RAMAN ANALYSIS OF OCTOCORAL CARBONATE ION LATTICE DISORDER ALONG A NATURAL DEPTH GRADIENT, KONA COAST, HAWAIʻI

A THESIS SUBMITTED TO THE GRADUATE DIVISION OF THE UNIVERSITY OF HAWAIʻI AT MĀNOA IN PARTIAL FULFILLMENT OF THE REQUIREMENTS FOR THE DEGREE OF

MASTER OF SCIENCE

IN

OCEANOGRAPHY

MARCH 2022

By

Kyle A. Conner

Thesis Committee:

Samuel Kahng, Co-Chairperson
Christopher Sabine, Co-Chairperson
Shiv Sharma
Richard Zeebe

Keywords: Octocorals, magnesian calcite, carbonate ion disorder, Raman spectroscopy

DEDICATION PAGE

I would like to thank my loving parents, Michael Earl Conner and Takako Uzawa Conner, and my brother, Kevin, for their love and support. I also thank my Kumu housemates for always being there for me, rain or shine.

ACKNOWLEDGEMENTS

Octocoral Raman analysis was supported by the Raman and Infrared Spectroscopy Laboratory at the Hawaiʻi Institute for Geophysics and Planetary Sciences. I would like to specifically thank Dr. Miles Egan for providing micro-Raman instrument training and troubleshooting. Collection of octocoral samples and oceanographic data were made possible by the Hawaiʻi Undersea Research Laboratory (HURL). Financial support for ship and submersible time were provided by the NOAA Deep Sea Coral and Sponge Research and Technology Program. I thank Dr. Juan Sánchez and Dr. Luisa Dueñas at the Universidad de Los Andes in Colombia and Dr. Bertalan Lendvay at the University of Zürich for morphological and genetic identification of the octocoral specimens. Sample M3 was provided by Dr. Frank Parrish from the Pacific Islands Fisheries Science Center.

I would also like to thank Ryohei Uchiyama (Hokkaido University), Dr. Kentaro Tanaka (University of Tokyo), Dr. Naoko Murakami-Sugiyama (University of Tokyo), and Dr. Kotaro Shirai (University of Tokyo) for their generation of the LA-ICPMS Mg data collected from cross sections of our sampled octocorals. Their contributions have been recognized via co-authorship on the submitted manuscript associated with this thesis work.

ABSTRACT

Both environmental and vital effects cause carbonate lattice disorder in biogenic Mg-calcites. A major component of this disorder is driven by the incorporation of Mg through environmental forcing and growth rate kinetics although non-Mg factors (e.g., other cation/anion impurities, organic molecules) also contribute. Understanding the drivers of Mg content in biogenic calcite and its effects on disorder has implications for octocoral Mg paleo-proxies and the stability and diagenetic alteration of their calcitic skeletons. However, prior studies of biogenic Mg-calcites have often been complicated by sampling inconsistencies over space and time and potential intra-sample Mg variability. This study aims to analyze the relative contributing factors of octocoral Mg-calcite lattice disorder along gradients of both depth and growth rate. Calcitic octocorals (Corallidae and Isididae, N = 28) were collected from 221–823 m across a natural gradient in biogeochemical parameters (pH: 7.4–7.9, T: 5–16°C) off the Kona coast of Hawaiʻi Island and analyzed using Raman spectroscopy. Samples were collected during the same month, controlling for potential seasonal variability. Raman spectral parameters from the ν_1 peak quantified total carbonate lattice disorder (full width at half maximum height [FWHM] of ν_1) and Mg content (ν_1 position, Raman shift). The total lattice disorder was then partitioned into Mg-driven and non-Mg driven components (residual FWHM). The total lattice disorder and Mg content decreased significantly with increasing depth, correlating with temperature and carbonate system parameters. The Mg-temperature relationships from this study were also consistent with prior studies. Residual FWHM did not correlate to any environmental parameters. When measured across an intra-sample gradient of (ontogenetic) growth rate, total lattice disorder, Mg content, and residual FWHM increased with growth rate for all but one taxon, demonstrating the kinetic effect of growth rate as well as potential taxon-specific vital effects. These results provide insight into how environmental and growth rate kinetic effects

independently affect different components of carbonate lattice disorder (Mg content and non-Mg factors). These findings also suggest that Raman spectroscopy may be helpful in quantifying solubility within biogenic calcites.

TABLE OF CONTENTS

LIST OF TABLES

LIST OF FIGURES

PREFACE

My admission to the Oceanography graduate program was unique in the sense that I was not provided a research advisor upon arrival. I eventually met with Dr. Samuel Kahng, an Associate Professor at Hawaiʻi Pacific University and Affiliate Graduate Faculty in the Oceanography Department at the University of Hawaiʻi, and was interested in the research project he proposed to me involving the geochemical analysis of octocoral samples using Raman spectroscopy. The use of Raman in this study required the expertise and equipment of Dr. Shiv Sharma, a researcher at the Hawaiʻi Institute of Geophysics and Planetology and leader in Raman-related research. These two, in addition to UH Oceanography's Dr. Christopher Sabine and Dr. Richard Zeebe, provided a wealth of knowledge to my M.S. committee relating to octocoral biology and ecology, Raman spectroscopic theory and application, calcite mineral geochemistry, and seawater carbonate chemistry.

This thesis was reliant upon a sample set of octocorals and oceanographic data collected on a series of research cruises conducted by the Hawaiʻi Undersea Research Laboratory in 2011, 2016, and 2017. My main advisor, Dr. Kahng, was present during all cruises. Since these cruises were conducted prior to my enrollment in the UH Oceanography graduate program, I did not participate in the collection of octocorals and oceanographic data. The processing of seawater samples for biogeochemical data was also conducted prior to my arrival as well.

The contents of this thesis are heavily based upon a manuscript submitted to the American Mineralogist peer-reviewed journal in December 2021 with the same title and the following authorship: Kyle Conner, Shiv Sharma, Ryohei Uchiyama, Kentaro Tanaka, Naoko Murakami-Sugihara, Kotaro Shirai, Samuel Kahng.

1. INTRODUCTION

1.1 Background and knowledge gaps

Environmental and physiological (i.e., vital effects) factors can influence carbonate ion lattice disorder (referred to hereinafter as lattice disorder) within biogenic calcites through the incorporation of elemental impurities as well as growth rate kinetics and organic molecules involved in biogenic calcification. Calcite lattice disorder involves the orientation of carbonate ions relative to the *c* (vertical) and *a* (horizontal) unit cell axes (Bischoff et al. 1985). Ideally, carbonate ions are symmetrically aligned with their respective basal planes along the *a* axis, however, deviations from this symmetry occur at varying extents within synthetic and biogenic calcites. The incorporation of non-constituent ion impurities (divalent cations with radii differing from Ca) such as Mg, Sr, and Ba results in altered cation-oxygen bond lengths that can rotate carbonate ions out of the basal plane towards the *c* axis (Bischoff et al. 1985; Urmos et al. 1991; Perrin et al. 2016). Large anions like sulfate (relative to carbonate ions) can also be substituted into the calcite lattice and increase lattice disorder (reviewed in Vielzeuf et al. 2018). Kinetic effects influenced by growth rate as well as ambient temperature and pressure also promote increased disorder because rapid crystallization reduces the symmetric alignment of carbonate ions and increases the incorporation of impurities (Watson 2004; Morse et al. 2007; Mavromatis et al. 2013). Calcite precipitation rates can be elevated through favorable physicochemical conditions obtained either through the exterior environment or within an organism's extracellular calcifying fluid (Al-Horani et al. 2003; Morse et al. 2006; McCulloch et al. 2012). Organic molecules like skeletal organic matrices are crucial in regulating biogenic crystal nucleation and can also introduce disorder by interacting with adjacent carbonate ions (Tambutté et al. 2011; Mass et al. 2013; DeCarlo et al. 2018). Biogenic calcites are known to contain larger unit cell volumes and *c*/*a* axis ratios relative to synthetic calcites even with comparable concentrations of elemental impurities such as Mg (Bischoff et al. 1985).

A major component of lattice disorder within biogenic calcite involves the incorporation of Mg cations, which is largely driven by temperature, carbonate system parameters, and skeletal growth rate. Although the exact mechanisms influencing biogenic Mg incorporation are not well understood (Long et al. 2014), the connection between temperature and Mg content in organisms such as octocorals has been well established (Weinbauer et al. 2000; Thresher et al. 2004, 2010; Sherwood et al. 2005). Carbonate system parameters such as saturation state (Ω) have also been correlated with Mg content (Thresher et al. 2011) due to their thermodynamic and kinetic influence on calcite solubility (Mackenzie et al. 1983; Mucci 1987; Morse et al. 2007). Other studies have also highlighted the complications of seasonal skeletal growth rate effects on Mg content (Vielzeuf et al. 2013, 2018; Robinson et al. 2014; Chaabane et al. 2019; Flöter et al. 2019). The main factor controlling Mg incorporation is still debated, although a combination of different environmental factors (e.g., temperature) simultaneously influencing biological response and growth rate kinetics is generally thought to be the case (Vielzeuf et al. 2018).

Understanding the drivers of octocoral Mg content and resulting lattice disorder has implications for mineral solubility and Mg paleo-proxies, yet prior studies have been complicated by inconsistencies in sampling location and timeframes as well as potential Mg variability within individual organisms. Higher calcite Mg content generates lattice disorder that decreases mineral stability and increases solubility across natural gradients in depth and latitude (Andersson et al. 2008; Lebrato et al. 2016). Mg-temperature relationships are integral to paleothermometry applications, yet the impact of vital effects on Mg incorporation and resulting lattice disorder confounds temperature reconstructions (Chaabane et al. 2019). Prior geochemical studies on octocorals relied on limited or opportunistic sample sets lacking in corresponding environmental data with specimens collected from a wide variety of locations and timeframes (Robinson et al. 2014). As a result, attempts to distinguish Mg contributions from different environmental and vital effects are fundamentally confounded. Specimens from different oceanographic regimes contain a different combination of biogeochemical conditions and food sources, which could impact the elemental geochemistry of octocoral skeletons (Hasegawa et al. 2012). Not accounting for time-based variables such as seasonal growth rates could also lead to inaccuracies if samples are collected at different times of the year. Spatial variability in trace elements within individual octocoral skeletons has been analyzed through radial cross section measurements for numerous species, revealing areas of relatively faster growth (e.g., medullar zone for *Corallium rubrum*, Vielzeuf et al. 2008). However, intra-sample variability has not been quantified on surface skeletons despite providing an opportunity to observe the effects of variable growth rates (branches vs. base; Vielzeuf et al. 2008) for skeletons precipitated concurrently under the same environmental conditions. Only a few studies have analyzed octocoral geochemistry with respect to environmental gradients involving corresponding oceanographic parameters (Thresher et al. 2011; Bostock et al. 2015), which have better enabled the analysis of major environmental effects on measured Mg.

Raman spectroscopy can provide a fast, nondestructive method of quantifying octocoral lattice disorder from Mg and non-Mg sources as well as Mg content. The Raman spectra of calcium carbonates contain six main peaks: two representing the intermolecular lattice vibration modes (librational L peak and translational T peak) and four representing the internal vibration modes (ν_1, $2\nu_2$, ν_3, ν_4) (Bischoff et al. 1985, Fig. 1). The incorporation of smaller sized (relative to Ca) Mg cations into calcite shortens cation-oxygen bonds, which then elevate the vibrational frequencies and positional disorder of neighboring carbonate ions (Krishnamurti 1957; White 1974; Bischoff et al. 1985). Raman spectral parameters like peak position (Raman shift, cm^{-1}) and width (full width at half magnitude, FWHM, cm^{-1}) increase predictably as a function of Mg content (mol%, Bischoff et al. 1985; Perrin et al. 2016; Fig. 2). Incorporated divalent cations larger than Ca such as Ba and Sr generate longer, weaker bonds with oxygen that should, in theory, oppose and suppress the Raman signal influenced by Mg. Analogous work on aragonite minerals reported that ν_1 Raman shift values decrease 0.0544 cm^{-1} per mmol/mol Sr/Ca and 0.0004 cm^{-1} per μmol/mol B/Ca while increasing 0.0262 cm^{-1} per mmol/mol Mg/Ca (Farfan et al. 2021). However, findings from Kaabar et al. (2011) demonstrated that considerable Ba and Sr content (up to 33% of total cations) did not cause significant changes to calcite ν_1 peak Raman shift when the Ca fraction was 20% or higher. Previous Raman calibration of calcite Sr content also observed no significant change in calcite ν_1 peak characteristics even across a 0–13% range in Sr content (Shibano et al. 2017). Sulfate anions thought to impact lattice disorder did not significantly change ν_1 Raman shift in calcites with up to 20% $CaSO_4$ (Kontoyannis et al. 1997). While large fractions of Ba, Sr, and S can interact with Ca to significantly alter calcite FWHM values (Kontoyannis et al. 1997; Kaabar et al. 2011), Ba, Sr, and S content within octocoral calcite is negligible based on previous studies (Thresher et al. 2007; LaVigne et al. 2011; Sinclair et al. 2011; Vielzeuf et al. 2018). For instance, octocoral Sr/Ca and B/Ca had ranges of only around 1.26 mmol/mol and 59 μmol/mol, respectively (Farmer et al. 2015; Vielzeuf et al. 2018). Using the ratios from Farfan et al. (2021), this translates to Raman shift decreases of 0.069 cm^{-1} and 0.023 cm^{-1}, which are small compared to the expected 1.67 cm^{-1} increase from Mg based on Mg/Ca ranges (~64 mmol/mol) from Vielzeuf et al. (2018). A similar outcome is reached with respect to FWHM for those ranges in Mg/Ca (+1.91 cm^{-1}), Sr/Ca (-0.047 cm^{-1}), and B/Ca (-0.018

cm^{-1}). Farfan et al. 2021 did not measure Ba/Ca, but its concentration in octocorals (range of 8.1 μmol/mol) is less than that of B/Ca (Vielzeuf et al. 2018). Observed Raman spectral changes from octocoral calcite can therefore be predominantly attributed to Mg. The FWHM of biogenic calcite is consistently larger than that of synthetic calcites even at very similar Mg content (Bischoff et al. 1985), suggesting that physiological factors aside from Mg are contributing to overall disorder. As such, the overall FWHM signal can be partitioned into Mg and non-Mg driven components (e.g., residual FWHM, Comeau et al. 2018; DeCarlo et al. 2019). The residual FWHM parameter quantifies lattice disorder after the effects of Mg incorporation on overall FWHM have been removed and has been employed in studies of Mg-calcite crustose coralline algae as a potential qualitative proxy of calcifying fluid Ω (Comeau et al. 2018; Cornwall et al. 2018, 2020).

1.2 Goals and expectations of the study

The goals of this study are to separate and analyze the relative contributions of lattice disorder with respect to environmental gradients and variable growth effects within octocoral colonies to better understand the drivers of disorder within octocoral calcite. Lattice disorder (Mg and non-Mg) as well as Mg content were measured within the calcitic surface skeletons of three Corallidae species and one Isididae genus collected along a natural gradient in depth and environmental parameters (temperature, pH, Ω, salinity) off the Kona coast of Hawai‘i Island within the same month. The study area took advantage of the North Pacific's naturally compressed vertical oceanographic gradients and shallow calcium carbonate saturation horizons (Greenwood 2009). Geochemical parameters were measured from the basal portion of skeleton using Raman spectroscopy and compared to corresponding in situ oceanographic data to determine the effect of environmental factors on lattice disorder while controlling for seasonal growth effects. Intra-sample Raman measurements were conducted on specific octocoral specimens at varying branch diameters to analyze disorder with respect to variable growth rates under fixed environmental conditions.

We expect the depth gradient measurements to demonstrate the effects of environmental parameters on octocoral lattice disorder and Mg content. In other words, overall lattice disorder and Mg content should decrease with increasing depth as a result of temperature decreases. Non-Mg lattice disorder could potentially decrease along the depth gradient due to decreasing skeletal growth rates. Taxon-specific patterns in non-Mg lattice disorder could also occur, although the octocoral species in the sample set are closely related. We expect the intra-sample Raman measurements to demonstrate the effects of varying growth rates on lattice disorder and Mg incorporation. Smaller branch diameters should represent areas of faster skeletal growth compared to larger branch diameters, which should result in increases in overall lattice disorder and Mg content with decreasing branch diameter. Non-Mg lattice disorder should also increase with decreasing branch diameter since it is thought to be driven by growth rate kinetics as well as organic molecule incorporation.

2. MATERIALS and METHODS

2.1 Octocoral collection and oceanographic observations

Deep-sea octocorals of the families Corallidae and Isididae were collected live along a natural depth gradient (221–823 m, nitrate maximum at ~800 m with pH = 7.35 and DIC = 2340 μmol/kg) off the leeward coast of Hawaiʻi Island (Fig. 3, Table 1). Sample collections were made using *Pisces IV/V* submersibles as part of the Hawaiʻi Undersea Research Laboratory (HURL) cruises in 2011, 2016, and 2017 during the same season (August to September). An additional sample (M3) collected off Makapuʻu, Oʻahu at 417 m depth was used for the calibration of Raman-based Mg content. All relevant octocoral specimens (N = 28) were taxonomically identified by specialists at the University of Colombia, Bogotá (Luisa Dueñas; Ardila et al. 2012, Dueñas et al. 2014) and the University of Zürich (Bertalan Lendvay; Lendvay et al. 2020). Octocoral species in this sample set include *Pleurocorallium* cf. *secundum*, *Corallium tortuosum*, *Hemicorallium imperiale/laauense* (a single species complex; Dueñas and Lendvay, pers. comm.), and *Acanella* spp. (likely multiple species). Prior to geochemical analysis, organic matter was removed from the skeletons by soaking and rinsing them in a sodium hypochlorite (bleach) and water mixture and rinsing with fresh water.

At each sampling site, oceanographic parameters were measured from the surface down to 1000 m to fully characterize water column chemistry. In the sites visited during the 2011 cruise (Hoʻokena, Kealakekua, Waiahukini), CTD hydrocasts equipped with a Sea-Bird SBE-9, SBE-18 pH probe, and a rosette of 24 Niskin bottles were conducted at 4–5 stations per site along a 2 km transect perpendicular to the shore. Hydrocasts provided continuous measurements of temperature, conductivity (salinity), and pH as well as discrete water samples (N = 89) that were stored in borosilicate glass bottles in a cool dark container until chemical analysis. Additional continuous temperature, salinity, and pH data were measured using SBE-25 CTD and SBE-18 pH probes attached to the submersible during sample collection. At the Kailua-Kona site, temperature loggers (Onset TidbiT v2) were deployed on the seafloor at nine stations from 200–900 m and collected data every 30 minutes for 12 months (Sept 2016 to Aug 2017, Fig. 4). This additional data enabled the quantification of vertical oscillations in isopycnal depths from internal tides, which aided with accurately aligning environmental parameters with octocoral samples.

Discrete seawater samples were analyzed for carbonate system parameters (pH, DIC, TA) in accordance with standard operation procedures described in Dickson et al. (2007) and Riebesell et al. (2010) with appropriate modifications for differences in our analytical equipment. Dissolved inorganic carbon (DIC) was measured using an APOLLO SciTech DIC analyzer (model AS-C3). Total alkalinity (TA) was measured using an automated open-cell potentiometric titration method described in Dickson et al. (2007). Certified reference materials (CRM) were measured routinely to confirm measurement accuracy. Spectrophotometric measurements of pH were made using an m-cresol purple dye indicator on a temperature-controlled spectrophotometer (Thermo Scientific™ Orion™ AquaMate 7000 Vis Spectrophotometer). Tris standards (Dickson Lab, SIO) were used to verify dye quality and measurement accuracy. Necessary temperature and salinity measurements were conducted using a YSI multiparameter meter (YSI 5563). CO2SYS (Excel; Lewis and Wallace 1998) was used to calculate calcite saturation state (Ω_{Cal}), [CO_3^{2-}], and [HCO_3^-] using K_1 and K_2 dissociation constants from Mehrbach et al. (1973) refit by Dickson and Millero (1987), K_{HSO4} from Dickson (1990), total boron from Uppström (1974), and seawater-scale pH. Potential density (σ_θ) was calculated in MATLAB using the Gibbs-Seawater toolbox (McDougall and Barker 2011).

2.2 Oceanographic data adjustments using seawater potential density

Oceanographic data were adjusted as the CTD casts and discrete bottle samples only provide a depth-based snapshot of mid-water environmental conditions. While sessile benthic organisms like octocorals are fixed at depth, oceanographic parameters are tightly fixed to density-specific water masses, which can undergo constant vertical oscillations from physical forcing, thereby exposing octocorals to a range of environmental conditions over short timescales. Inertial oscillations in seawater masses are apparent through high-resolution temperature data collected from Kailua-Kona, which can be driven by factors such as lunar tides and larger mesoscale eddies. Such oscillations also visibly attenuate with increasing depth (due to density gradients) and can influence oceanographic measurements conducted at a fixed depth depending on the time of sampling. The temperature time-series data, as well as correlations between temperature and potential density (σ_θ, kg/m^3) from the CTD casts, provided insight on the magnitude of water mass oscillations over different depths and times and allowed for CTD measurement adjustments. A temperature and σ_θ correlation converted high-resolution temperature data over multiple depths into high-resolution σ_θ data which was then averaged by depth over a 24-hour composite period (e.g., changes in σ_θ relative to mean σ_θ ($\Delta\sigma_\theta$) as a function of time of day). The depth and timing of specific oceanographic measurements were inserted into the 24-hour averaged curves to calculate $\Delta\sigma_\theta$. A more accurate σ_θ ($\sigma_{\theta,\mathrm{True}}$) was then calculated through

$$\sigma_{\theta,\mathrm{True}} = \sigma_{\theta,\mathrm{Measured}} + \Delta\sigma_\theta \tag{1}$$

which approximated a more accurate corresponding oceanographic parameter depending on the relationship between said parameter and $\sigma_{\theta,\mathrm{True}}$.

2.3 Micro-Raman instrumentation

The micro-Raman system located in the Raman and Infrared Spectroscopy Laboratory at the Hawaiʻi Institute of Geophysics and Planetology (HIGP) was used to conduct Raman measurements in accordance with procedures used in Acosta-Maeda et al. (2013). The instrument is comprised of a Kaiser Micro-Raman Spectrometer with a RAMAN RXN1™ Microprobe (Kaiser Optical Systems Inc.) and a Leica DMLB microscope with a 100x maximum magnification objective, motorized x-y stage, Kaiser HoloSpec spectrometer, and Andor CCD camera. The near-infrared excitation laser uses an external-cavity Invictus diode laser with a maximum power of 66 mW. The laser wavelength was set at 785 nm to reduce interference from octocoral skeletal organic matter via residual fluorescence (DeCarlo et al. 2017, 2018). The system has a spatial resolution of ~1 μm (using the 100x objective) with a Raman spectral lines measurement accuracy of ±0.5 cm^{-1} and a spectral range of 150–3300 cm^{-1}. Cyclohexane Raman spectra (801.3 cm^{-1} peak) were frequently measured to check for instrument drift over time. GRAMS/AI software (Thermo Fisher Scientific Inc.) was used to curve fit the Raman ν_1 peak with a mixed Gaussian-Lorentzian curve that allowed the extraction of Raman shift and linewidth (peak width) parameters. Calculating the final FWHM required deconvolving the Raman instrument linewidth from the raw measured linewidth. Deconvolutions were done via Raman measurements of Neon lamp light and the equation:

$$\omega_{obs}^2 = \omega_{actual}^2 + \omega_{inst}^2 \tag{2}$$

where ω_{obs} is the observed linewidth of the Raman peak, ω_{inst} is the instrument-based linewidth, and ω_{actual} is the true linewidth (FWHM) from the analyzed sample.

2.4 Raman-based Mg content calculation and corrections

The Mg content of the octocoral surface skeleton was calculated using the ν_1 peak calibration lines from Perrin et al. (2016) (see Fig. 2). The calibration line for Raman shift was:

$$\text{Raman shift (cm}^{-1}) = 0.256 \times [\text{MgCO}_3 \text{ (mol\%)}] + 1085.71 \ (R^2 = 0.988) \tag{3}$$

which covers a range of 0 to 50 mol% $MgCO_3$. Overall FWHM can be partitioned into a Mg-driven component (Mg-driven FWHM) and a non-Mg component (residual FWHM). Mg-driven FWHM is calculated by applying the Mg content from the Raman shift calibration line to the FWHM calibration line:

$$\text{FWHM (cm}^{-1}) = -0.00787 \times [\text{MgCO}_3 \text{ (mol\%)}]^2 + 0.51 \times [\text{MgCO}_3 \text{ (mol\%)}] + 3.61 \qquad (4)$$

$$(R^2 = 0.973)$$

Residual FWHM is the difference between the overall FWHM signal and Mg-driven FWHM. The resulting Mg value was then used to predict the FWHM signal contributed by Mg (Mg-driven lattice disorder, Perrin et al. 2016), which was then subtracted from the overall FWHM measurement to obtain the residual FWHM value (non-Mg lattice disorder).

The accuracy of the calculated Mg values based on Perrin et al. (2016) was first verified through the pairing of measurements from Raman spectroscopy and Laser Ablation Inductively Coupled Plasma Mass Spectrometry (LA-ICPMS) on polished octocoral basal cross sections. Radial Mg measurements were conducted on a subset of depth gradient octocorals as well as sample M3 from Makapuʻu (N = 8, Table 1) using an Agilent 7700cs connected with an excimer laser (NWR-193, New Wave Research) at the Atmosphere and Ocean Research Institute, The University of Tokyo. Setup conditions included a 100-μm diameter laser spot, a pulse rate of 10 Hz and pulse energy of 3 mJ, using He as the carrier gas. The signal intensity of ions (^{26}Mg and ^{43}Ca) was calculated by subtracting the background level of trace elements, which had been obtained empirically with the laser output set to 0%. Subsequently, the ratio of trace elements to ^{43}Ca was obtained and compared to the signal intensities of standard reference materials. The reference material NIST SRM 612 was used as an external standard, with the reference materials coral powder JCp-1 and giant clam powder JCt-1 (National Institute of Advanced Industrial Science and Technology, Tsukuba, Japan) measured to confirm accuracy. The reference materials were analyzed three times before and after every 50–100 sample spots to monitor instrument drift. The Mg/Ca ratio calculations were based on the analyses of NIST SRM 612, standard glass, and reproducibility (percent relative standard deviation [%RSD]), measured at

<5%. The Mg/Ca ratio of JCp-1 (certified value of Mg/Ca = 4.2 mmol/mol) was determined to be Mg/Ca = 4.5 ± 0.2 (1σ, N = 26) mmol/mol. Detailed analytical conditions are reported in the literature (e.g., Murakami-Sugihara et al. 2019).

Observable round craters in the cross-section surface from the 100-μm laser spot were used to align the subsequent Raman measurements. Raman measurements (N = 10 per marker) were taken adjacent to each crater along the transects. Raman-based Mg estimates were compared to LA-ICPMS Mg to generate a trendline between the two data sources to validate the equations from Perrin et al. (2016) and adjust Raman-based Mg content for the octocoral samples.

2.5 Octocoral surface skeleton Raman measurements

Raman measurements were taken on the outermost, up current side of the basal portion (>3 mm diameter) of the octocoral skeletons to capture the geochemical conditions at the time of sample collection. Octocorals tend to display skewed growth patterns in their basal cross sections due to consistent variations in radial growth rate in different directions (Luan et al. 2013; Vielzeuf et al. 2018). Growth rates are fastest on the up current side of the corals (opposite of the feeding polyps) and produce relatively thicker growth rings (Kahng, pers. obs.). The central portion of the cross sections contains the fast-growing medullar region (Corallidae) or the central axis (Isididae), which is known to have naturally higher Mg content than the surrounding growth rings (Vielzeuf et al. 2008; Perrin et al. 2015; Flöter et al. 2019). All Raman measurements (N = 15 per sample: 3 5-point transects with ~100 μm spacing) were taken from the up current side of the thicker basal portion of skeleton (as opposed to younger, thinner branches that are likely comprised of mostly medullar skeleton) to reduce potential growth rate bias in Mg measurements across the depth gradient (Fig. 7). Preliminary sample size analysis demonstrated that at least N

= 9 Raman measurements per octocoral sample yield a negligible change in standard error values (Fig. 8).

Raman measurements were also taken across the surface skeleton of several entire octocoral samples (*P.* cf. *secundum* from 273 m; *C. tortuosum* from 280 m; *H. imperiale/laauense* from 444 m; *H. imperiale/laauense* from 472 m; *Acanella* spp. from 823m) to investigate intra-sample variability in lattice disorder and Mg content. The same transect approach was used on 20 different locations along the octocoral surface (N = 100), spanning from thicker basal regions to thinner branches. Branch diameter, the distance between the up current and down current sides, was measured using digital calipers (0.01 mm resolution; Neiko Tools, USA) and then compared to corresponding Raman measurements (FWHM, Mg content, residual FWHM) to ascertain within-sample variability as well as whether such variation is attributable to incidental sampling of the medullar or central axis region (e.g., near branch tips).

Potential Mg and non-Mg disorder patterns along the depth gradient were compared with corresponding oceanographic measurements to illuminate patterns between skeletal geochemistry and environmental conditions. Univariate models were emphasized as temperature and carbonate system parameters were highly collineated. All relevant statistical analyses were conducted using R Studio (version 4.0.5, R Core Team 2021). For this study, significance was defined as $P < 0.05$.

3. RESULTS

3.1 Environmental context

Oceanographic parameters (temperature, salinity, pH, Ω_{Cal}) decreased sharply at around 100 m depth, signifying the transition to denser water masses (Fig. 9). Environmental parameters began to stabilize past 500 m. The calcite saturation horizon (Ω_{Cal} = 1) was almost reached at ~600 m. Collinearity was also observed in the oceanographic data, especially between pH and temperature (Fig. 10). The sampled octocorals displayed a clear depth zonation pattern with *P.* cf. *secundum* and *C. tortuosum* inhabiting the shallowest areas from ~220 m to ~300 m and *H. imperiale*/*laauense* observed in deeper regions from ~400 m to ~580 m. *Acanella* spp. had a wider depth distribution from ~400 m to over 800 m. Depths from 221 m to 823 m experienced temperature and pH values ranging from 16.37 to 4.99 °C and 7.94 to 7.41, respectively.

Temperature data from multiple depths ranging from 220 to 900 m depict short-term (M_2 semidiurnal tidal cycles; Merrifield and Holloway 2002) and long-term (mesoscale eddies; Calil et al. 2008) variability resulting from the oscillations of water masses with different densities over a yearlong interval (Fig. 4). Deviations from the average potential density were relatively small (~0.01 kg/m^3 at most) and resulted in few adjustments in depth-based oceanographic data (Fig. 5). Power spectral density analysis revealed consistent tidal patterns dominated by the M_2 semidiurnal tide, which decreased rapidly with increasing depth (Fig. 6). Average temperatures decreased rapidly after the 220 m logger (average temperature of 16.29 ± 1.32 °C compared to 11.02 ± 0.79 °C from 302 m) but then stabilized at 506 m and greater (6.80 ± 0.29 °C).

3.2 LA-ICPMS corrections to Raman-based skeletal Mg content

Mg content displayed considerable scatter (~2.5 mol% range) around the linear relationship of

$$\text{LA-ICPMS Mg} = (1.1116 \times \text{Raman Mg}) + 3.0703 \text{ with } R^2 = 0.77 \text{ (Fig. 11a)} \qquad (5)$$

There was a noticeable grouping of data points corresponding with the two octocoral species sampled (*H. imperiale/laauense* and *P.* cf. *secundum*). Although the LA-ICPMS Mg values closely overlapped between the two species, Raman-derived Mg values showed greater differences close to 2 mol%. The trendline slope did not differ greatly from the 1:1 line between Raman Mg and LA-ICPMS Mg, although there was an offset in Mg indicated by the y-intercept where Raman-Mg underpredicted Mg by 3.86 ± 0.74 mol% on average. Henceforth, corrections based on the linear relationship between LA-ICPMS and Raman are applied to the octocoral Raman-based Mg data (depth gradient and intra-sample measurements). Raman-based Mg content appeared to increase significantly towards the medullar region of the cross-section as exemplified with the slow growth axis of *P.* cf. *secundum* from 238 m (Dev. Expl. = 0.94, R^2 = 0.92), which was well correlated with LA-ICPMS Mg data (R^2 = 0.79, $P < 0.001$, Fig. 11b, c).

3.3 Octocoral lattice disorder and skeletal Mg along depth gradient

Octocoral FWHM ranged from a high of 10.06 ± 0.03 cm^{-1} detected from *P.* cf. *secundum* at 221 m to a low of 9.11 ± 0.04 cm^{-1} from *H. imperiale/laauense* at 574 m. FWHM across all octocoral species significantly decreases with increasing potential density (Fig. 12). *H. imperiale*/*laauense* FWHM displayed a significant relationship with potential density, while *Acanella* spp. did not appear to display any notable FWHM patterns (Table 2). *P.* cf. *secundum* FWHM had an especially strong relationship with potential density although only four samples were collected. Only two samples of *C. tortuosum* were acquired so no taxon-specific trendline could be generated for any of the Raman parameters. When only Corallidae octocorals were considered, the FWHM depth gradient correlation was further strengthened.

Octocoral Mg content along the depth gradient ranged from a high of 11.54 ± 0.04 mol% $MgCO_3$ detected from *C. tortuosum* at 280 m to a low of 8.97 ± 0.09 mol% $MgCO_3$ from *H. imperiale/laauense* at 582 m. Mg content also significantly decreases with increasing potential density (Fig. 12). *H. imperiale*/*laauense* Mg displayed a significant yet weaker relationship with potential density compared to FWHM, while *Acanella* spp. Mg displayed no significant pattern with potential density. *P.* cf. *secundum* Mg content was more moderately correlated with potential density compared to FWHM (Table 3). The Mg depth gradient pattern was again strengthened when only Corallidae octocorals were considered.

Residual FWHM ranged from 1.73 ± 0.08 cm^{-1} for *Acanella* spp. at 451 m to 1.21 ± 0.04 cm^{-1} for *H. imperiale/laauense* at 399 m and did not change significantly with potential density (Fig. 12, Table 4). Moreover, two-way ANOVA tests yielded no significant taxon-specific patterns between octocoral residual FWHM and those oceanographic parameters (best interaction was between Species and Ω_{Cal}; $F_{3,20} = 1.54$, $P = 0.23$).

FWHM was most strongly correlated with $[CO_3^{2-}]$ and Ω_{Cal} ($R^2 = 0.93$ and $R^2 = 0.92$, respectively), although temperature and pH also displayed strong correlations (Fig. 13, Table 2). FWHM from *Acanella* spp. displayed no significant relationships with any environmental parameter. *H. imperiale/laauense* FWHM was strongly correlated with all environmental parameters except salinity, with the strongest covariance being with TA ($R^2 = 0.74$). *P.* cf. *secundum* FWHM was well correlated with all environmental parameters.

Mg content had similar correlation patterns compared to FWHM although R^2 values were lower overall. $[CO_3^{2-}]$ and Ω_{Cal} (both $R^2 = 0.84$) maintained the strongest positive correlations with octocoral Mg content (Fig. 14, Table 3). In *Acanella* spp., the Mg content displayed no significant relationships with any environmental parameter. *H. imperiale/laauense* was moderately correlated with all environmental parameters except for salinity. *P.* cf. *secundum* Mg was well correlated with all environmental parameters except for pH (only moderately correlated), but all linear models had no significant p-values due to low sample size.

Residual FWHM was weakly correlated with all environmental parameters with the highest correlation occurring with pH (R^2 = 0.24, Table 4). Multivariate FWHM, Mg content, and residual FWHM relationships with environmental parameters are also displayed in Figure 15 and Table 8.

3.4 Octocoral intra-sample lattice disorder and skeletal Mg

FWHM of *P.* cf. *secundum* collected at 273 m consistently increased at smaller branch diameters from 9.70 ± 0.05 cm^{-1} at 5.18 mm to 9.95 ± 0.04 cm^{-1} at 0.95 mm (Fig. 16a). Mg content is mostly scattered between 11.22 ± 0.04 mol% and 11.63 ± 0.04 mol% with a notable peak of 11.87 ± 0.08 mol% at 1.77 mm (Fig. 16a). Residual FWHM also increased somewhat both at the smallest branch diameters (from 1.27 ± 0.03 cm^{-1} at 5.64 mm to 1.48 ± 0.04 cm^{-1} at 0.95 mm) and at high branch diameters (e.g., 1.43 ± 0.06 cm^{-1} at 10.13 mm). In *C. tortuosum* from 280 m, both FWHM (9.76 ± 0.03 cm^{-1} to 9.76 ± 0.03 cm^{-1}) and residual FWHM (1.36 ± 0.02 cm^{-1} to 1.59 ± 0.05 cm^{-1}) increased nonlinearly with decreasing branch diameter, while Mg content increased more linearly from 11.37 ± 0.09 mol% at 7.31 mm to 11.75 ± 0.13 mol% at 1.45 mm (Fig. 16b).

Within the *H. imperiale/laauense* specimen collected at 444 m, FWHM sharply increased to 9.87 ± 0.03 cm^{-1} at less than 0.5 mm compared to values of around 9.2–9.4 cm^{-1} from larger diameters (Fig. 16c). Mg content experienced a similar pattern with values increasing to greater than 10.23 ± 0.07 mol% at diameters less than 0.58 mm. Residual FWHM increased with decreasing branch diameter at a consistent rate from 1.41 ± 0.01 cm^{-1} at 3.67 mm to 1.80 ± 0.02 cm^{-1} at 0.39 mm. In *H. imperiale/laauense* from 472 m, FWHM (from 9.14 ± 0.02 cm^{-1} at 3.98 mm to 9.47 ± 0.04 cm^{-1} at 0.73 mm) and Mg content (9.02 ± 0.07 mol% to 9.56 ± 0.02 mol% at those same diameters) also increased with decreasing branch diameter at a consistent rate (Fig.

16d). Its residual FWHM values followed a similar yet more scattered gradual increase from 1.48 ± 0.02 cm^{-1} at 6.82 mm to 1.70 ± 0.04 cm^{-1} at 0.73 mm. The sharp step-like FWHM and Mg spikes observed within the *H. imperiale/laauense* specimens contrasted with the more linear and scattered changes within *P.* cf. *secundum* and *C. tortuosum*.

In *Acanella* spp. 823 m, a similar relationship was observed between branch diameter and Mg content, which rose from 9.25 ± 0.07 mol% at 8.61 mm to 9.88 ± 0.09 mol% at 1.05 mm (Fig. 16e). However, FWHM (9.23 ± 0.03 cm^{-1} at 6.76 mm to 9.03 ± 0.05 cm^{-1} at 1.05 mm) and residual FWHM (1.55 ± 0.04 cm^{-1} at 6.76 mm to 1.15 ± 0.04 cm^{-1} at 1.05 mm) contained strikingly different patterns with branch diameter compared to FWHM and residual FWHM from the other octocoral specimens.

Taxon-specific relationships among overall FWHM, Mg-based FWHM, and residual FWHM were apparent (Fig. 17, Table 5). Within *P.* cf. *secundum* from 273 m, Mg-based FWHM was weakly correlated with overall FWHM (R^2 = 0.29), while residual FWHM and overall FWHM were more strongly correlated (R^2 = 0.59). FWHM values from the *H. imperiale/laauense* specimen collected at 444 m were well correlated with both Mg-based (R^2 = 0.67) and residual FWHM (R^2 = 0.67). Moderate to strong correlations (R^2 = 0.52 and R^2 = 0.63, respectively) were also observed for *H. imperiale/laauense* from 472 m. All relevant FWHM parameters within *C. tortuosum* from 280 m were strongly correlated with one another, although the relationship between FWHM and residual FWHM (R^2 = 0.90) was much stronger here compared to that of FWHM and Mg-based FWHM (R^2 = 0.67). FWHM values measured from *Acanella* spp. at 823 m were weakly correlated with Mg-based FWHM (R^2 = 0.11) but strongly correlated with residual FWHM (R^2 = 0.74). Relationships among overall FWHM, Mg-based

FWHM, and residual FWHM were also provided from the LA-ICPMS corrections (Fig. 18, Table 6).

4. DISCUSSION

4.1 Quantifying skeletal Mg content from Raman measurements

Raman spectral measurements of octocoral calcite should be largely representative of changes in Mg content as opposed to other incorporated cations and anions (discussed in Introduction). It should be noted that the range in Mg content within the octocorals is narrow, equating to a Raman shift range of only 1.09 cm^{-1} for the LA-ICPMS corrections, 0.59 cm^{-1} for the depth gradient, and 0.65 cm^{-1} for the intra-sample measurements. However, assuming similar elemental ratios between Mg and other ions like Sr, B, and Ba from Vielzeuf et al. (2018), we would expect to see a range of around 1.92 mmol/mol Sr/Ca, 89.64 μmol/mol B/Ca, and 0.012 μmol/mol Ba/Ca for 97 mmol/mol Mg/Ca. Changes in Mg should again dominate the Raman signal (e.g., based on Farfan et al. 2021, +2.54 cm^{-1} from Mg with only -0.10 cm^{-1} from Sr), yet the presence of non-Mg cations could lead to underestimated Raman-based Mg values. For this reason, the LA-ICPMS Mg correction is needed to obtain more accurate Mg values from Raman shift. While the results of Farfan et al. (2021) provide a potential detailed look into the effects of certain divalent cations on Raman spectral analysis of $CaCO_3$, a detailed analogous analysis on calcite minerals is needed.

The trendline (Eqn. 5) comparing LA-ICPMS and Raman-based Mg displays a consistent offset of around 3 mol% from the 1:1 line with Raman shift underestimating LA-ICPMS Mg (Fig. 11a). The Raman-Mg calibration lines from Perrin et al. (2016) are based on calcites synthesized under high pressure and temperature without the presence of non-Mg cations/anions, organic molecules, or other physiological factors that could impact the calcite Raman signal. It is possible that the presence of non-Mg cations/anions are driving the underestimated Raman-based Mg values in this case. Raman shift values within biogenic Mg-calcites are also known to be slightly lower than their synthetic counterparts at similar Mg content (Bischoff et al. 1985). The consistent offset of the LA-ICPMS and Raman trendline suggests that these biogenic factors are largely similar across the octocoral species in this study. There is a notable spread of data points around the trendline that could be due to the differing spatial resolutions of LA-ICPMS (100 μm) and Raman (~2 μm). Octocoral skeletons are known to contain fine-scale spatial variability in Mg content (Vielzeuf et al. 2008). While smaller differences in Mg content are being masked by the spatial mismatch between the two methods, larger Mg differences are better resolved. For instance, Figs. 11b-c highlights the sharp increase in Mg content from the skeletal surface to the medullar region within a single cross section sample of *P.* cf. *secundum*, resulting in a strong LA-ICPMS and Raman Mg trendline with relatively less scatter. Nevertheless, a strong correlation exists between the two methods with a consistent offset, thus allowing Raman-based Mg content to be corrected.

4.2 Environmental drivers of lattice disorder and skeletal Mg

In this study, all octocoral specimens were collected over multiple years (2011, 2016, and 2017) but within the same four-week period (August-September), thereby minimizing the impacts of seasonal growth variations on Mg content and lattice disorder (Mavromatis et al. 2013; Vielzeuf et al. 2013, 2018; Flöter et al. 2019). Moreover, the collection of specimens from the same oceanographic regime minimizes differences in food sources (via surface primary productivity and export) and biogeochemical conditions that can inherently confound results. By controlling for spatial (e.g., sampling location and corresponding oceanography) and temporal (e.g., seasonal growth) variables, environmental factors and taxon-specific effects can be better isolated. Overall FWHM and Mg content both decrease across the environmental gradient, indicating an overall decrease in lattice disorder correlating strongly with decreasing temperature and carbonate system parameters. The relationship between potential density (depth) and FWHM and Mg content agrees with prior findings along environmental gradients (Andersson et al. 2008; Thresher et al. 2011). Lower temperatures at greater depth result in a thermodynamically more soluble Mg-calcite structure relative to warmer, shallower waters (Mucci 1987; Morse et al. 2007). Conditions less conducive to calcification at depth (reduced pH, [CO_3^{2-}], and Ω_{Cal}) would also lead to thermodynamically less stable calcite, which discourages Mg incorporation (Mackenzie et al. 1983). Although the relationship between calcite Mg content and temperature has received relatively more attention, carbonate system parameters maintain the highest correlations with FWHM and Mg in this study with strong temperature correlations as well.

Non-Mg driven lattice disorder measured using residual FWHM displayed no clear pattern with depth or environmental parameters. Residual FWHM decreases slowly with depth only among the shallowest *C. tortuosum* and *P.* cf. *secundum* specimens, yet the variable clustering from deeper *H. imperiale/laauense* and Isididae disrupts any overall trends. The lack of significant change in non-Mg disorder with depth suggests that the octocoral calcite stability influenced by vital effects or growth rate kinetics not involving Mg are not sensitive to environmental changes. In contrast, FWHM and Mg display strong patterns with depth, which implies that skeletal lattice disorder is due largely to Mg incorporation. If the majority of non-Mg lattice disorder is driven by variations in growth rate, then Mg should dominate the FWHM signal given that seasonal growth rates are controlled through a consistent sampling protocol over time and location within the sample (basal portion of surface skeleton). Another possibility is that basal skeleton growth rate itself does not change significantly with depth, which has been observed by Thresher et al. (2016) for Isididae.

FWHM could also be positively correlated with extracellular calcifying fluid Ω (Ω_{ECF}) due to the well-recognized positive relationship between calcite growth rates and Ω (Morse et al. 2007). For biogenic calcifiers, higher Ω_{ECF} should drive faster skeletal accretion rates, which would increase lattice disorder and FWHM values. While this relationship has been well demonstrated for aragonite and used to quantify shallow water coral Ω_{ECF} (DeCarlo et al. 2019), it has not yet been verified for Mg-calcite. Prior studies have used residual FWHM as a qualitative proxy for Ω_{ECF} within Mg-calcite calcifiers (e.g., crustose coralline algae, Comeau et al. 2018; Cornwall et al. 2018, 2020) assuming that the Mg-calcite FWHM-Ω_{ECF} relationship operates similarly to that of aragonite (DeCarlo et al. 2017). If true, then the results here would indicate that Ω_{ECF} is not sensitive to the environmental gradient. While this result would have interesting implications for octocoral responses to contemporary carbonate chemistry gradients as well as ongoing ocean acidification, a systematic calibration between calcite Ω_{ECF} and Raman spectral parameters (e.g., FWHM) is needed to confirm these results.

Mg-temperature relationships in this study align with relationships from prior studies of synthetic and biogenic calcite (Fig. 19, Table 7). The linear expression for skeletal Mg/Ca as a function of temperature based on all available octocoral samples from this study ($R^2 = 0.70$, N = 28) as well as the one derived exclusively from Corallidae ($R^2 = 0.73$, N = 23) either overlapped or were similar to those established for *Corallium* spp., *C. rubrum*, and *Corallium* spp. compiled in previous studies (Chave 1954; Weinbauer et al. 2000; Yoshimura et al. 2011; Vielzeuf et al. 2013; Thresher et al. 2016; Chaabane et al. 2019). Only the model from Weinbauer et al. (2000) ($R^2 = 0.99$, N = 3) had a very different slope and intercept. Isididae from this study ($R^2 = 0.20$, N

= 5) did not display a strong relationship albeit with a low sample size. The Isididae model generated by Thresher et al. (2016) (R^2 = 0.87, N = 73) was similar to prior Corallidae models. Inorganic high-Mg calcite experiments under varying temperatures (5–40°C) also yielded a slope overlapping with the above octocoral studies although the intercept was much lower (Mucci 1987). The comparable Mg-temperature slopes between organic and inorganic calcite suggest a similar kinetic Mg incorporation mechanism (Thresher et al. 2016). Meanwhile, differences in intercept values among different octocoral Mg models could result from taxon-specific effects. The lack of a consistent intra-annual Mg-temperature relationship in prior studies is likely driven by interference from vital effects amplifying Mg content (Vielzeuf et al. 2013). Nevertheless, vital effects can be a product of temperature as well as other environmental parameters. While seasonal fluctuations in skeletal growth rate appear to drive intra-annual Mg variability, longer-term mean temperature has been correlated with average octocoral Mg content (Chaabane et al. 2019), a result that could be observed here along the depth gradient.

4.3 Growth rate effects on lattice disorder and skeletal Mg

Within individual octocoral specimens, the change in residual FWHM with respect to branch diameter differs from that of Mg content despite experiencing the same environmental history. Intra-sample Raman measurements can examine lattice disorder as a function of changes in skeletal growth rate driven entirely by organismal physiology and not by environmental conditions. Octocoral branches grow lengthwise and radially (branch width/diameter) over time. As branches increase in length, the medullar or central axis skeleton is precipitated first. As the branch thickens via radial growth, the medullar skeleton eventually transitions to an annular skeleton containing observable growth rings (Fig. 7). Because growth rates are relatively higher within the interior medullar zone and central axis of Corallidae and Isididae skeleton, respectively (Vielzeuf et al. 2008; Flöter et al. 2019), radial growth rates should be faster for smaller branch diameters and relatively slower at larger ones. This pattern is further implied by the increase in residual FWHM (non-Mg disorder) with decreasing branch diameter (Fig. 16). Linear changes in residual FWHM with respect to branch diameter, as opposed to stepwise changes observed for Mg discussed later, could be a result of ontogenetic growth effects where radial growth rates naturally and gradually decrease with age and size (Sinclair et al. 2011; Farmer et al. 2015; Flöter et al. 2019). The differing residual FWHM pattern observed within *Acanella* spp. (Fig. 16e) is puzzling since greater non-Mg disorder was also expected within the faster growing central axis of Isididae. This inverted pattern is also well manifested in the overall FWHM signal despite Mg content increasing with decreasing branch diameter. Secondary infilling could lead to spikes in Mg content and potential growth anomalies in locations where newer skeleton was more recently formed, yet Mg content does not display the same inverted pattern as overall and non-Mg lattice disorder (Flöter et al. 2019). Further intra-sample analysis of *Acanella* spp. surface skeleton is needed to confirm whether this outcome is simply an anomaly or the result of a consistent taxon-specific mineralogical difference. Ω_{ECF} could also at least partially contribute to these intra-sample patterns although such interpretations must be approached with caution. As branch diameter (i.e., skeletal growth rate) varies, correlations between residual FWHM and FWHM are comparable to that of Mg content and FWHM (Fig. 17, Table 5). Non-Mg growth rate kinetics appears to contribute more towards overall intra-sample lattice disorder relative to the environmental gradient, where only Mg and FWHM were significantly correlated (Fig. 12).

Stepwise increases in Mg content with decreasing octocoral branch diameter are indicative of faster-growing medullar or central axis skeleton, which typify ontogenetic growth patterns in Corallidae and Isididae (Vielzeuf et al. 2008; Sinclair et al. 2011). Significant increases in Mg content were observed with decreasing branch diameter, especially at diameters smaller than 2 mm (Fig. 16). This value agrees with spatially mapped Electron Microprobe Analysis (EMPA) data of Corallidae (*C. rubrum*) cross sections where the diameter of the medullar region containing higher Mg was 1.0–2.0 mm with an irregular shape (Vielzeuf et al. 2008; Fig. 7, 11b). For Isididae, the central axis is known to be much rounder with a maximum diameter of 1.0 mm (Flöter et al. 2019). The outer edge of the central axis skeleton in *Acanella* spp. was likely detected through the sharp Mg peak at 1.05 mm diameter. As observed with residual FWHM, the early growth medullar zone would intuitively be exposed at the branch tip surface, resulting in Mg spikes at the smallest branch diameters. Elevated Mg content in these regions is likely a product of kinetic effects driven by skeletal growth rates (reviewed in Vielzeuf et al. 2018). In scleractinian skeletons, Gagnon et al. (2007) noted that high Mg regions (also known as Centers of Calcification) were influenced by non-Rayleigh processes in contrast to the rest of the skeleton. Mechanisms such as the growth entrapment model (Watson 2004) as well as a more modified impurity incorporation/repulsion model (Vielzeuf et al. 2018) have been proposed to explain the connection behind precipitation rate and Mg incorporation. The presence of differing organic molecules within rapid growth zones is also thought to selectively enhance Mg incorporation (Gagnon et al. 2007). Regardless of the exact mechanism, these differing growth regions demonstrate the need to focus comparative octocoral surface Mg measurements at the thicker basal portions of skeleton to avoid accidental sampling of the medullar zone.

4.4 Taxon-specific patterns in lattice disorder and skeletal Mg

Analysis of intra-sample Mg and non-Mg lattice disorder reveals potentially different biomineralization patterns among closely related Corallidae species (*H. imperiale/laauense, C.*

tortuosum, *P.* cf. *secundum*; Ardila et al. 2012) as well as Isididae. Throughout most of the intra-sample specimens, Mg-based FWHM and residual FWHM are both well correlated with overall FWHM although the strength of these relationships varies by species. Some species patterns (e.g., *P.* cf. *secundum*) appear to be more strongly influenced by non-Mg sources compared to others (e.g., *H. imperiale/laauense*) (Fig. 17, Table 5). Mg and residual FWHM are positively correlated within *C. tortuosum* and *H. imperiale*/*laauense* while being negatively correlated in *P.* cf. *secundum*. The high variability between the two parameters, however, resulted in no significant trends except for *C. tortuosum*. *P.* cf. *secundum* and *C. tortuosum* also displayed relatively lower residual FWHM values despite having the highest Mg content. Mg content and residual FWHM were expected to be positively correlated since both are positively impacted by skeletal growth rates (DeCarlo et al. 2017; Vielzeuf et al. 2018). This outcome is only seen within *C. tortuosum* where both Mg and non-Mg lattice disorder strongly contribute to overall lattice disorder. The lower residual FWHM values within the *P.* cf. *secundum* and *C. tortuosum* specimens could be evidence of a taxon-specific biomineralization effect given the concurrent similarity in FWHM results between the two *H. imperiale/laauense* specimens. Despite this similarity in FWHM, *C. tortuosum* is taxonomically more closely related to *H. imperiale/laauense* than *P.* cf. *secundum* (Ardila et al. 2012). Another instance of taxon-specific biomineralization is observed with *Acanella* spp., which displayed unforeseen FWHM and residual FWHM patterns with branch diameter. Although these results were surprising considering the known radial growth patterns for Isididae (Flöter et al. 2019), *Acanella* spp. resides in a different taxonomic family compared to the remaining specimens.

LA-ICPMS and Raman Mg data also display indications of taxon-specific patterns in octocoral Mg and non-Mg disorder. *H. imperiale/laauense* and *P.* cf. *secundum* cross sections from multiple depths were used in the analysis of LA-ICPMS and Raman-based Mg data. Despite an overlap of LA-ICPMS Mg content between the two species (~10.5–11.2 mol%), Mg content based on Raman shift forms two distinct taxon-specific groups (Fig. 11a). Grouping is also observed with corresponding FWHM data, although residual FWHM does not appear to show any significant patterns (Fig. 18). Like the intra-sample analysis, residual FWHM values within *P.* cf. *secundum* are similar to those of *H. imperiale/laauense* despite the former having greater FWHM and Mg content than the latter (Fig. 20 and Table 6). Overall lattice disorder and vibrational frequencies are greater in *P.* cf. *secundum* compared to *H. imperiale/laauense* even at areas with the same LA-ICPMS Mg content. Increasing calcite unit cell volumes are thought to lead to lower vibrational frequencies (lower Raman shift) and lattice disorder (Bischoff et al. 1985). In this case, *H. imperiale/laauense* specimens could have characteristically larger unit cell volumes compared to *P.* cf. *secundum* specimens. As previously mentioned, the general discrepancies between LA-ICPMS and Raman Mg content could be attributed to physiological mechanisms absent from the synthetic calcites used in Perrin et al. (2016). Both Raman shift and FWHM-based trendlines are mostly offset from the 1:1 line through the y-intercept, suggesting that physiological factors contributing to the Mg discrepancy could be largely similar across different octocoral individuals and species. However, the slope of the FWHM trendline (0.79 ± 0.04) is offset more compared to that of Raman shift (1.11 ± 0.06), indicating that different parts of the LA-ICPMS/Raman FWHM signal (e.g., from different species) are being impacted differentially. The Mg-driven disorder appears to be relatively higher for *P.* cf. *secundum* compared to *H. imperiale/laauense*.

Skeletal morphologies could also explain observed differences in Mg and non-Mg driven disorder with respect to changes in branch diameter and growth rate. Stepwise increases in Mg content are apparent within *H. imperiale/laauense* and *Acanella* spp. but occur to a lesser extent within *P.* cf. *secundum* and *C. tortuosum*. Faster-growing medullar zones may not be well defined for some individual octocorals, thereby resulting in a less obvious change in lattice disorder and Mg. While the intra-sample *P.* cf. *secundum* specimen displayed inconsistent Mg patterns, one specimen of *P.* cf. *secundum* analyzed by LA-ICPMS and Raman displayed a sharp radial increase in Mg content (Fig. 11b, c). A possible explanation of this phenomenon could be connected to skeletal morphology rather than inherent taxon-specific differences in medullar skeleton characteristics. For instance, the robust skeletons of *P.* cf. *secundum* (as well as *C. tortuosum*) quickly transition from thick basal branches to warped irregular branch tips compared to the smoother transitions in *H. imperiale/laauense* (Fig. 16). Less consistent Mg patterns with branch diameter could be a product of inconsistencies in the assumed relationship between growth rate and branch diameter caused by the irregular skeletal morphology itself. Based on the patterns observed with *P.* cf. *secundum* and *C. tortuosum*, branch diameter may not be as reliable of a growth rate metric for the irregular morphologies of those species compared to *H. imperiale/laauense*. Whether the formation of this differing skeletal morphology significantly alters any of the mechanisms (e.g., growth kinetics, non-Rayleigh mechanisms, biomolecules) thought to influence lattice disorder and Mg content within the medullar zone is unknown (Gagnon et al. 2007; Tambutté et al., 2011).

5. CONCLUSIONS AND RESEARCH IMPLICATIONS

5.1 Study conclusions and expectations

In conclusion, the measurement and analysis of octocoral Mg-calcite lattice disorder and Mg content were conducted under two settings: 1. Under varying environmental parameters while attempting to control ontogenetic growth rates (i.e., depth gradient); 2. Under varying growth rates with controlled environmental parameters (i.e., intra-sample). Additional correction of Raman-based Mg content was conducted using Mg data measured using LA-ICPMS.

The comparison of Mg data from Raman and LA-ICPMS displayed a consistent offset between the two methods where Raman calibration lines underestimated LA-ICPMS Mg by several mol%. Although the resulting correction line (Eqn. 5) possessed a fairly strong correlation score and a slope value close to 1, it also contained highly scattered data. It is thought that the spatial mismatch between Raman and LA-ICPMS spatial resolutions contributed to the scattered data. Although small differences in Mg content were not well-resolved, it appeared that larger differences in Mg content were better resolved. It is recommended for future comparative exercises that Raman be paired with instrumentation like EMPA due to its similar spatial resolution. Future analysis into the effects of individual seawater cations/anions on lattice disorder and Raman spectral parameters within calcites will also be needed.

Depth gradient measurements displayed significant decreases in overall lattice disorder and Mg content with increasing depth. Both overall lattice disorder and Mg content were most strongly correlated with carbonate system parameters ([CO_3^{2-}], Ω_{Cal}, pH), although strong correlations with temperature were also observed. Mg-temperature relationships obtained from this study aligned well with prior octocoral studies and possessed slope values similar to that of inorganic Mg-calcite studies. Non-Mg lattice disorder displayed no significant patterns with depth. Overall lattice disorder and Mg content results agree with initial predictions and are likely driven by the transition to increasingly undersaturated waters where high lattice disorder and Mg content are less tolerated. The lack of a depth-based pattern for non-Mg lattice disorder was also within expectations due to the controls on seasonal and spatial variability in skeletal growth rates. However, taxon-specific patterns in non-Mg lattice disorder were not observed.

Intra-sample measurements displayed significant increases in overall lattice disorder, Mg content, and non-Mg lattice disorder with decreasing branch diameter for most of the selected octocoral specimens. These results confirmed the presence of skeletal growth patterns involving medullar and annular zones and their effects on Mg incorporation. Non-Mg lattice disorder patterns also demonstrated ontogenetic growth patterns where lattice disorder and therefore radial growth rate decreases with age. Nevertheless, these patterns were not consistent among all analyzed specimens and appeared to be taxon-specific. The *Acanella* spp. specimen displayed a particularly unexpected pattern with the highest lattice disorder occurring at the largest branch diameters. Further analysis of more individual octocoral specimens (especially *Acanella* spp.) could provide more insight on these findings.

The main findings of this study also have implications for the following areas relating to Mg-calcite mineral solubility and the use of Mg as an environmental paleothermometer.

5.2 FWHM, skeletal Mg content, and calcite mineral stability

Mg measurements alone do not appear to entirely capture the factors impacting biogenic Mg-calcite disorder and therefore stability. Mg has been demonstrated to be a major driver of lattice disorder within synthetic and biogenic calcites, although other sources of disorder can originate from non-Mg sources such as organic molecules and other physiological effects from calcification (Bischoff et al. 1985; Perrin et al. 2016). Data from this study has shown instances where octocoral specimens of very similar Mg content differed in their overall FWHM, a result likely to occur from additional lattice disorder from non-Mg sources (residual FWHM). For example, while the intra-sample Mg content from *P.* cf. *secundum* and *C. tortuosum* overlapped heavily, FWHM values from the latter often exceeded that of the former (Fig. 16). Mg and FWHM data from the depth gradient samples are well correlated but express a nonlinear relationship, indicating that there are factors influencing FWHM differently from Mg. The EMPA-based Mg and FWHM calibration line from Perrin et al. (2016) (Eqn. 4) is also nonlinear as opposed to their strongly linear Raman shift Mg calibration line (Eqn. 3). Intra-sample FWHM and Mg relationships also varied strongly among different species, which is likely driven by variable taxon-specific skeletal growth rates. Clearly, non-Mg lattice disorder can impact the overall FWHM signal independently from Mg.

Raman spectroscopic measurements of calcite FWHM could theoretically provide a quantitative proxy for solubility although empirical validations must first be performed. Mg has served as a prominent proxy for synthetic and biogenic calcite solubility through its correlations with carbonate chemistry along depth and latitudinal gradients (Andersson et al. 2008; Lebrato et al. 2016). While Mg-based metrics of solubility are valid for synthetic calcites, biogenic calcites are subject to significant variability in solubility estimates even for specimens of similar Mg content (Morse et al. 2006). Because FWHM can quantify overall lattice disorder within carbonate minerals (Bischoff et al. 1985), the spectral parameter could provide a robust method to incorporate non-Mg factors influencing calcite stability and therefore solubility. Increased accuracy in determining biogenic calcite solubility could help determine which calcifying organisms are most at risk from stressors like ocean acidification. Despite the logical relationship between lattice disorder and mineral solubility, no experiments to date have quantified the relationship between calcite solubility and FWHM.

5.3 Taxon-specific biomineralization patterns

Biomineralization patterns differ by species, especially between those residing in shallower and deeper water, respectively. Certain specimens (*H. imperiale/laauense*) displayed lattice disorder and Mg values anticipated from a sharp radial change in skeletal growth zones (i.e., from annular to medullar). However, changes in lattice disorder were less striking in other specimens (*P.* cf. *secundum*, *C. tortuosum*) with some patterns (*Acanella* spp.) being entirely different from expectations. Such differences could be linked to vital effects involving organic molecules or larger calcification mechanisms that influence the specific manner of calcite precipitation and subsequent Mg incorporation. Further clarification of these taxon-specific biomineralization patterns could provide insight as to how certain species precipitate skeleton differently than others as well as how such biominerals react to future environmental change.

5.4 Implications for use of skeletal Mg as a paleo-proxy

A better understanding of calcite lattice disorder will clarify applications of Mg paleo-proxies. Vital effects interfere with the correlation between skeletal Mg and temperature since faster growth also enhances Mg content (Vielzeuf et al. 2018). This interference is particularly apparent in temperate waters where growth rate and temperature covary seasonally. The results from this study demonstrate the effect that growth rates on different segments of octocoral skeleton can have on Mg content despite experiencing the same environmental conditions. Correcting Mg content for vital effects will likely require the quantification and removal of growth rates with respect to changes in Mg to isolate the purely abiotic environmental effects.

TABLES

Table 1: Metadata for all depth gradient octocoral samples and M3 from Makapuʻu.

Sample ID#	Date/Time Sampled	Depth (m)	Location	Species	LA-ICPMS?
108	9/5/2016, 3:34pm	221	Kailua-Kona	*Pleurocorallium* cf. *secundum*	Yes
107	9/5/2016, 2:29pm	238	Kailua-Kona	*Pleurocorallium* cf. *secundum*	Yes
204	9/5/2016, 3:12pm	269	Kailua-Kona	*Pleurocorallium* cf. *secundum*	No
106	9/5/2016, 2:06pm	273	Kailua-Kona	*Pleurocorallium* cf. *secundum*	No
1105	9/28/2011, 12:33pm	280	Kealakekua	*Corallium tortuosum*	No
105	9/5/2016, 1:40pm	293	Kailua-Kona	*Corallium tortuosum*	No
1124	9/30/2011, 2:00pm	395	Waiahukini	*Hemicorallium imperiale/laauense*	Yes
1126	9/30/2011, 2:44pm	396	Waiahukini	*Acanella* spp.	No
1101	9/28/2011, 1:45pm	399	Kealakekua	*Hemicorallium imperiale/laauense*	Yes
1112	9/29/2011, 11:28am	401	Hoʻokena	*Hemicorallium imperiale/laauense*	No
1114	9/29/2011, 12:22pm	402	Hoʻokena	*Hemicorallium imperiale/laauense*	No
104	9/5/2016, 1:16pm	405	Kailua-Kona	*Acanella* spp.	No
1121	9/30/2011, 9:44am	444	Waiahukini	*Hemicorallium imperiale/laauense*	No
1120	9/30/2011, 8:56am	445	Waiahukini	*Hemicorallium imperiale/laauense*	No
1104	9/28/2011, 10:00am	446	Kealakekua	*Hemicorallium imperiale/laauense*	No
314	8/30/2017	447	1919 Lava Flow*	*Hemicorallium imperiale/laauense*	No
1109	9/29/2011, 9:18am	449	Hoʻokena	*Hemicorallium imperiale/laauense*	No
1110	9/29/2011, 10:01am	449	Hoʻokena	*Hemicorallium imperiale/laauense*	No
1117	9/29/2011, 3:29pm	449	Hoʻokena	*Hemicorallium imperiale/laauense*	No
1103	9/28/2011, 9:47am	451	Kealakekua	*Acanella* spp.	No
103	9/5/2016, 12:30pm	472	Kailua-Kona	*Hemicorallium imperiale/laauense*	No
202	9/5/2016, 1:49pm	506	Kailua-Kona	*Hemicorallium imperiale/laauense*	No
304	8/29/2017, 12:57pm	544	Kailua-Kona	*Hemicorallium imperiale/laauense*	No
313	8/30/2017	560	1919 Lava Flow*	*Hemicorallium imperiale/laauense*	Yes
312	8/30/2017	574	1919 Lava Flow*	*Hemicorallium imperiale/laauense*	Yes
102	9/5/2016, 11:45am	582	Kailua-Kona	*Hemicorallium imperiale/laauense*	Yes
303	8/29/2017, 11:27am	753	Kailua-Kona	*Acanella* spp.	No
101	9/5/2016, 10:56am	823	Kailua-Kona	*Acanella* spp.	No
M3	2/5/2000	417	Makapuʻu	*Hemicorallium imperiale/laauense*	Yes

Note: The 1919 Lava Flow site was just south of the Hoʻokena site.

Table 2: Linear regression data for FWHM in all species with respect to each environmental variable measured. P-values for statistically significant ($P < 0.05$) models are bolded. No models shown for *C. tortuosum* due to small sample size (N = 2).

Species	Environmental Variable	Fitted Coefficients	R^2	F	P	N
All	Temperature	$0.0002x^2 + 0.0812x + 8.7192$	0.8639	79.35	**1.49e-11**	28
All	Salinity	$8.717x^2 – 597.79x + 10258$	0.3815	7.71	**0.0025**	28
All	pH	$1.058x^2 – 14.73x + 60.187$	0.8947	106.20	**6.06e-13**	28
All	TA	$0.0002x^2 – 0.822x + 965.33$	0.3750	7.50	**0.0028**	28
All	CO_3^{2-}	$6.04e\text{-}6x^2 + 0.0062x + 8.8913$	0.9251	154.30	**8.57e-15**	28
All	Ω_{Cal}	$0.0086x^2 + 0.275x + 8.9152$	0.9241	152.20	**1.01e-14**	28
All	Potential Density	$0.109x^2 – 6.2464x + 98.433$	0.8512	71.53	**4.53e-11**	28
Isididae	Temperature	0.0561x + 8.9976	0.3677	1.74	0.28	5
Isididae	Salinity	-0.3255x + 20.544	0.0823	0.27	0.64	5
Isididae	pH	1.6252x – 2.7762	0.3264	1.45	0.31	5
Isididae	TA	-0.0019x + 13.768	0.3087	1.34	0.33	5
Isididae	CO_3^{2-}	0.0065x + 8.959	0.2918	1.24	0.35	5
Isididae	Ω_{Cal}	0.2769x + 8.9949	0.3364	1.52	0.31	5
Isididae	Potential Density	-0.2807x + 16.932	0.3082	1.34	0.33	5
H. imperiale/laauense	Temperature	0.0931x + 8.597	0.6621	29.39	**7.08e-5**	17
H. imperiale/laauense	Salinity	-0.1219x + 13.461	0.0097	0.15	0.71	17
H. imperiale/laauense	pH	0.7564x – 1.1379	0.5483	18.21	**0.00068**	17
H. imperiale/laauense	TA	-0.0051x + 20.902	0.7436	43.50	**8.51e-6**	17
H. imperiale/laauense	CO_3^{2-}	0.0076x + 8.8167	0.7094	36.62	**2.22e-5**	17
H. imperiale/laauense	Ω_{Cal}	0.3337x + 8.8333	0.7076	36.30	**2.32e-5**	17
H. imperiale/laauense	Potential Density	-0.4942x + 22.513	0.5292	16.86	**0.00093**	17
P. cf. *secundum*	Temperature	0.0708x + 8.8961	0.9938	319.40	**0.0031**	4
P. cf. *secundum*	Salinity	0.7668x – 16.469	0.9397	31.15	**0.031**	4
P. cf. *secundum*	pH	2.6887x – 11.296	0.9857	137.90	**0.0071**	4
P. cf. *secundum*	TA	0.0269x – 51.456	0.9307	26.88	**0.035**	4
P. cf. *secundum*	CO_3^{2-}	0.0101x + 8.4541	0.9373	29.92	**0.032**	4
P. cf. *secundum*	Ω_{Cal}	0.4123x + 8.5454	0.9370	29.77	**0.032**	4
P. cf. *secundum*	Potential Density	-0.5055x + 22.879	0.9963	539.40	**0.0018**	4
Corallidae	Temperature	$-0.0043x^2 + 0.186x + 8.1542$	0.9531	203.3	**5.14e-14**	23
Corallidae	Salinity	$8.3378x^2 – 571.6x + 9806$	0.4284	7.50	**0.0037**	23
Corallidae	pH	$1.0444x^2 – 14.429x + 58.756$	0.9535	205.10	**4.72e-14**	23
Corallidae	TA	$0.0003x^2 – 1.223x + 1425.8$	0.4006	6.68	**0.0060**	23
Corallidae	CO_3^{2-}	$5.61e\text{-}6x^2 + 0.0065x + 8.8579$	0.9708	332.90	**4.45e-16**	23
Corallidae	Ω_{Cal}	$0.0041x^2 + 0.3051x + 8.8634$	0.9707	331.20	**4.67e-16**	23
Corallidae	Potential Density	$-0.0972x^2 + 4.524x – 42.132$	0.9438	168	**3.13e-13**	23

Table 3: Linear regression data for Mg content in all species with respect to each environmental variable measured. P-values for statistically significant ($P < 0.05$) models are bolded. No models shown for *C. tortuosum* due to small sample size (N = 2).

Species	Environmental Variable	Fitted Coefficients	R^2	F	P	N
All	Temperature	$-0.0146x^2 + 0.5436x + 6.6131$	0.7254	33.03	**9.62e-8**	28
All	Salinity	$26.347x^2 – 1807.9x + 31024$	0.2858	5.00	**0.0149**	28
All	pH	$-5.0413x^2 + 81.603x – 318.65$	0.8026	50.82	**1.56e-9**	28
All	TA	$0.0007x^2 – 3.1269x + 3643.6$	0.5090	12.96	**1.37e-4**	28
All	CO_3^{2-}	$-0.0002x^2 + 0.0548x + 6.9746$	0.8425	66.85	**9.27e-11**	28
All	Ω_{Cal}	$-0.3018x^2 + 2.250x + 7.242$	0.8379	64.63	**1.32e-10**	28
All	Potential Density	$-0.2276x^2 + 10.543x – 109.30$	0.6999	29.16	**2.92e-7**	28
Isididae	Temperature	$0.1326x + 8.8438$	0.1931	0.72	0.46	5
Isididae	Salinity	$-0.0919x + 12.889$	0.0006	0.0019	0.97	5
Isididae	pH	$4.9526x – 27.295$	0.2857	1.20	0.35	5
Isididae	TA	$-0.0038x + 18.432$	0.1140	0.39	0.58	5
Isididae	CO_3^{2-}	$0.02425x + 8.1815$	0.3826	1.86	0.27	5
Isididae	Ω_{Cal}	$0.9321x + 8.4541$	0.3591	1.68	0.29	5
Isididae	Potential Density	$-0.5714x + 25.117$	0.1203	0.41	0.57	5
H. imperiale/laauense	Temperature	$0.4436x + 6.445$	0.4825	13.99	**0.0020**	17
H. imperiale/laauense	Salinity	$-1.1963x + 50.688$	0.02999	0.46	0.51	17
H. imperiale/laauense	pH	$5.8124x – 33.844$	0.4593	12.74	**0.0028**	17
H. imperiale/laauense	TA	$-0.02282x + 62.047$	0.4843	14.09	**0.0019**	17
H. imperiale/laauense	CO_3^{2-}	$0.0387x + 7.3198$	0.5982	22.33	**0.00027**	17
H. imperiale/laauense	Ω_{Cal}	$1.7146x + 7.399$	0.5999	22.49	**0.00026**	17
H. imperiale/laauense	Potential Density	$-2.5278x + 77.385$	0.4446	12.01	**0.0035**	17
P. cf. *secundum*	Temperature	$0.0942x + 9.9246$	0.6891	4.43	0.17	4
P. cf. *secundum*	Salinity	$1.1277x – 27.518$	0.7966	7.83	0.11	4
P. cf. *secundum*	pH	$3.1828x – 13.831$	0.5414	2.36	0.26	4
P. cf. *secundum*	TA	$0.0391x – 77.849$	0.7695	6.68	0.12	4
P. cf. *secundum*	CO_3^{2-}	$0.01475x + 9.1412$	0.7890	7.48	0.11	4
P. cf. *secundum*	Ω_{Cal}	$0.6040x + 9.2755$	0.7882	7.44	0.11	4
P. cf. *secundum*	Potential Density	$-0.6529x + 28.022$	0.6514	3.74	0.19	4
Corallidae	Temperature	$-0.0333x^2 + 0.9704x + 4.4049$	0.8255	47.32	**2.61e-8**	23
Corallidae	Salinity	$25.887x^2 – 1776.2x + 30477$	0.306	4.41	**0.026**	23
Corallidae	pH	$-5.9516x^2 + 95.656x – 372.86$	0.8309	49.12	**1.92e-8**	23
Corallidae	TA	$0.0014x^2 – 6.4597x + 7471$	0.6006	15.04	**1.03e-4**	23
Corallidae	CO_3^{2-}	$-0.0002x^2 + 0.0607x + 6.7317$	0.8700	66.91	**1.38e-9**	23
Corallidae	Ω_{Cal}	$-0.375x^2 + 2.5905x + 6.914$	0.8697	66.78	**1.41e-9**	23
Corallidae	Potential Density	$-1.2114x^2 + 62.001x – 781.91$	0.8216	46.05	**3.27e-8**	23

Table 4: Linear regression data for residual FWHM in all species with respect to each environmental variable measured. P-values for statistically significant ($P < 0.05$) models are bolded. No models shown for *C. tortuosum* due to small sample size (N = 2).

Species	Environmental Variable	Fitted Coefficients	R^2	F	P	N
All	Temperature	$0.005452x^2 – 0.1110x + 1.9914$	0.1715	2.59	0.095	28
All	Salinity	$-0.4691x^2 + 32.556x – 563.31$	0.1182	1.68	0.21	28
All	pH	$2.9019x^2 – 44.469x + 171.75$	0.2423	4.00	**0.031**	28
All	TA	$-5.9711e-5x^2 + 0.2771x – 319.89$	0.1172	1.66	0.21	28
All	CO_3^{2-}	$6.7148e-5x^2 – 0.01332x + 2.0444$	0.2284	3.70	**0.039**	28
All	Ω_{Cal}	$0.1181x^2 – 0.5269x + 1.9723$	0.2237	3.60	**0.042**	28
All	Potential Density	$0.1941x^2 – 10.23x + 136.2$	0.1569	2.33	0.12	28
Isididae	Temperature	$0.008294x + 1.4894$	0.01022	0.031	0.87	5
Isididae	Salinity	$-0.2864x + 11.374$	0.08123	0.27	0.64	5
Isididae	pH	$-0.157x + 2.7192$	0.003883	0.012	0.92	5
Isididae	TA	$-0.0005372x + 2.7861$	0.03141	0.097	0.78	5
Isididae	CO_3^{2-}	$-0.002201x + 1.6865$	0.04263	0.13	0.74	5
Isididae	Ω_{Cal}	$-0.05799x + 1.6251$	0.0188	0.057	0.83	5
Isididae	Potential Density	$-0.07360x + 3.5263$	0.02713	0.083	0.79	5
H. imperiale/laauense	Temperature	$-0.06367x + 1.9333$	0.1746	3.17	0.095	17
H. imperiale/laauense	Salinity	$0.3129x – 9.2508$	0.03603	0.56	0.47	17
H. imperiale/laauense	pH	$-0.9118x + 8.2972$	0.1984	3.71	0.073	17
H. imperiale/laauense	TA	$0.002997x – 5.4104$	0.1467	2.58	0.13	17
H. imperiale/laauense	CO_3^{2-}	$-0.006112x + 1.8425$	0.2619	5.32	**0.036**	17
H. imperiale/laauense	Ω_{Cal}	$-0.2717x + 1.8313$	0.2644	5.39	**0.035**	17
H. imperiale/laauense	Potential Density	$0.40212x – 9.3007$	0.1975	3.69	0.074	17
P. cf. *secundum*	Temperature	$0.03881x + 0.9957$	0.7125	4.96	0.16	4
P. cf. *secundum*	Salinity	$0.3861x – 11.73$	0.5685	2.63	0.25	4
P. cf. *secundum*	pH	$1.5968x – 11.042$	0.8297	9.74	0.089	4
P. cf. *secundum*	TA	$0.01369x – 29.649$	0.5742	2.70	0.24	4
P. cf. *secundum*	CO_3^{2-}	$0.005082x + 0.8160$	0.5702	2.65	0.24	4
P. cf. *secundum*	Ω_{Cal}	$0.2082x + 0.8619$	0.5703	2.65	0.24	4
P. cf. *secundum*	Potential Density	$-0.2832x + 8.8181$	0.7464	5.89	0.14	4
Corallidae	Temperature	$0.007514x^2 – 0.1558x + 2.2012$	0.2829	3.95	**0.036**	23
Corallidae	Salinity	$-0.7224x^2 + 50.06x – 865.66$	0.1964	2.44	0.11	23
Corallidae	pH	$3.1991x^2 – 48.993x + 188.94$	0.3342	5.02	**0.017**	23
Corallidae	TA	$-0.00022x^2 + 1.0269x – 1180.4$	0.2431	3.21	0.062	23
Corallidae	CO_3^{2-}	$7.6607e-5x^2 – 0.01503x – 2.0941$	0.3339	5.01	**0.017**	23
Corallidae	Ω_{Cal}	$0.1387x^2 – 0.6136x + 2.0341$	0.3357	5.06	**0.017**	23
Corallidae	Potential Density	$0.3341x^2 – 17.565x + 232.27$	0.3151	4.60	**0.023**	23

Table 5: Linear model statistics of the Mg and FWHM relationships obtained from the five octocoral specimens used during the intra-sample variability measurements.

Specimen	**Model Variables**	**Fitted Coefficients**	**R^2**	**F**	**P**
P. cf. *secundum* 273 m	FWHM vs. Mg FWHM	0.3485x + 5.0167	0.2892	7.33	**0.014**
P. cf. *secundum* 273 m	FWHM vs. Residual FWHM	0.6515x – 5.0167	0.5871	25.59	**8.17e-5**
P. cf. *secundum* 273 m	Mg vs. Residual FWHM	-0.0545xx + 1.9651	0.0159	0.29	0.60
C. tortuosum 280 m	FWHM vs. Mg FWHM	0.3187x + 5.2919	0.6675	36.14	**1.10e-5**
C. tortuosum 280 m	FWHM vs. Residual FWHM	0.6813x – 5.2919	0.9018	165.20	**1.66e-10**
C. tortuosum 280 m	Mg vs. Residual FWHM	0.3602x – 2.7067	0.3354	9.92	**0.0055**
H. imperiale/laauense 444 m	FWHM vs. Mg FWHM	0.5029x + 3.0478	0.6729	37.03	**9.47e-6**
H. imperiale/laauense 444 m	FWHM vs. Residual FWHM	0.4971x – 3.0478	0.6677	36.17	**1.09e-5**
H. imperiale/laauense 444 m	Mg vs. Residual FWHM	0.1216x + 0.4521	0.1191	2.43	0.14
H. imperiale/laauense 472 m	FWHM vs. Mg FWHM	0.4448x + 3.5648	0.5202	19.52	**0.00033**
H. imperiale/laauense 472 m	FWHM vs. Residual FWHM	0.5552x – 3.5648	0.6282	30.41	**3.09e-5**
H. imperiale/laauense 472 m	Mg vs. Residual FWHM	0.0622x + 0.9858	0.0228	0.42	0.53
Acanella spp. 823 m	FWHM vs. Mg FWHM	-0.2563x + 10.0231	0.1083	2.19	0.16
Acanella spp. 823 m	FWHM vs. Residual FWHM	1.2563x -10.0231	0.7448	52.24	**9.70e-7**
Acanella spp. 823 m	Mg vs. Residual FWHM	-0.5134x + 6.1823	0.5780	24.65	**0.0001**

Table 6: Linear model statistics of the Mg and FWHM relationships obtained from the octocorals samples used during the comparison between LA-ICPMS and Raman Mg measurements.

Specimen	Model Variables	Fitted Coefficients	R^2	F	P
P. cf. *secundum* 221 m	FWHM vs. Mg FWHM	0.6457x + 1.9757	0.4303	6.04	**0.039**
P. cf. *secundum* 221 m	FWHM vs. Residual FWHM	0.3544x – 1.9770	0.1856	1.82	0.21
P. cf. *secundum* 221 m	Mg vs. Residual FWHM	-0.3330x + 4.4880	0.1588	1.51	0.25
P. cf. *secundum* 238 m (fast axis)	FWHM vs. Mg FWHM	0.9422x – 0.8843	0.8434	64.65	**3.57e-6**
P. cf. *secundum* 238 m (fast axis)	FWHM vs. Residual FWHM	0.0574x + 0.8878	0.0196	0.24	0.63
P. cf. *secundum* 238 m (fast axis)	Mg vs. Residual FWHM	-0.1053x + 2.3768	0.0693	0.89	0.36
P. cf. *secundum* 238 m (slow axis)	FWHM vs. Mg FWHM	1.1172x – 2.6233	0.7617	76.72	**6.12e-9**
P. cf. *secundum* 238 m (slow axis)	FWHM vs. Residual FWHM	-0.1173x + 2.6248	0.034	0.85	0.37
P. cf. *secundum* 238 m (slow axis)	Mg vs. Residual FWHM	-0.3180x + 4.1835	0.4109	16.74	**0.0004**
H. imperiale/laauense 417 m	FWHM vs. Mg FWHM	0.4756x + 3.3721	0.3071	3.55	0.096
H. imperiale/laauense 417 m	FWHM vs. Residual FWHM	0.5130x – 3.2649	0.3383	4.089	0.078
H. imperiale/laauense 417 m	Mg vs. Residual FWHM	-0.3646x + 4.4492	0.1259	1.15	0.31
H. imperiale/laauense 560 m	FWHM vs. Mg FWHM	-1.2001x + 18.7908	0.5040	5.08	0.074
H. imperiale/laauense 560 m	FWHM vs. Residual FWHM	2.2009x – 18.7982	0.7738	17.10	**0.0090**
H. imperiale/laauense 560 m	Mg vs. Residual FWHM	-1.4201x + 12.4135	0.9206	57.95	**0.0006**
H. imperiale/laauense 574 m	FWHM vs. Mg FWHM	-0.3694x + 11.1474	0.1103	1.12	0.32
H. imperiale/laauense 574 m	FWHM vs. Residual FWHM	1.3691x – 11.1441	0.6300	15.33	**0.0035**
H. imperiale/laauense 574 m	Mg vs. Residual FWHM	-1.2985x – 11.5331	0.7012	21.12	**0.0013**
H. imperiale/laauense 582 m	FWHM vs. Mg FWHM	0.8690x – 0.4077	0.7789	35.22	**0.0001**
H. imperiale/laauense 582 m	FWHM vs. Residual FWHM	0.1310x + 0.4076	0.0742	0.80	0.39
H. imperiale/laauense 582 m	Mg vs. Residual FWHM	-0.1036x + 2.4030	0.0450	0.47	0.51

Table 7: Mg-temperature relationships from this study and other relevant octocoral or inorganic calcite studies. Numbers in the parentheses represent the 95% CI.

Study	**Taxon**	**Fitted Model** **Mg/Ca (mmol/mol) = A×T(°C) + B**	**Temp. Range (°C)**	**N**
This Study	Corallidae & Isididae	$2.94(\pm 0.75) \times T(℃) + 87.02(\pm 6.74)$	5-16.4	28
This Study	Corallidae	$3.08(\pm 0.82) \times T(℃) + 85.58(\pm 7.66)$	6-16.4	23
This Study	Isididae	$1.64(\pm 3.84) \times T(℃) + 96.87(\pm 26.38)$	5-8.4	5
Weinbauer et al. 2000	Corallidae (*C. rubrum*)	$5.03(\pm 1.14) \times T(℃) + 39.0(\pm 16.8)$	13-16	3
Chave 1954 Weinbauer et al. 2000 Yoshimura et al. 2011 Thresher et al. 2016	Corallidae (*Corallium* spp.)	$3.08(\pm 0.56) \times T(℃) + 70.9(\pm 7.32)$	0-19.5	17
Chaabane et al. 2019	Corallidae (*C. rubrum*)	$2.89(\pm 0.59) \times T(℃) + 73.98(\pm 9.09)$	13.8-16.8	12
Yoshimura et al. 2011 Vielzeuf et al. 2013 Chaabane et al. 2019	Corallidae (*Corallium* spp.)	$3.71(\pm 0.23) \times T(℃) + 66.89(\pm 3.21)$	2.5-19.5	24
Thresher et al. 2016	Isididae	$2.93(\pm 0.25) \times T(℃) + 72.1(\pm 2.46)$	-1.9-26.8	73
Mucci 1987	Inorganic Mg-calcite	$3.16(\pm 0.28) \times T(℃) + 42(\pm 0.92)$	5-40	3

Note: Compiled Mg-temperature data was generated by Thresher et al. (2016) and Chaabane et al. (2019), respectively.

Table 8: Summary statistics of PCA conducted on oceanographic parameters and octocoral Mg content, FWHM, and residual FWHM with respect to octocoral species and depth/potential density including relative contributions (%) between individual variables and PC axes.

Variable	**PC1**	**PC2**	**PC3**	**PC4**	**PC5**
Depth	**10.2014**	5.5885	7.6386	8.0049	0.2019
Potential Density	12.2278	0.1619	0.7665	0.9510	**16.9993**
Temperature	**12.2850**	1.0430	0.2823	0.3165	11.2862
Salinity	0.6764	41.0360	7.5356	**48.8939**	0.0251
pH	**12.3813**	0.2460	0.1218	2.7925	4.7071
TA	5.1994	20.5409	14.6958	**26.7374**	4.8630
[CO_3^{2-}]	**12.3939**	0.6472	0.4085	2.3984	0.2972
Ω_{Cal}	**12.4406**	0.6205	0.2682	2.2223	0.5286
Octocoral $MgCO_3$	10.5371	1.1207	13.8762	0.6892	**19.1000**
Octocoral FWHM	11.6380	1.6870	0.2858	3.2210	**36.8623**
Octocoral Residual FWHM	0.0190	27.3083	**54.1207**	3.7728	5.1293
Summary Statistics					
Standard Deviation	2.7959	1.3178	0.9663	0.5792	0.3508
Proportion of Variance	0.7107	0.1579	0.0849	0.0305	0.0011
Cumulative Proportion	0.7107	0.8685	0.9534	0.9839	0.9951

FIGURES

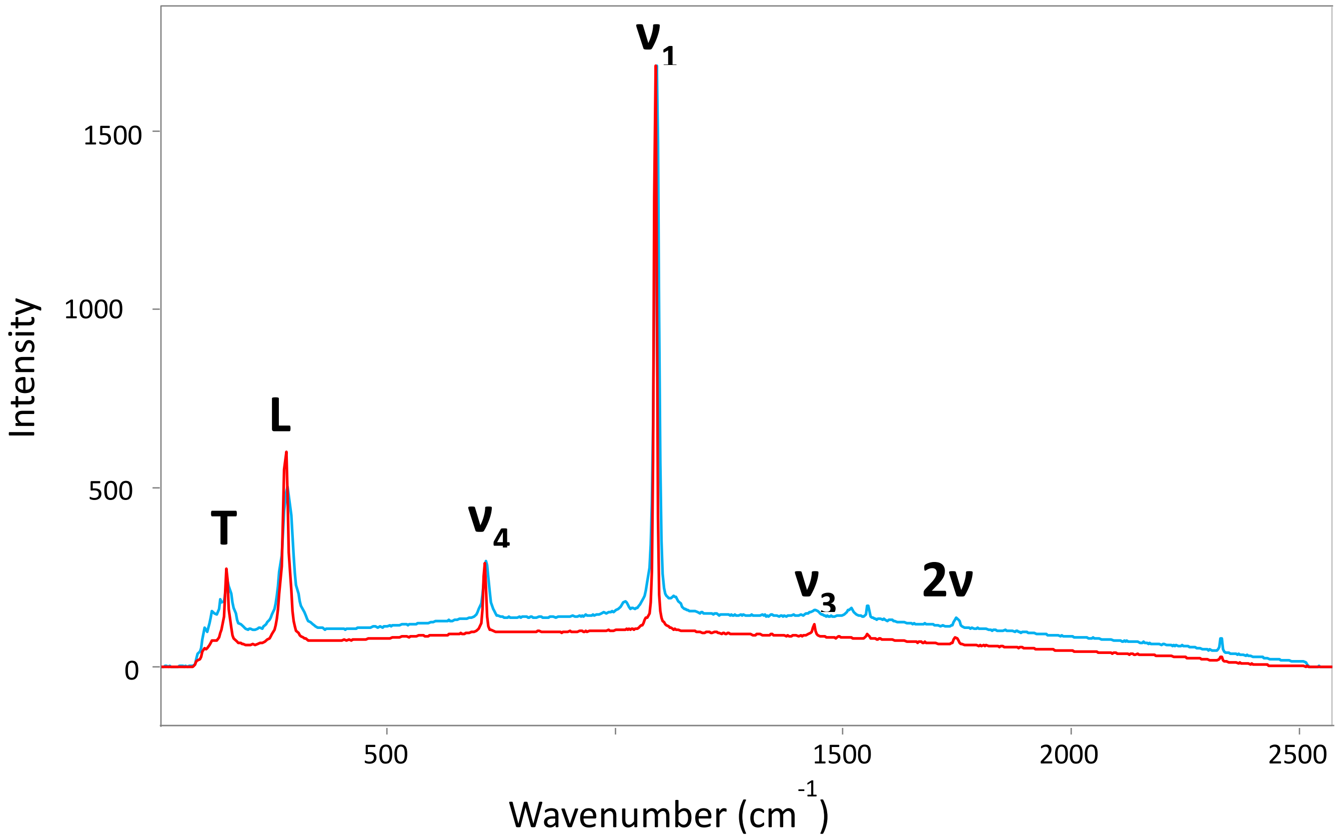

Figure 1. Raman spectra of synthetic (red) and biogenic (blue, *H. imperiale/laauense* from 447 m) calcite with lattice and internal modes labelled.

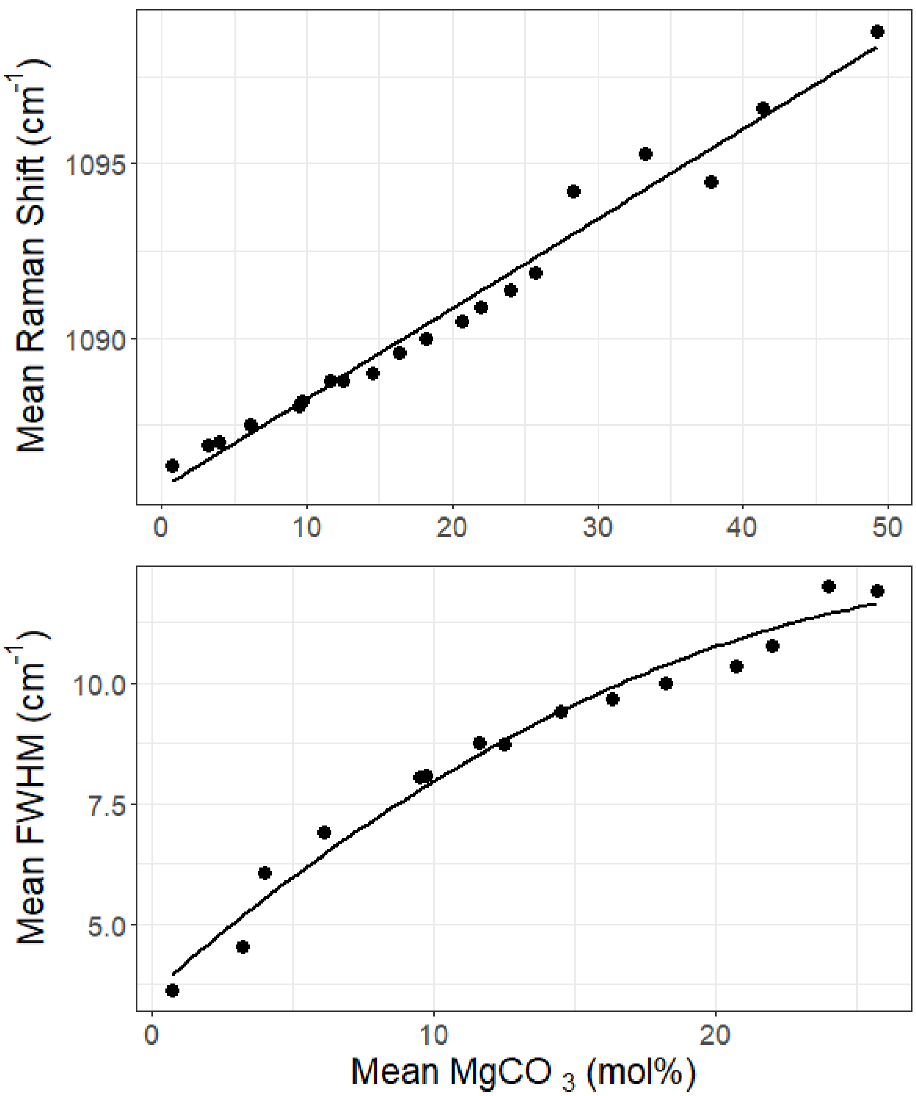

Figure 2. Raman spectral data (Raman shift and FWHM) from the ν_1 peak as a function of Mg content within synthetically produced Mg-calcites. Data and trendlines are from Perrin et al. (2016).

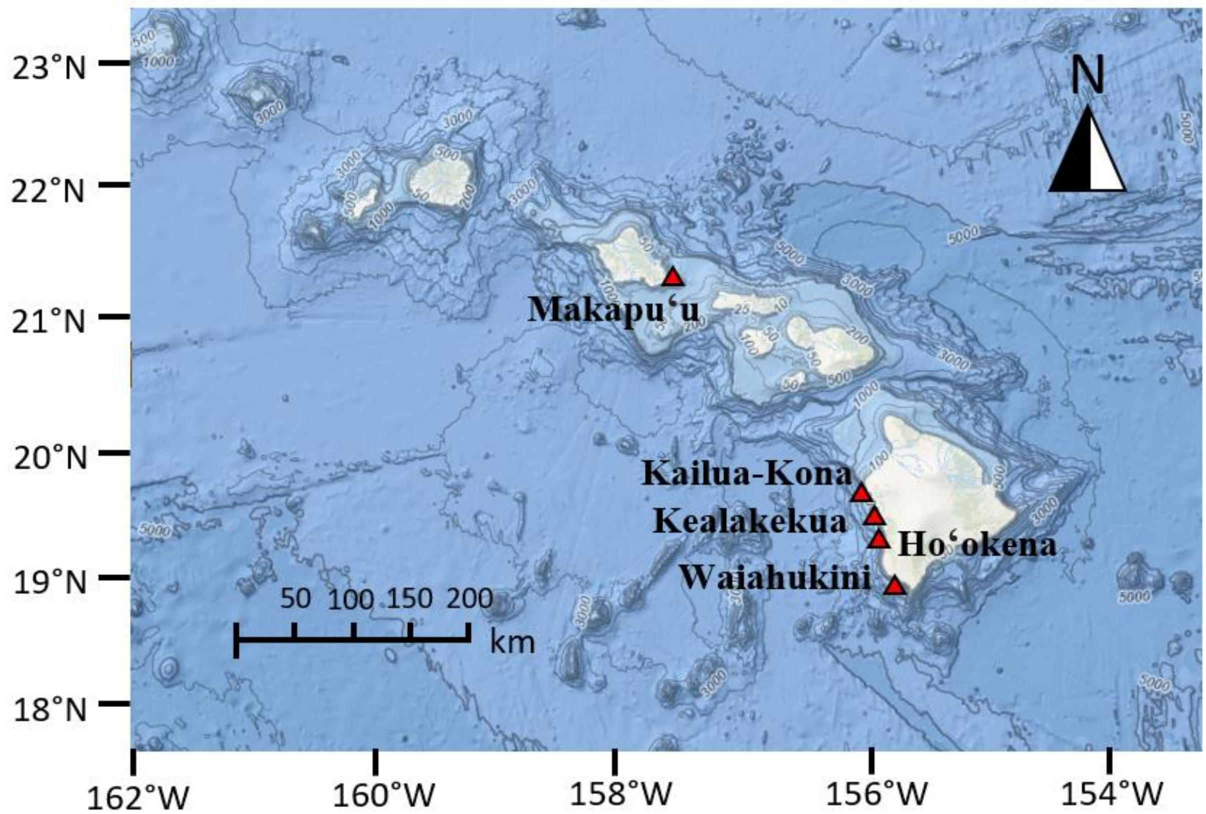

Figure 3. Octocoral and oceanographic sampling sites including the Makapu‘u site for sample M3.

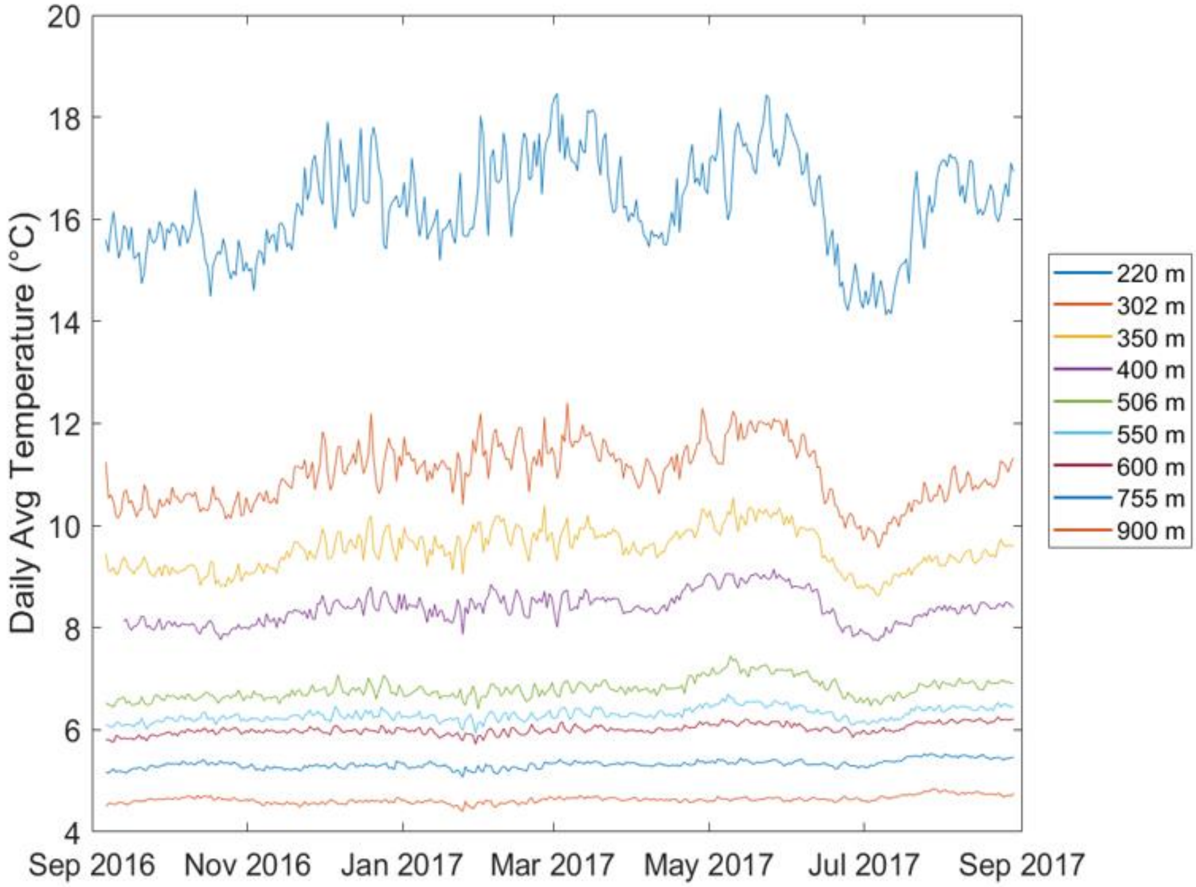

Figure 4: In situ temperature (24-hour averages) along the seafloor at Kailua-Kona for 12 months (Sep 2016–Aug 2017), color coded by depth in meters. The temperature decrease in June is thought to be caused by an anticyclonic mesoscale eddy.

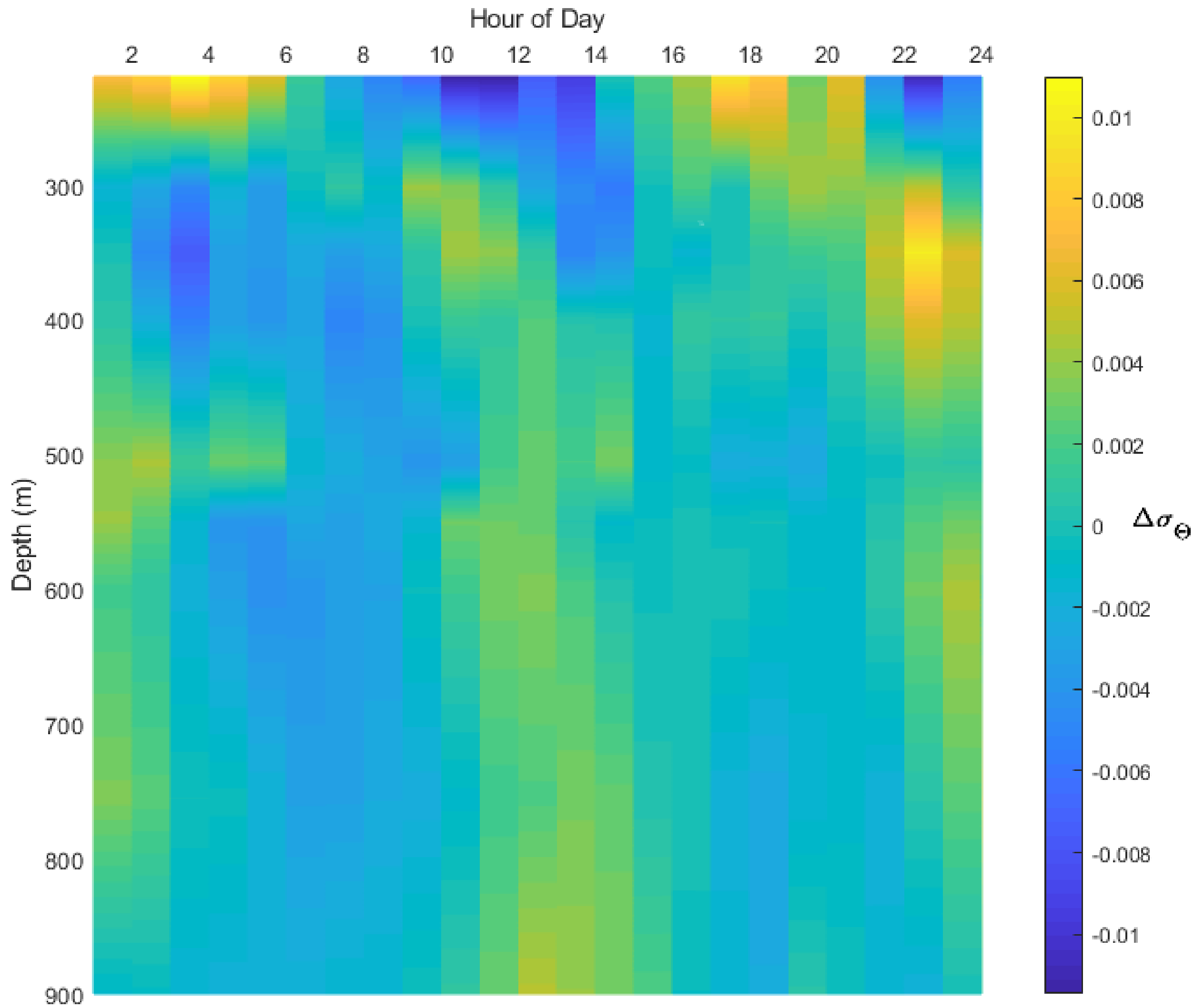

Figure 5: Interpolated color map of 24-hour averaged change in potential density $\Delta\sigma_\theta$ (difference between measured potential density and average potential density for the entire time-series, kg/m^3) observed at different depths.

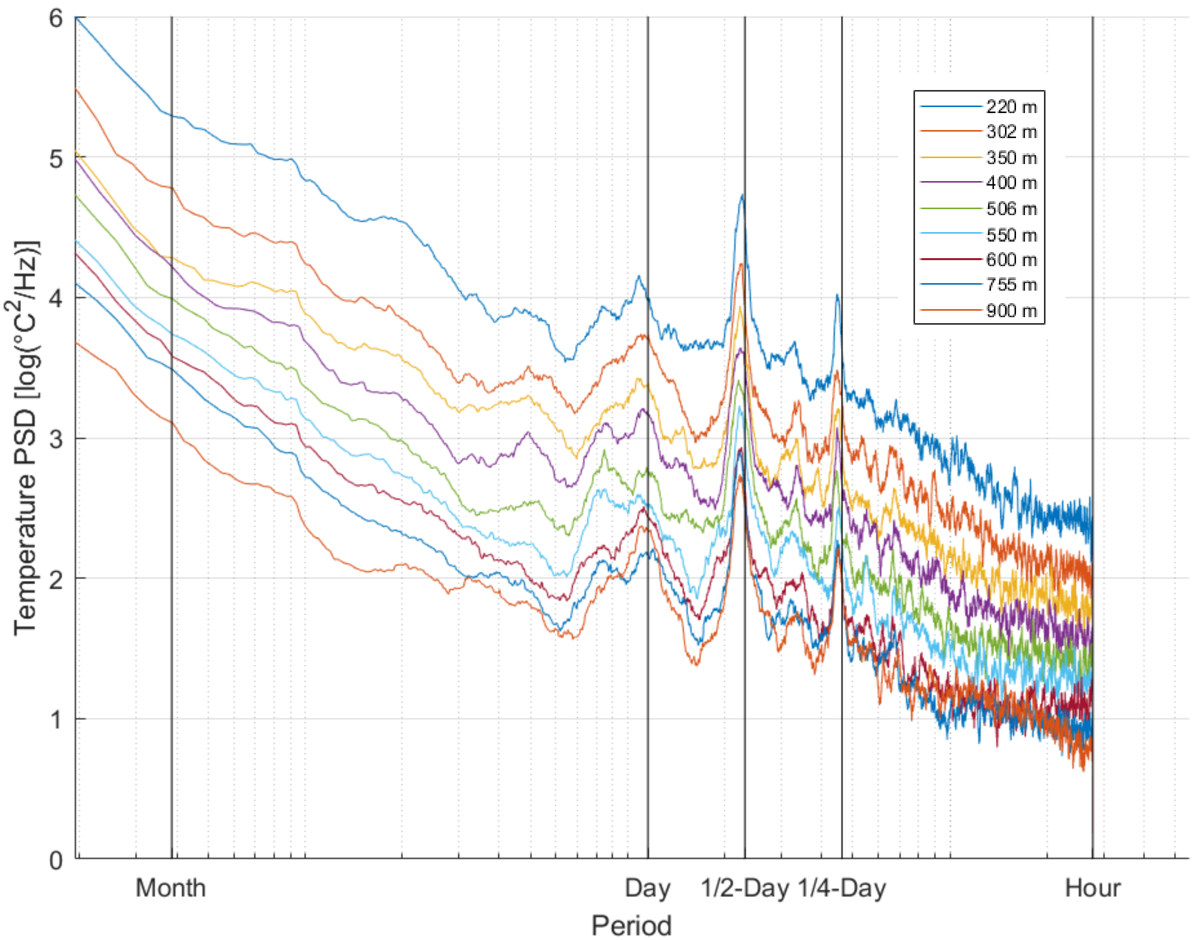

Figure 6: Power spectral density (log-transformed) of in situ temperature data collected from Kailua-Kona for 12 months (Sep 2016 to Aug 2017), color coded by depth in meters. A low pass moving average filter was used to smooth the data. Hourly, quarter day, half day (M_2 semidiurnal), daily, and monthly tidal periods are denoted by the black lines. Tidal fluctuations in temperature appear to attenuate exponentially with depth.

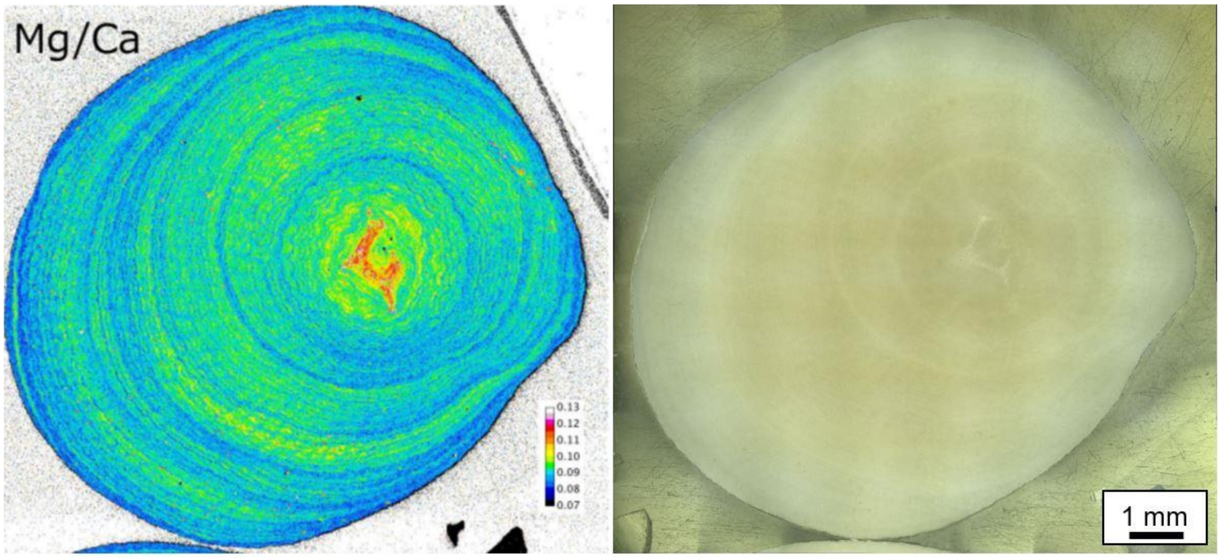

Figure 7: Spatially mapped relative Mg content (color-coded, count/count) of a Corallidae octocoral cross section taken using Electron Microprobe Analysis (EMPA) and a corresponding photograph of the sample (K. Tanaka, unpublished data). The central medullar region of skeleton contains elevated Mg content and is surrounded by annular skeleton.

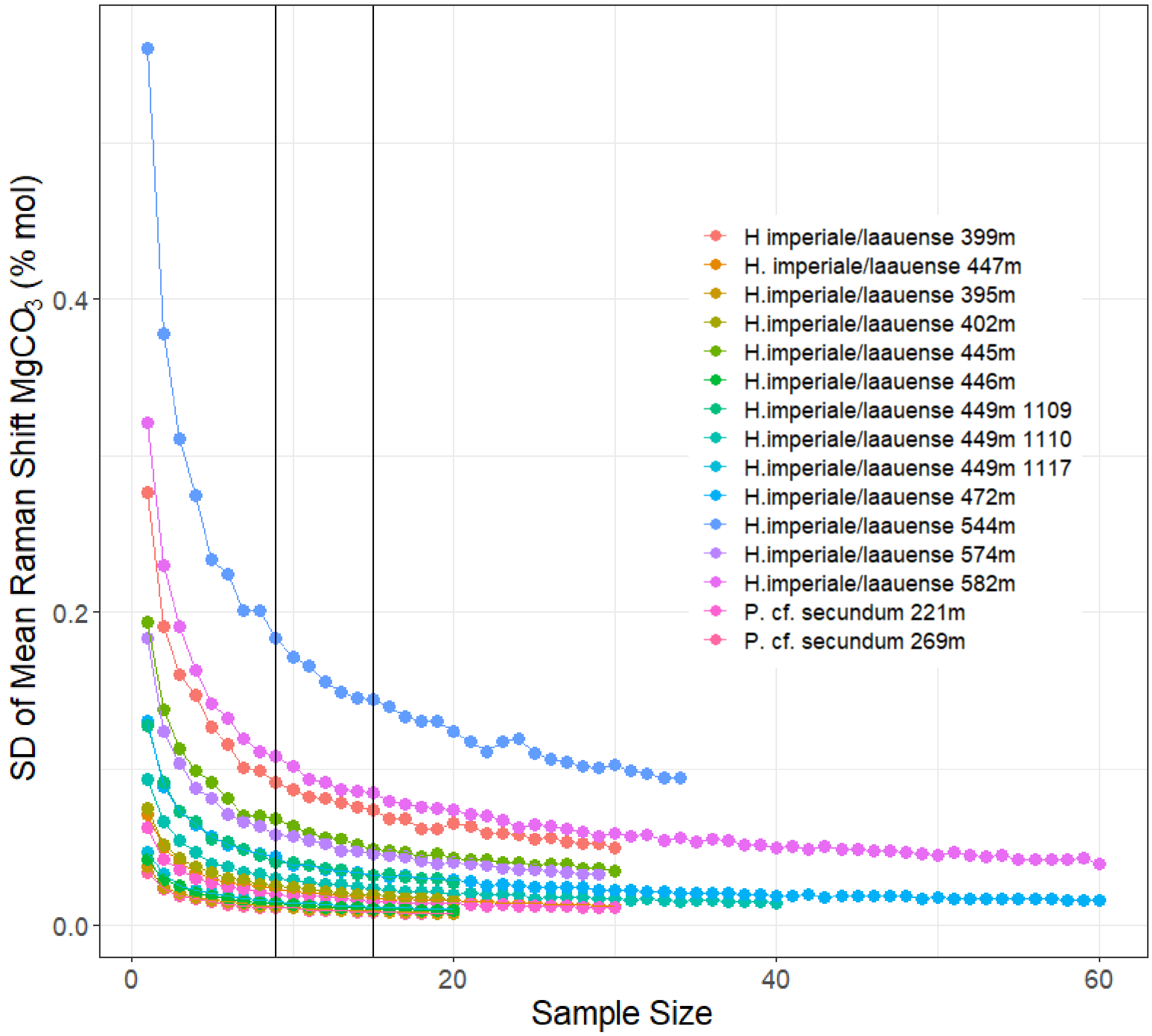

Figure 8: Preliminary sample size analysis of Raman measurements on various octocoral sample surfaces. A bootstrap simulation was conducted containing 1000 iterations where the mean and standard deviation (SD) of Mg content calculated from Raman shift measurements were taken for each iteration. The SD of those 1000 mean values represents the bootstrapped standard error of the mean. Black vertical lines represent sample sizes of 9 and 15.

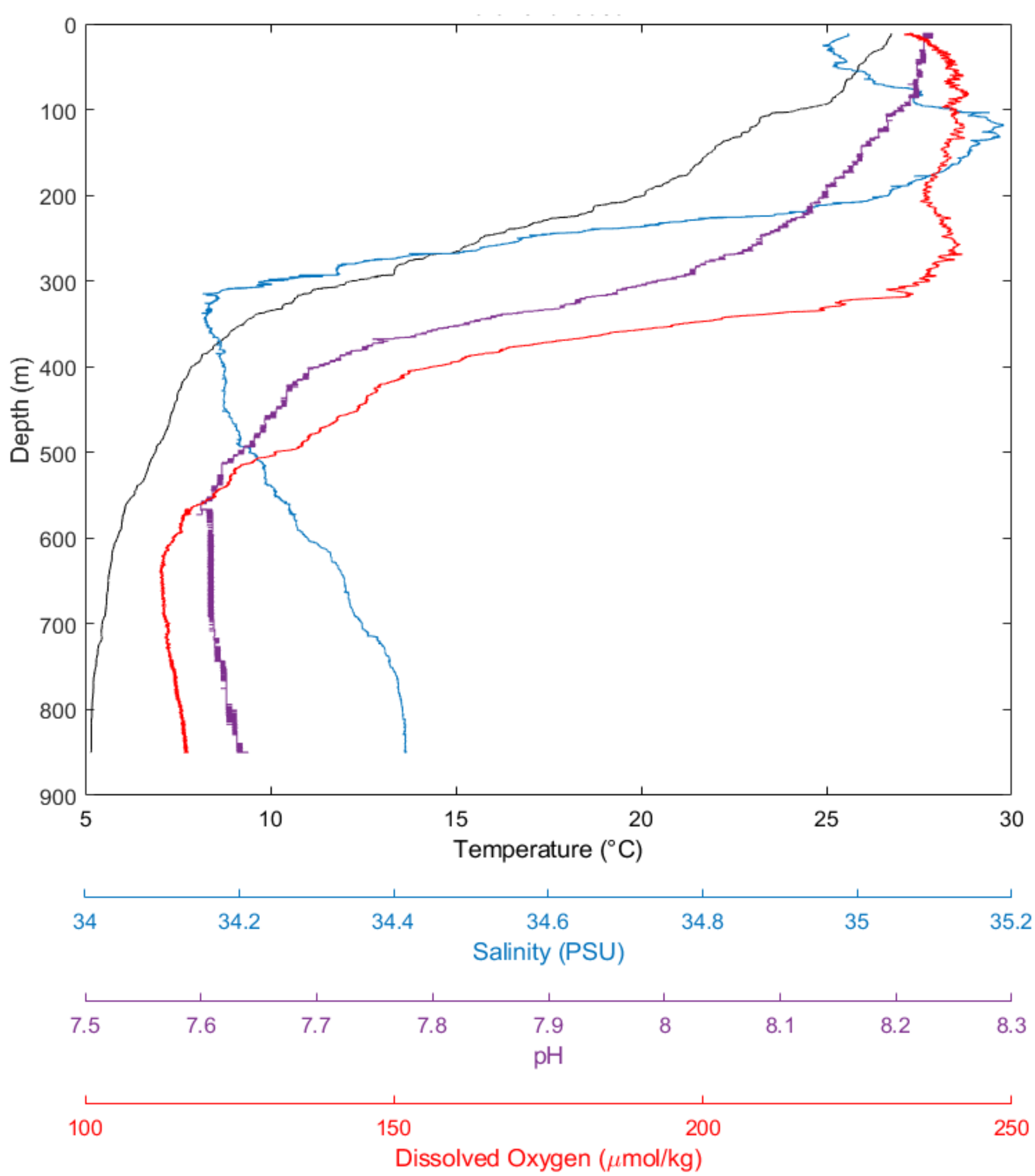

Figure 9: An example of CTD data collected off Hoʻokena (19°12'N, 155°56'W) containing temperature, salinity, pH, and dissolved oxygen data.

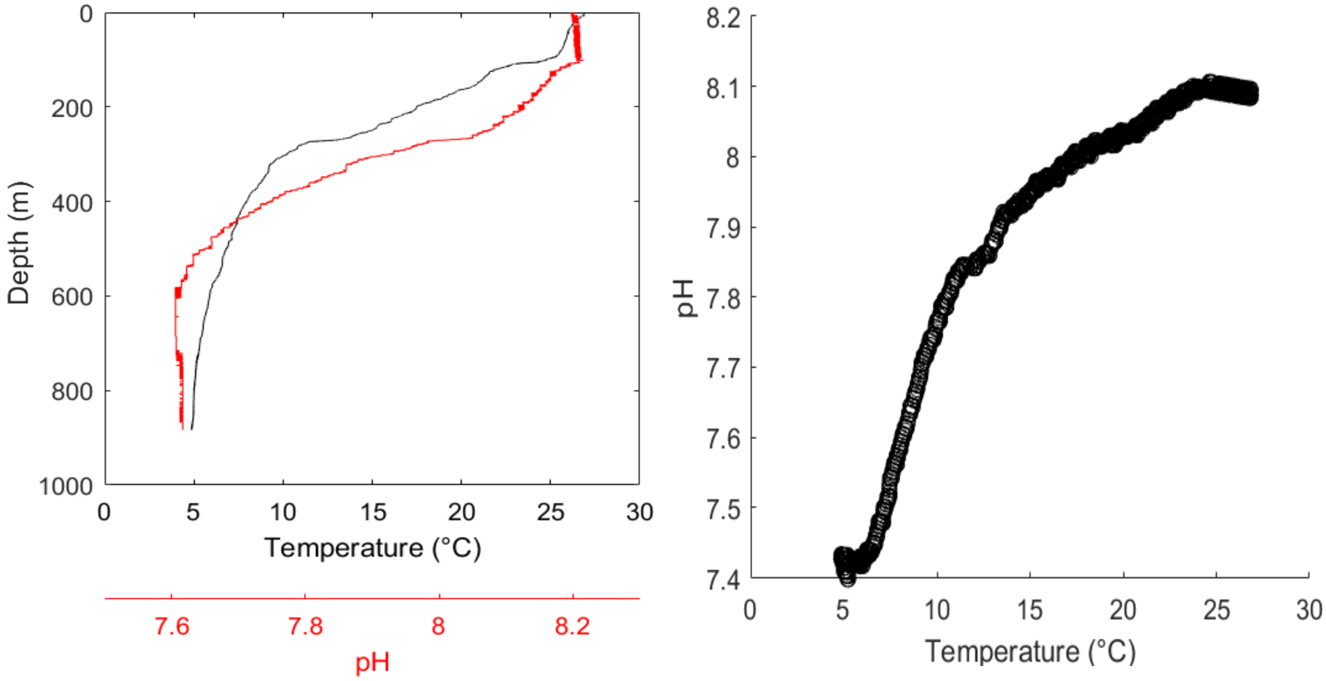

Figure 10: A comparison of temperature and pH data collected from a CTD hydrocast in the Kealakekua Bay site (19°28’N, 155°57’W). Collinearity between the two parameters is apparent and can be a common phenomenon in oceanographic depth profile data. Temperature and pH had a correlation of R^2 = 0.95.

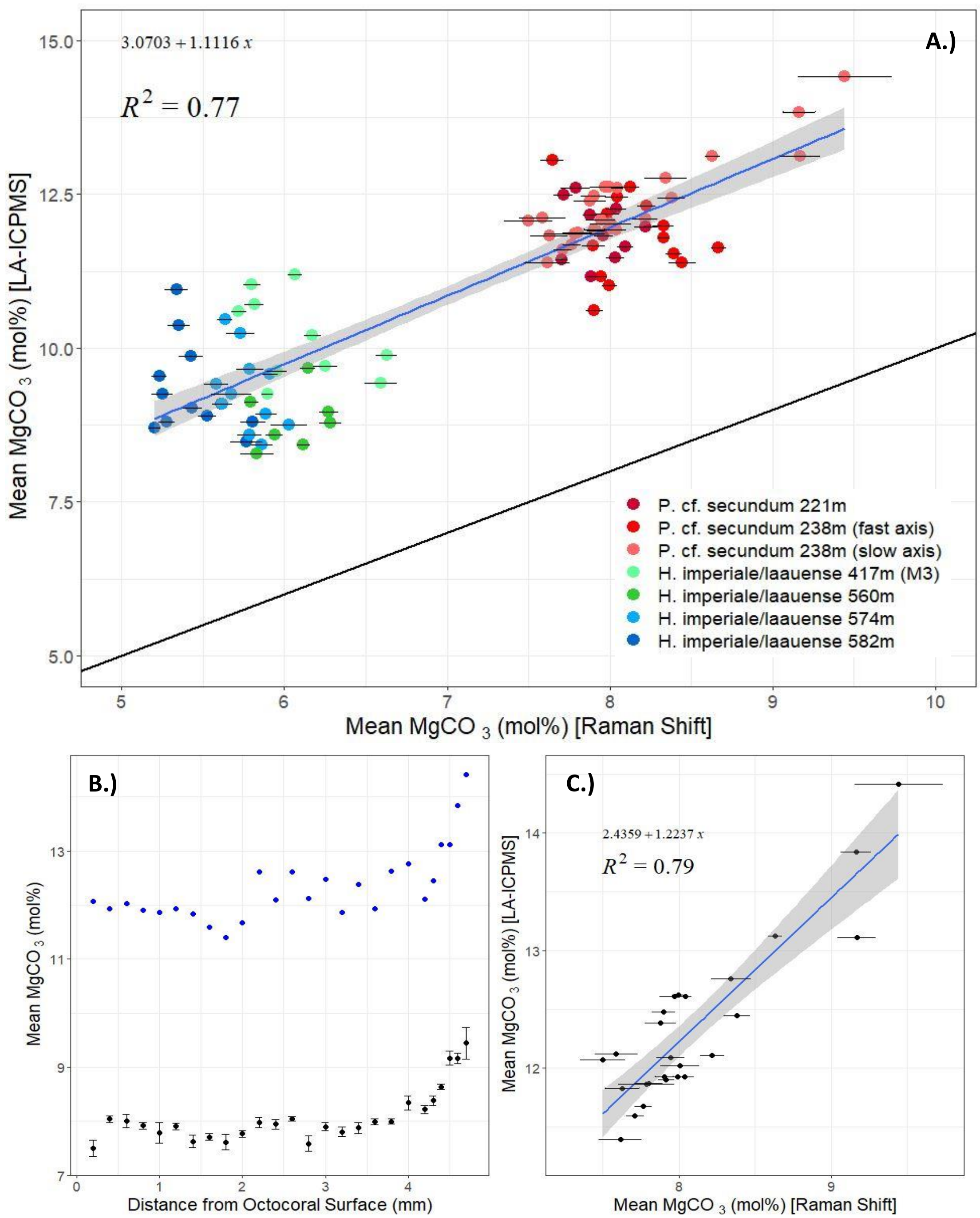

Figure 11. (a) Relationship between skeletal Mg content calculated from Raman shift (Perrin et al. 2016) and Mg measured using LA-ICPMS. The 1:1 line is shown in black. **(b)** Radial measurements of octocoral Mg content from *P.* cf. *secundum* 238 m (slow-axis) taken using Raman (black) and LA-ICPMS (blue) **(c)** as well as the relationship between the two. All error bars represent ±1 SD with the shaded regions representing the 95% CI.

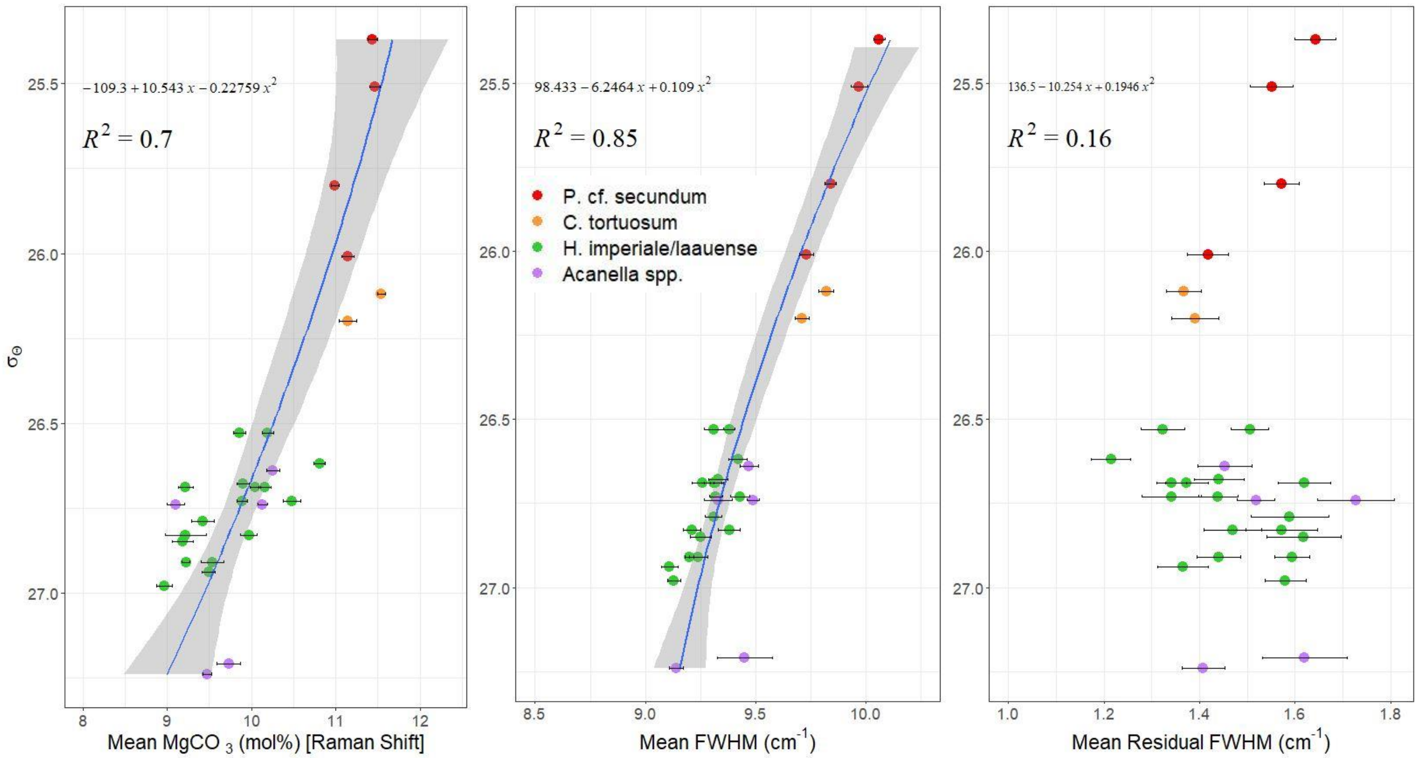

Figure 12. Mean Mg content, FWHM, and residual FWHM of octocoral surface skeleton with respect to potential density (an analog of depth). A 2nd degree polynomial was used for the trendline with error bars representing ±1 SD and the shaded regions representing the 95% CI.

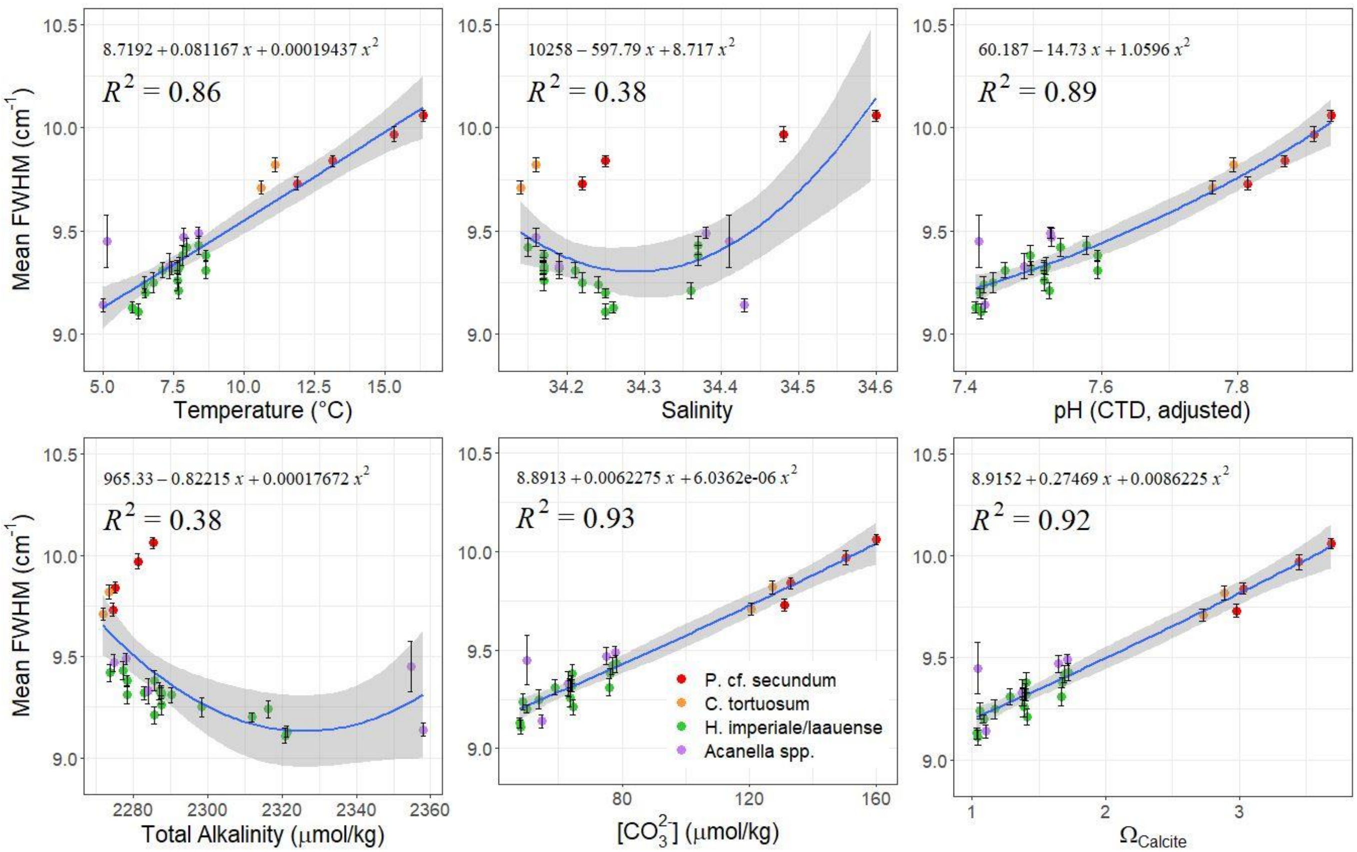

Figure 13. Mean FWHM of octocoral surface skeleton and its relationships with major oceanographic variables covered in this study. A 2nd degree polynomial was used for the trendline with error bars representing ±1 SD and the shaded regions representing the 95% CI.

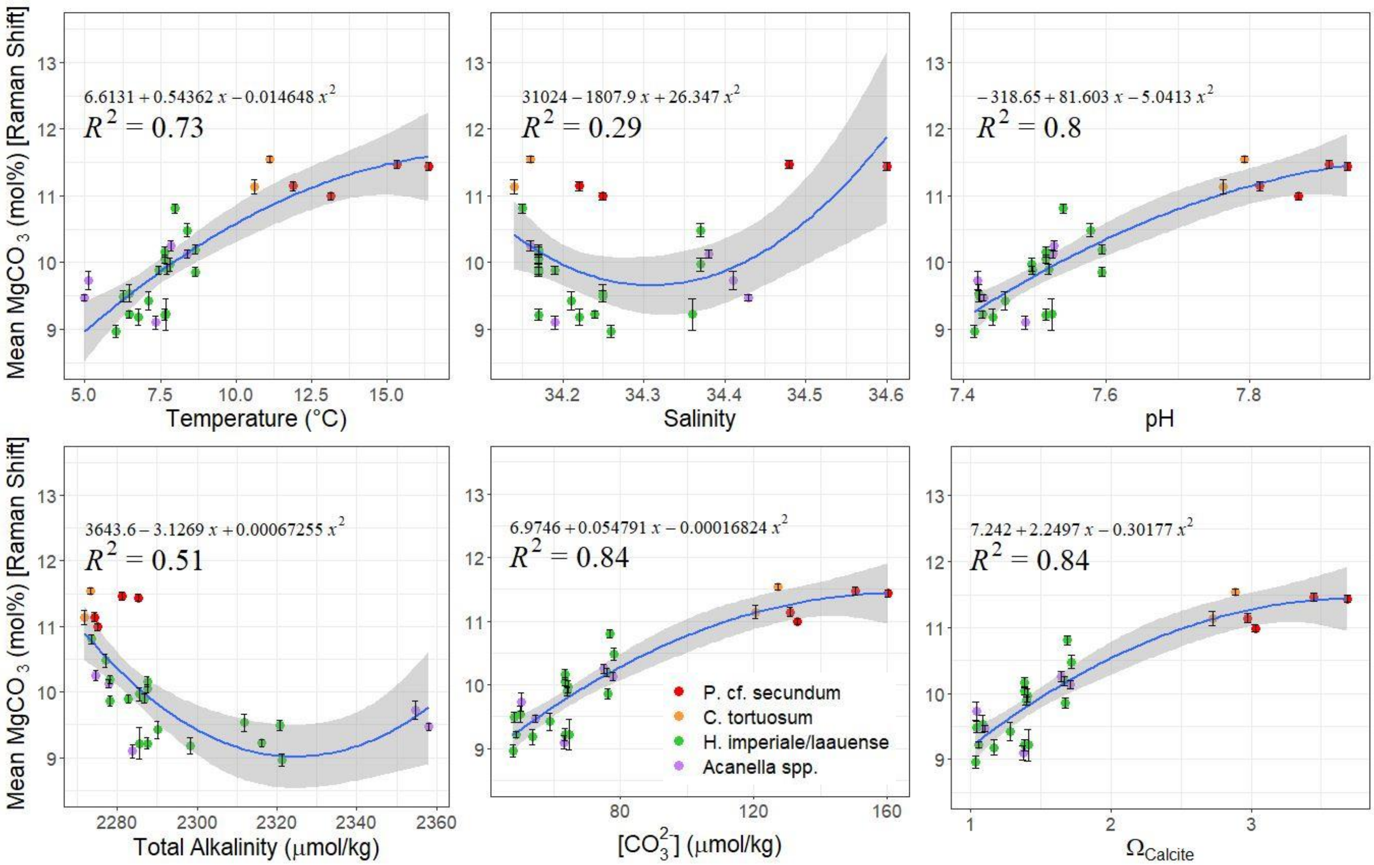

Figure 14. Mean Mg content of octocoral surface skeleton and its relationships with major oceanographic variables covered in this study. A 2nd degree polynomial was used for the trendline with error bars representing ±1 SD and the shaded regions representing the 95% CI.

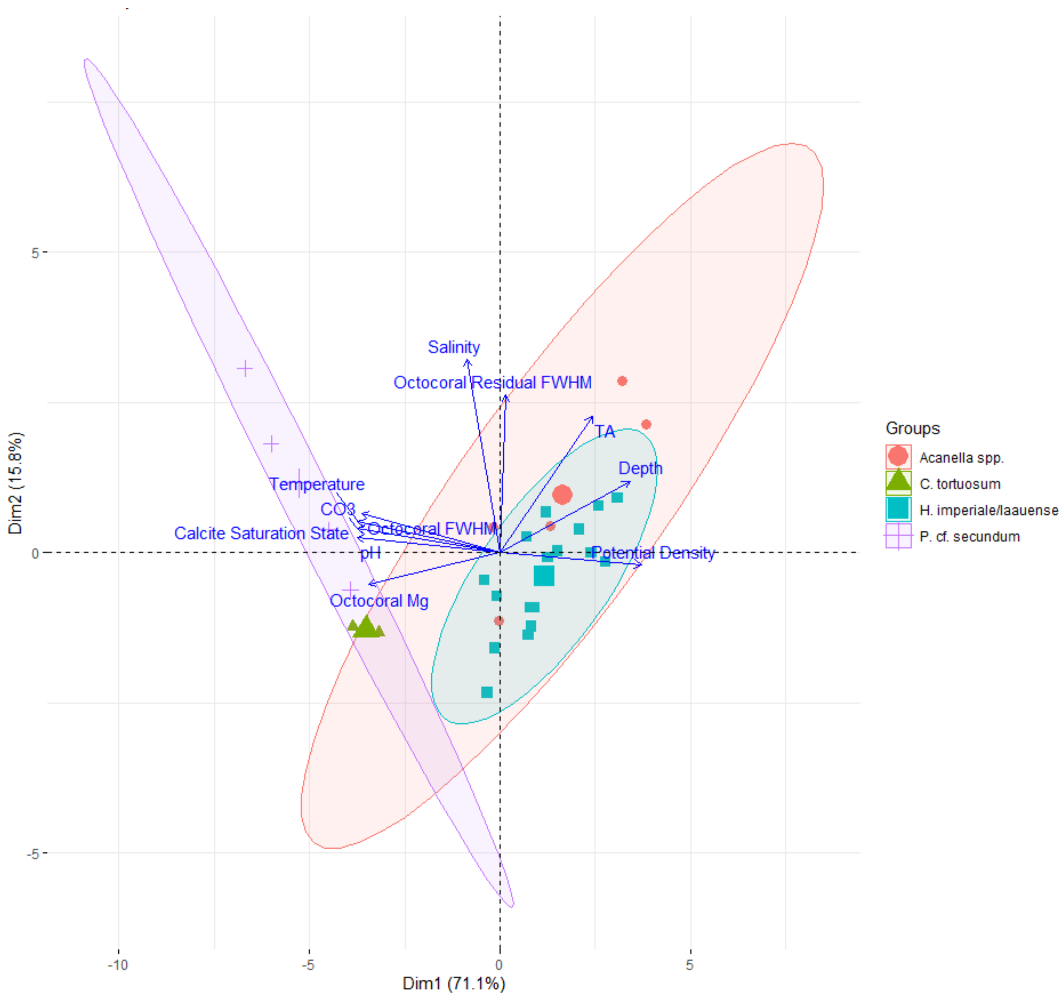

Figure 15: Principal component analysis (PCA) of oceanographic parameters and octocoral Mg content, FWHM, and residual FWHM with respect to octocoral species and depth/potential density. Data points more aligned with the direction of specific variable vectors (e.g., *P.* cf. *secundum* and CO_3^{2-}) are positively correlated while points in the opposite direction are negatively correlated. The first axis (likely temperature, carbonate parameters, FWHM, Mg content, and potential density) explains 71.1% of the patterns in the data while the second axis (salinity, residual FWHM) explains 15.8%. Concentration ellipses represent the 95% CI. A PERMANOVA test (adonis2 R function) found that different species experienced significantly different FWHM, Mg content, and environmental conditions ($F_{1,26} = 21.46$, $P = 0.001$).

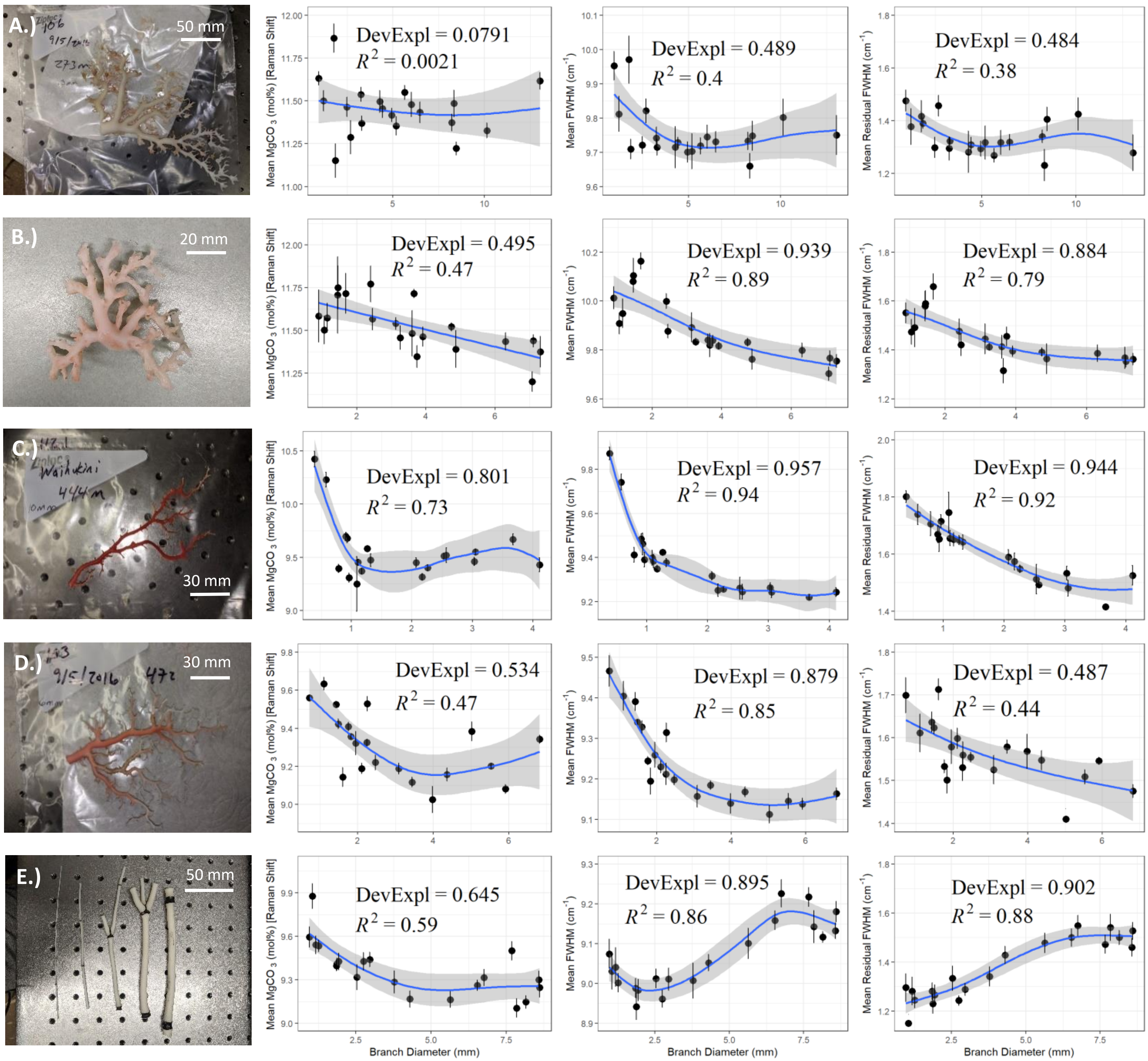

Figure 16. Mean intra-sample octocoral Mg content, overall FWHM, and residual FWHM with respect to octocoral branch diameter for five specific samples **(a)** *P.* cf. *secundum* from 273 m; **(b)** *C. tortuosum* from 280 m; **(c)** *H. imperiale/laauense* from 444 m; **(d)** *H. imperiale/laauense* from 472 m; **(e)** *Acanella* spp. from 823 m. A general additive model was used for the trendlines where error bars are ±1 SD, shaded regions are the 95% CI, and DevExpl represents the deviance explained by the model.

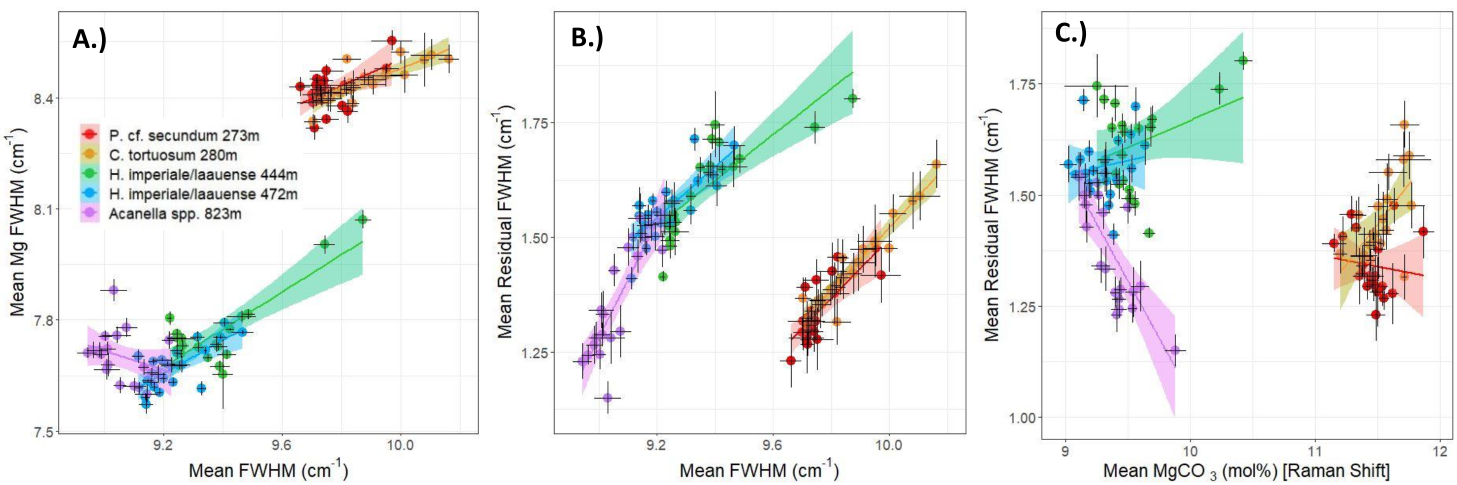

Figure 17. (a) Mean FWHM compared to Mean Mg-based FWHM, **(b)** mean FWHM compared to mean residual FWHM, and **(c)** mean Mg content (from Raman shift) compared to mean residual FWHM for the five octocoral specimens used during the intra-sample variability measurements. Error bars are ±1 SD while shaded regions are the 95% CI.

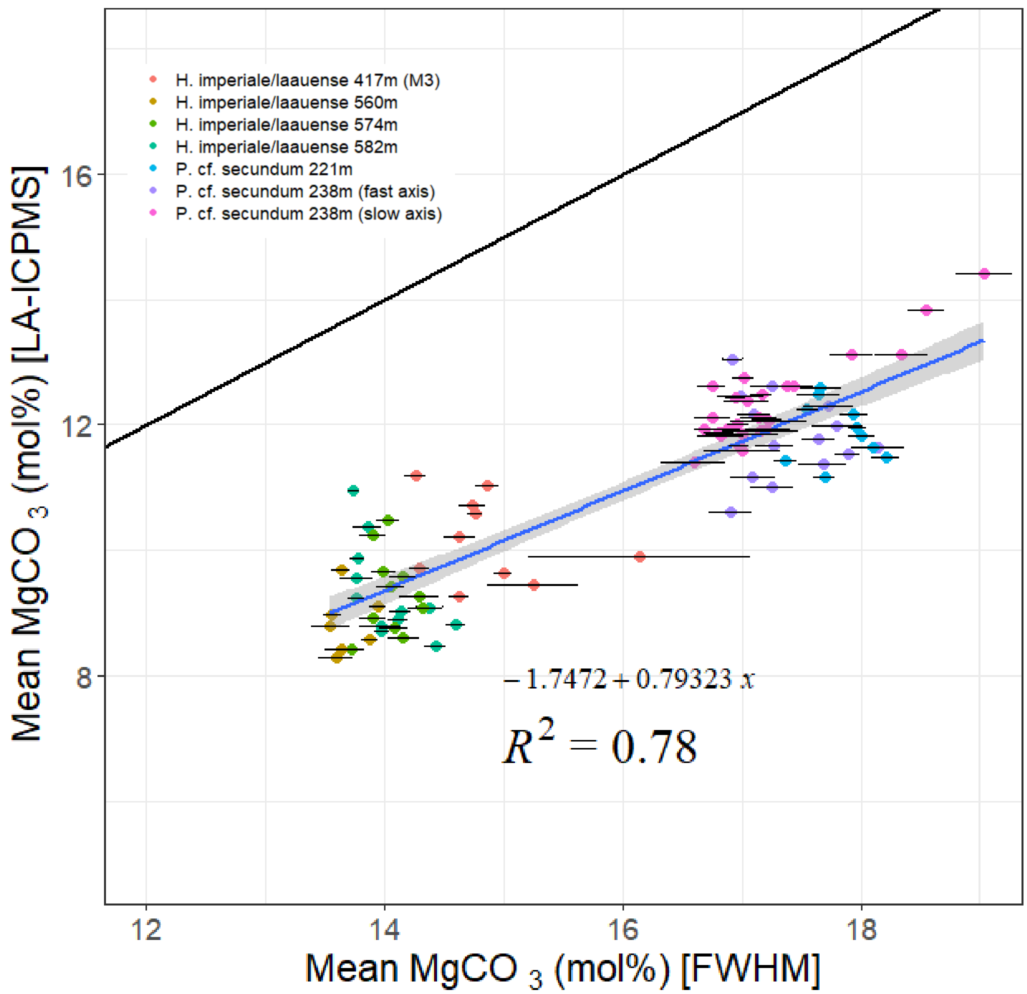

Figure 18: Relationship between skeletal Mg content based on FWHM (Perrin et al. 2016) and Mg measured using LA-ICPMS. The 1:1 line is shown in black.

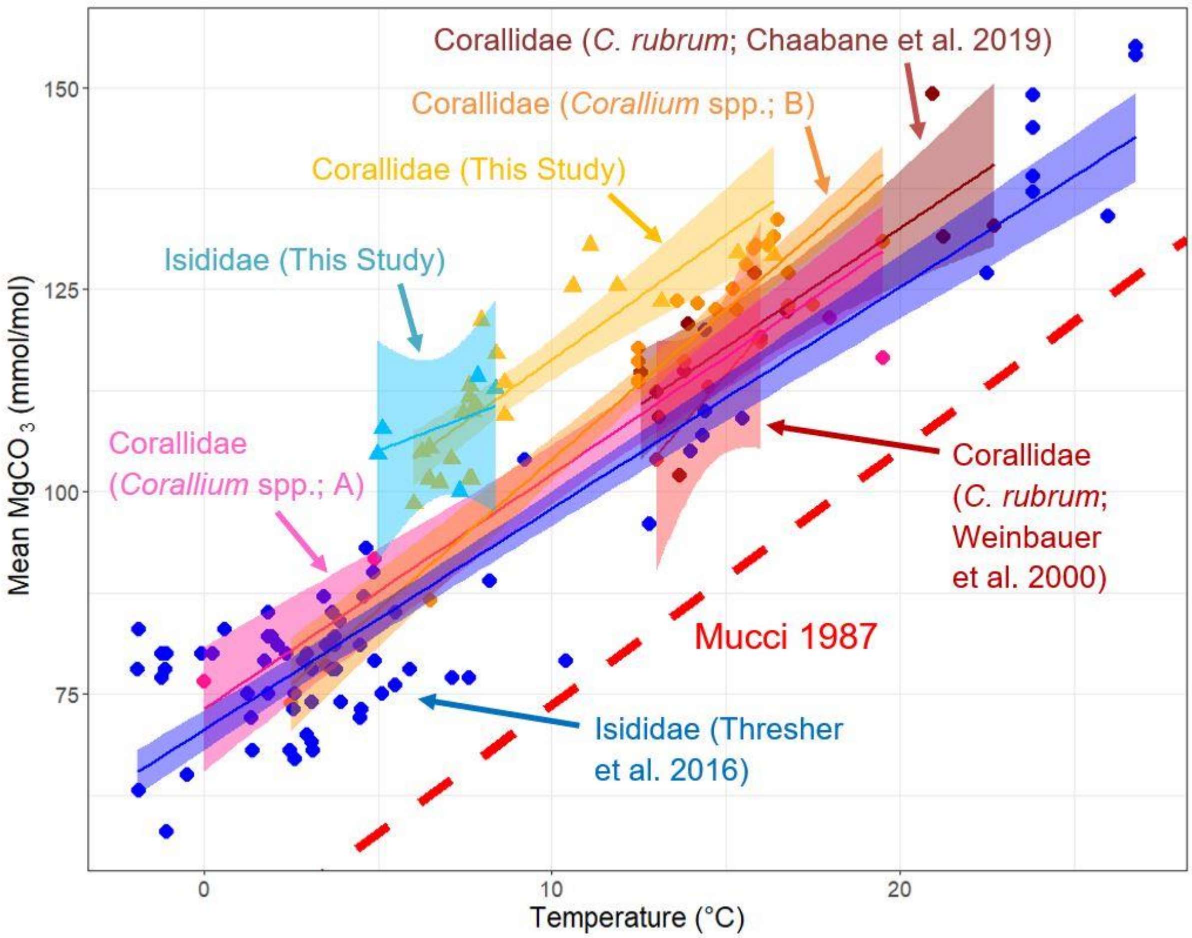

Figure 19: Mg-temperature relationships from this study and other relevant octocoral or inorganic calcite studies (authors annotated). Data from this study are shown with triangle markers. Shaded regions represent the 95% CI around the trendlines. The red dashed line represents the relationship from Mucci (1987).

A: Chave 1954; Weinbauer et al. 2000; Yoshimura et al. 2011; Thresher et al. 2016

B: Yoshimura et al. 2011; Vielzeuf et al. 2013; Chaabane et al. 2019

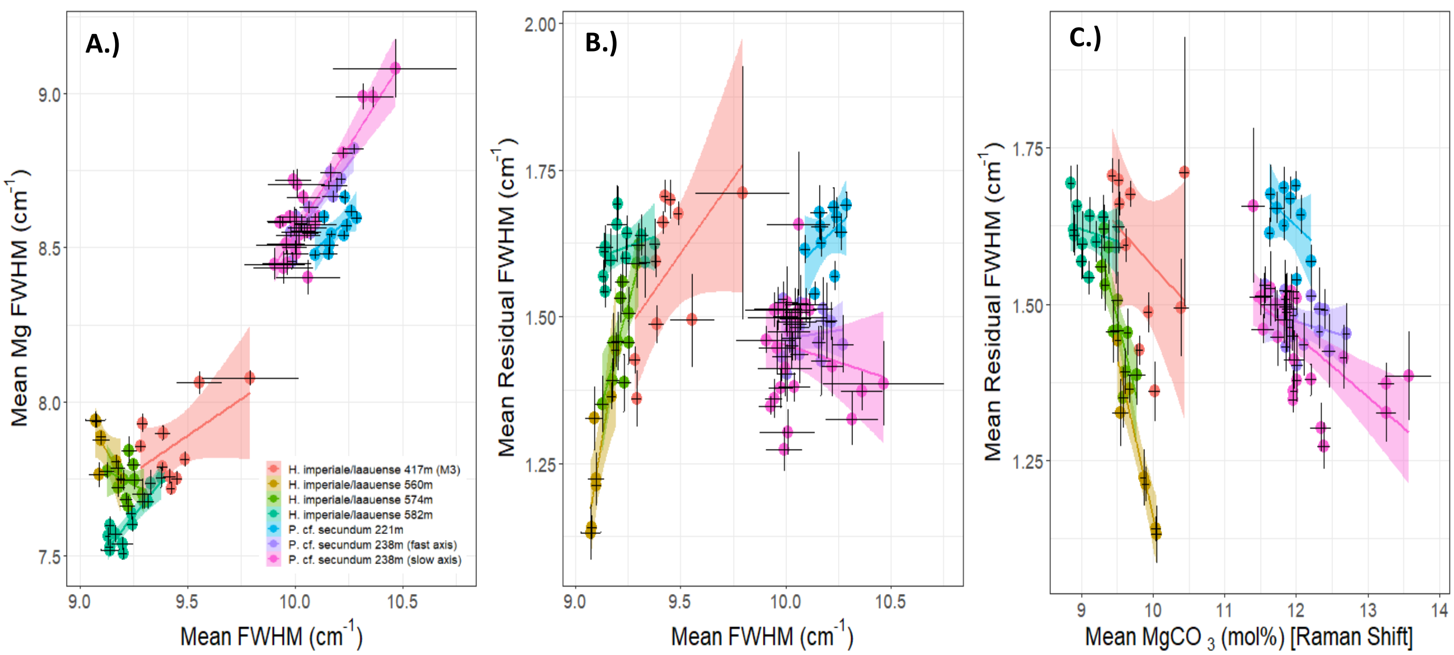

Figure 20: a.) Mean FWHM compared to mean FWHM contributed by Mg content, **b.)** mean FWHM compared to mean residual FWHM, and **c.)** mean Mg content (from Raman shift) compared to mean residual FWHM for the octocorals samples used during the comparison between LA-ICPMS and Raman Mg measurements. Error bars are ±1 SD while shaded regions are the 95% CI.

APPENDIX A: Raw Data Tables

Table A1: Oceanographic data with respect to each octocoral depth gradient sample.

Species	Depth	Adjusted σ_0 (kg/m^3)	Temperature (°C)	Salinity (PSU)	pH	TA (µmol/kg)	[CO_3^{2-}] (µmol/kg)	Ω_{Cal}	[HCO_3^-] (µmol/kg)
P. cf. *secundum*	221	25.37	16.37	34.60	7.94	2285.3	160.04	3.69	1893.3
P. cf. *secundum*	238	25.51	15.33	34.48	7.91	2281.2	133.16	3.03	1950.6
P. cf. *secundum*	269	25.80	13.14	34.25	7.87	2275.1	127.32	2.89	1963.5
P. cf. *secundum*	273	26.01	11.88	34.22	7.82	2274.4	120.63	2.73	1978.4
C. tortuosum	280	26.11	11.1	34.16	7.79	2273.4	77.77	1.71	2083.6
C. tortuosum	293	26.19	10.6	34.14	7.76	2271.8	76.82	1.69	2086.3
H. imp./laau.	395	26.73	8.4	34.37	7.58	2277.1	75.89	1.67	2088.9
Acanella spp.	396	26.74	8.37	34.38	7.53	2277.9	63.54	1.39	2126.2
H. imp./laau.	399	26.62	7.97	34.15	7.54	2273.6	58.97	1.28	2142
H. imp./laau.	401	26.53	8.64	34.17	7.59	2278.3	47.91	1.04	2196.2
H. imp./laau.	402	26.53	8.64	34.17	7.59	2278.3	78.09	1.72	2082.8
Acanella spp.	405	26.64	7.86	34.16	7.53	2274.7	63.54	1.39	2126.2
H. imp./laau.	444	26.83	7.68	34.36	7.52	2285.6	63.54	1.39	2126.2
H. imp./laau.	445	26.83	7.81	34.37	7.50	2285.6	64.43	1.41	2123.3
H. imp./laau.	446	26.73	7.43	34.19	7.50	2282.9	64.21	1.40	2124
H. imp./laau.	447	26.68	7.7	34.17	7.52	2286.9	63.98	1.40	2124.7
H. imp./laau.	449	26.69	7.63	34.17	7.52	2287.5	53.80	1.17	2162.4
H. imp./laau.	449	26.69	7.63	34.17	7.52	2287.5	50.00	1.08	2181.3
H. imp./laau.	449	26.69	7.63	34.17	7.52	2287.5	48.23	1.04	2193.4
Acanella spp.	451	26.74	7.34	34.19	7.49	2283.9	74.97	1.65	2091.5
H. imp./laau.	472	26.79	7.11	34.21	7.46	2290.1	63.11	1.38	2127.6
H. imp./laau.	506	26.85	6.77	34.22	7.44	2298.4	50.20	1.04	2223.2
H. imp./laau.	544	26.91	6.48	34.25	7.42	2311.9	54.68	1.10	2216.8
H. imp./laau.	560	26.91	6.46	34.24	7.43	2316.3	64.66	1.41	2122.5
H. imp./laau.	574	26.94	6.25	34.25	7.42	2320.8	76.20	1.68	2088
H. imp./laau.	582	26.98	6.03	34.26	7.41	2321.3	48.94	1.06	2188
Acanella spp.	753	27.21	5.13	34.41	7.42	2354.7	150.33	3.45	1913.7
Acanella spp.	823	27.24	4.99	34.43	7.43	2358.1	131.02	2.98	1955.3

Note: *Hemicorallium imperiale/laauense* is abbreviated as *H. imp./laau.*

Table A2: Raman shift Mg, LA-ICPMS Mg, and adjusted Raman shift Mg data obtained from the LA-ICPMS Mg correction.

Specimen	Mean Raman Shift Mg (cm^{-1})	SD Raman Shift Mg (cm^{-1})	LA-ICPMS Mg (mol%)	Mean Adjusted Mg (mol%)	SD Adjusted Mg (mol%)
H. imperiale/laauense 417m (M3)	6.59	0.10	9.44	10.40	0.11
H. imperiale/laauense 417m (M3)	6.25	0.07	9.71	10.02	0.08
H. imperiale/laauense 417m (M3)	6.63	0.06	9.89	10.44	0.07
H. imperiale/laauense 417m (M3)	5.95	0.06	9.62	9.69	0.07
H. imperiale/laauense 417m (M3)	5.90	0.03	9.26	9.63	0.04
H. imperiale/laauense 417m (M3)	5.81	0.06	10.71	9.53	0.07
H. imperiale/laauense 417m (M3)	5.72	0.05	10.59	9.43	0.05
H. imperiale/laauense 417m (M3)	5.80	0.05	11.03	9.52	0.06
H. imperiale/laauense 417m (M3)	6.17	0.05	10.21	9.93	0.06
H. imperiale/laauense 417m (M3)	6.07	0.04	11.19	9.81	0.05
H. imperiale/laauense 560m	5.83	0.10	8.29	9.55	0.11
H. imperiale/laauense 560m	6.12	0.04	8.42	9.87	0.05
H. imperiale/laauense 560m	5.94	0.05	8.59	9.67	0.06
H. imperiale/laauense 560m	6.28	0.07	8.78	10.05	0.08
H. imperiale/laauense 560m	5.80	0.04	9.12	9.51	0.05
H. imperiale/laauense 560m	6.14	0.05	9.68	9.90	0.05
H. imperiale/laauense 560m	6.27	0.06	8.97	10.04	0.06
H. imperiale/laauense 574m	5.86	0.07	8.42	9.59	0.07
H. imperiale/laauense 574m	5.89	0.06	8.93	9.61	0.07
H. imperiale/laauense 574m	6.03	0.11	8.76	9.77	0.12
H. imperiale/laauense 574m	5.91	0.05	9.58	9.64	0.05
H. imperiale/laauense 574m	5.79	0.07	8.59	9.50	0.08
H. imperiale/laauense 574m	5.62	0.06	9.09	9.32	0.07
H. imperiale/laauense 574m	5.67	0.12	9.26	9.38	0.14
H. imperiale/laauense 574m	5.79	0.08	9.67	9.50	0.09
H. imperiale/laauense 574m	5.73	0.09	10.23	9.44	0.10
H. imperiale/laauense 574m	5.64	0.05	10.47	9.33	0.05
H. imperiale/laauense 574m	5.58	0.07	9.42	9.28	0.08
H. imperiale/laauense 582m	5.77	0.10	8.47	9.48	0.11
H. imperiale/laauense 582m	5.81	0.08	8.81	9.53	0.09
H. imperiale/laauense 582m	5.61	0.06	9.09	9.31	0.06
H. imperiale/laauense 582m	5.52	0.06	8.90	9.21	0.06
H. imperiale/laauense 582m	5.44	0.06	9.03	9.11	0.06
H. imperiale/laauense 582m	5.28	0.05	8.80	8.94	0.06
H. imperiale/laauense 582m	5.20	0.04	8.70	8.85	0.04
H. imperiale/laauense 582m	5.25	0.06	9.25	8.91	0.07
H. imperiale/laauense 582m	5.23	0.05	9.55	8.89	0.05
H. imperiale/laauense 582m	5.42	0.07	9.87	9.10	0.08
H. imperiale/laauense 582m	5.35	0.07	10.36	9.02	0.08
H. imperiale/laauense 582m	5.34	0.07	10.95	9.00	0.08
P. cf. secundum 221m	8.03	0.05	11.48	12.00	0.06
P. cf. secundum 221m	8.22	0.07	11.97	12.21	0.08
P. cf. secundum 221m	7.96	0.06	11.82	11.92	0.06
P. cf. secundum 221m	8.09	0.05	11.65	12.07	0.06
P. cf. secundum 221m	8.04	0.06	12.26	12.01	0.07
P. cf. secundum 221m	7.88	0.04	12.16	11.83	0.05
P. cf. secundum 221m	7.88	0.03	11.16	11.84	0.03
P. cf. secundum 221m	7.79	0.09	12.61	11.73	0.10
P. cf. secundum 221m	7.70	0.04	11.44	11.63	0.04
P. cf. secundum 221m	7.71	0.06	12.49	11.64	0.07
P. cf. secundum 238m (fast axis)	8.67	0.05	11.63	12.71	0.05
P. cf. secundum 238m (fast axis)	8.44	0.08	11.38	12.46	0.09
P. cf. secundum 238m (fast axis)	8.22	0.05	12.31	12.21	0.06
P. cf. secundum 238m (fast axis)	8.39	0.05	11.53	12.40	0.06
P. cf. secundum 238m (fast axis)	8.33	0.07	11.98	12.33	0.07

P. cf. secundum 238m (fast axis)	8.33	0.04	11.79	12.33	0.04
P. cf. secundum 238m (fast axis)	7.90	0.07	11.66	11.85	0.08
P. cf. secundum 238m (fast axis)	8.00	0.05	11.01	11.96	0.05
P. cf. secundum 238m (fast axis)	7.94	0.04	11.17	11.90	0.04
P. cf. secundum 238m (fast axis)	7.90	0.05	10.61	11.86	0.06
P. cf. secundum 238m (fast axis)	8.04	0.07	12.46	12.01	0.08
P. cf. secundum 238m (fast axis)	8.13	0.06	12.61	12.10	0.06
P. cf. secundum 238m (fast axis)	7.99	0.07	12.18	11.95	0.08
P. cf. secundum 238m (fast axis)	7.65	0.07	13.06	11.57	0.08
P. cf. secundum 238m (slow axis)	7.50	0.15	12.07	11.41	0.17
P. cf. secundum 238m (slow axis)	8.04	0.06	11.93	12.01	0.07
P. cf. secundum 238m (slow axis)	8.01	0.13	12.02	11.97	0.14
P. cf. secundum 238m (slow axis)	7.92	0.06	11.90	11.87	0.06
P. cf. secundum 238m (slow axis)	7.79	0.19	11.86	11.73	0.21
P. cf. secundum 238m (slow axis)	7.90	0.06	11.93	11.85	0.07
P. cf. secundum 238m (slow axis)	7.63	0.11	11.83	11.55	0.13
P. cf. secundum 238m (slow axis)	7.71	0.06	11.59	11.64	0.06
P. cf. secundum 238m (slow axis)	7.61	0.14	11.39	11.53	0.16
P. cf. secundum 238m (slow axis)	7.77	0.06	11.68	11.70	0.06
P. cf. secundum 238m (slow axis)	7.97	0.10	12.61	11.93	0.11
P. cf. secundum 238m (slow axis)	7.95	0.09	12.09	11.90	0.10
P. cf. secundum 238m (slow axis)	8.04	0.04	12.61	12.01	0.04
P. cf. secundum 238m (slow axis)	7.59	0.14	12.12	11.50	0.16
P. cf. secundum 238m (slow axis)	7.90	0.08	12.48	11.85	0.08
P. cf. secundum 238m (slow axis)	7.80	0.09	11.87	11.74	0.10
P. cf. secundum 238m (slow axis)	7.88	0.10	12.39	11.83	0.11
P. cf. secundum 238m (slow axis)	7.99	0.06	11.93	11.95	0.06
P. cf. secundum 238m (slow axis)	8.00	0.04	12.62	11.96	0.05
P. cf. secundum 238m (slow axis)	8.34	0.13	12.76	12.34	0.15
P. cf. secundum 238m (slow axis)	8.22	0.08	12.11	12.20	0.08
P. cf. secundum 238m (slow axis)	8.38	0.08	12.45	12.39	0.09
P. cf. secundum 238m (slow axis)	8.63	0.05	13.12	12.67	0.05
P. cf. secundum 238m (slow axis)	9.17	0.12	13.11	13.26	0.14
P. cf. secundum 238m (slow axis)	9.16	0.10	13.84	13.26	0.11
P. cf. secundum 238m (slow axis)	9.44	0.29	14.42	13.57	0.32

Table A3: FWHM and residual FWHM data obtained from the LA-ICPMS Mg correction.

Specimen	Mean FWHM (cm^{-1})	SD FWHM (cm^{-1})	Mean Residual FWHM (cm^{-1})	SD Residual FWHM (cm^{-1})
H. imperiale/laauense 417m (M3)	9.56	0.10	2.93	0.08
H. imperiale/laauense 417m (M3)	9.29	0.02	2.80	0.05
H. imperiale/laauense 417m (M3)	9.79	0.22	3.14	0.22
H. imperiale/laauense 417m (M3)	9.49	0.02	3.12	0.02
H. imperiale/laauense 417m (M3)	9.38	0.02	3.04	0.03
H. imperiale/laauense 417m (M3)	9.42	0.03	3.11	0.02
H. imperiale/laauense 417m (M3)	9.42	0.02	3.15	0.03
H. imperiale/laauense 417m (M3)	9.45	0.03	3.15	0.03
H. imperiale/laauense 417m (M3)	9.39	0.04	2.93	0.03
H. imperiale/laauense 417m (M3)	9.28	0.03	2.87	0.02
H. imperiale/laauense 560m	9.09	0.04	2.77	0.05
H. imperiale/laauense 560m	9.10	0.04	2.66	0.05
H. imperiale/laauense 560m	9.17	0.02	2.81	0.02
H. imperiale/laauense 560m	9.07	0.05	2.57	0.05
H. imperiale/laauense 560m	9.19	0.02	2.89	0.03
H. imperiale/laauense 560m	9.10	0.02	2.65	0.03
H. imperiale/laauense 560m	9.08	0.02	2.58	0.02
H. imperiale/laauense 574m	9.13	0.03	2.80	0.05
H. imperiale/laauense 574m	9.18	0.03	2.84	0.04
H. imperiale/laauense 574m	9.23	0.03	2.83	0.05
H. imperiale/laauense 574m	9.25	0.03	2.90	0.04
H. imperiale/laauense 574m	9.25	0.04	2.95	0.05
H. imperiale/laauense 574m	9.30	0.03	3.07	0.04
H. imperiale/laauense 574m	9.29	0.05	3.04	0.04
H. imperiale/laauense 574m	9.20	0.03	2.91	0.05
H. imperiale/laauense 574m	9.18	0.03	2.91	0.05
H. imperiale/laauense 574m	9.22	0.03	2.98	0.04
H. imperiale/laauense 574m	9.22	0.03	3.01	0.05
H. imperiale/laauense 582m	9.33	0.03	3.04	0.06
H. imperiale/laauense 582m	9.38	0.02	3.07	0.04
H. imperiale/laauense 582m	9.32	0.03	3.09	0.03
H. imperiale/laauense 582m	9.24	0.02	3.05	0.03
H. imperiale/laauense 582m	9.25	0.02	3.10	0.03
H. imperiale/laauense 582m	9.20	0.05	3.11	0.07
H. imperiale/laauense 582m	9.20	0.02	3.15	0.03
H. imperiale/laauense 582m	9.14	0.02	3.07	0.03
H. imperiale/laauense 582m	9.14	0.04	3.08	0.04
H. imperiale/laauense 582m	9.14	0.02	3.00	0.03
H. imperiale/laauense 582m	9.17	0.03	3.05	0.05
H. imperiale/laauense 582m	9.13	0.01	3.02	0.03
P. cf. secundum 221m	10.29	0.03	3.09	0.02
P. cf. secundum 221m	10.23	0.02	2.96	0.03
P. cf. secundum 221m	10.24	0.03	3.07	0.03
P. cf. secundum 221m	10.26	0.03	3.04	0.03
P. cf. secundum 221m	10.14	0.02	2.94	0.02
P. cf. secundum 221m	10.23	0.03	3.09	0.03
P. cf. secundum 221m	10.17	0.02	3.03	0.02
P. cf. secundum 221m	10.16	0.04	3.06	0.03
P. cf. secundum 221m	10.09	0.02	3.02	0.02
P. cf. secundum 221m	10.16	0.04	3.08	0.05
P. cf. secundum 238m (fast axis)	10.27	0.05	2.83	0.05
P. cf. secundum 238m (fast axis)	10.17	0.05	2.81	0.06
P. cf. secundum 238m (fast axis)	10.18	0.05	2.90	0.05
P. cf. secundum 238m (fast axis)	10.22	0.02	2.88	0.03
P. cf. secundum 238m (fast axis)	10.19	0.05	2.88	0.07
P. cf. secundum 238m (fast axis)	10.16	0.03	2.85	0.03
P. cf. secundum 238m (fast axis)	10.07	0.04	2.92	0.05
P. cf. secundum 238m (fast axis)	10.07	0.04	2.88	0.04

P. cf. secundum 238m (fast axis)	10.03	0.05	2.86	0.05
P. cf. secundum 238m (fast axis)	9.98	0.04	2.83	0.04
P. cf. secundum 238m (fast axis)	10.00	0.05	2.80	0.05
P. cf. secundum 238m (fast axis)	10.07	0.04	2.83	0.05
P. cf. secundum 238m (fast axis)	10.03	0.03	2.85	0.02
P. cf. secundum 238m (fast axis)	9.99	0.02	2.94	0.03
P. cf. secundum 238m (slow axis)	10.06	0.15	3.07	0.13
P. cf. secundum 238m (slow axis)	9.98	0.06	2.78	0.04
P. cf. secundum 238m (slow axis)	10.00	0.13	2.81	0.05
P. cf. secundum 238m (slow axis)	10.04	0.06	2.89	0.06
P. cf. secundum 238m (slow axis)	10.01	0.19	2.90	0.02
P. cf. secundum 238m (slow axis)	10.06	0.06	2.91	0.04
P. cf. secundum 238m (slow axis)	9.96	0.11	2.92	0.04
P. cf. secundum 238m (slow axis)	10.01	0.06	2.93	0.06
P. cf. secundum 238m (slow axis)	9.91	0.14	2.87	0.02
P. cf. secundum 238m (slow axis)	10.00	0.06	2.90	0.03
P. cf. secundum 238m (slow axis)	10.10	0.10	2.92	0.03
P. cf. secundum 238m (slow axis)	10.06	0.09	2.89	0.03
P. cf. secundum 238m (slow axis)	10.11	0.04	2.91	0.03
P. cf. secundum 238m (slow axis)	9.95	0.14	2.92	0.03
P. cf. secundum 238m (slow axis)	10.05	0.08	2.90	0.04
P. cf. secundum 238m (slow axis)	9.96	0.09	2.85	0.05
P. cf. secundum 238m (slow axis)	10.02	0.10	2.88	0.04
P. cf. secundum 238m (slow axis)	9.93	0.06	2.75	0.02
P. cf. secundum 238m (slow axis)	9.94	0.04	2.76	0.03
P. cf. secundum 238m (slow axis)	10.01	0.13	2.69	0.04
P. cf. secundum 238m (slow axis)	10.04	0.08	2.77	0.02
P. cf. secundum 238m (slow axis)	9.99	0.08	2.66	0.04
P. cf. secundum 238m (slow axis)	10.22	0.05	2.80	0.05
P. cf. secundum 238m (slow axis)	10.32	0.12	2.69	0.05
P. cf. secundum 238m (slow axis)	10.36	0.10	2.74	0.03
P. cf. secundum 238m (slow axis)	10.47	0.29	2.74	0.08

Table A4: Adjusted $FWHM_{Mg}$ and adjusted residual FWHM data obtained from the LA-ICPMS Mg correction.

Specimen	Mean Adjusted $FWHM_{Mg}$ (cm^{-1})	SD Adjusted $FWHM_{Mg}$ (cm^{-1})	Mean Adjusted Residual FWHM (cm^{-1})	SD Adjusted Residual FWHM (cm^{-1})
H. imperiale/laauense 417m (M3)	8.06	0.04	1.49	0.08
H. imperiale/laauense 417m (M3)	7.93	0.03	1.36	0.05
H. imperiale/laauense 417m (M3)	8.08	0.02	1.71	0.22
H. imperiale/laauense 417m (M3)	7.81	0.02	1.68	0.02
H. imperiale/laauense 417m (M3)	7.79	0.01	1.59	0.03
H. imperiale/laauense 417m (M3)	7.76	0.02	1.66	0.02
H. imperiale/laauense 417m (M3)	7.72	0.02	1.70	0.03
H. imperiale/laauense 417m (M3)	7.75	0.02	1.70	0.03
H. imperiale/laauense 417m (M3)	7.90	0.02	1.49	0.03
H. imperiale/laauense 417m (M3)	7.86	0.02	1.43	0.02
H. imperiale/laauense 560m	7.76	0.04	1.33	0.05
H. imperiale/laauense 560m	7.88	0.02	1.22	0.04
H. imperiale/laauense 560m	7.81	0.02	1.36	0.02
H. imperiale/laauense 560m	7.94	0.03	1.13	0.05
H. imperiale/laauense 560m	7.75	0.02	1.44	0.03
H. imperiale/laauense 560m	7.89	0.02	1.21	0.03
H. imperiale/laauense 560m	7.94	0.02	1.14	0.02
H. imperiale/laauense 574m	7.78	0.03	1.35	0.05
H. imperiale/laauense 574m	7.79	0.03	1.39	0.04
H. imperiale/laauense 574m	7.84	0.04	1.39	0.05
H. imperiale/laauense 574m	7.80	0.02	1.46	0.04
H. imperiale/laauense 574m	7.75	0.03	1.51	0.04
H. imperiale/laauense 574m	7.68	0.03	1.62	0.04
H. imperiale/laauense 574m	7.70	0.05	1.59	0.04
H. imperiale/laauense 574m	7.75	0.03	1.46	0.05
H. imperiale/laauense 574m	7.72	0.03	1.46	0.05
H. imperiale/laauense 574m	7.68	0.02	1.53	0.04
H. imperiale/laauense 574m	7.66	0.03	1.56	0.05
H. imperiale/laauense 582m	7.74	0.04	1.59	0.06
H. imperiale/laauense 582m	7.75	0.03	1.62	0.04
H. imperiale/laauense 582m	7.68	0.02	1.64	0.03
H. imperiale/laauense 582m	7.64	0.02	1.60	0.03
H. imperiale/laauense 582m	7.60	0.02	1.64	0.03
H. imperiale/laauense 582m	7.54	0.02	1.66	0.06
H. imperiale/laauense 582m	7.51	0.02	1.69	0.03
H. imperiale/laauense 582m	7.53	0.03	1.61	0.03
H. imperiale/laauense 582m	7.52	0.02	1.62	0.04
H. imperiale/laauense 582m	7.60	0.03	1.54	0.03
H. imperiale/laauense 582m	7.57	0.03	1.60	0.05
H. imperiale/laauense 582m	7.56	0.03	1.57	0.03
P. cf. secundum 221m	8.60	0.02	1.69	0.02
P. cf. secundum 221m	8.66	0.03	1.57	0.03
P. cf. secundum 221m	8.57	0.02	1.67	0.03
P. cf. secundum 221m	8.62	0.02	1.64	0.03
P. cf. secundum 221m	8.60	0.02	1.54	0.02
P. cf. secundum 221m	8.54	0.02	1.69	0.03
P. cf. secundum 221m	8.54	0.01	1.63	0.02
P. cf. secundum 221m	8.51	0.03	1.65	0.03
P. cf. secundum 221m	8.48	0.01	1.61	0.02
P. cf. secundum 221m	8.48	0.02	1.68	0.05
P. cf. secundum 238m (fast axis)	8.82	0.02	1.45	0.05
P. cf. secundum 238m (fast axis)	8.74	0.03	1.42	0.06
P. cf. secundum 238m (fast axis)	8.66	0.02	1.51	0.05
P. cf. secundum 238m (fast axis)	8.72	0.02	1.49	0.03
P. cf. secundum 238m (fast axis)	8.70	0.02	1.49	0.07

P. cf. secundum 238m (fast axis)	8.70	0.01	1.46	0.03
P. cf. secundum 238m (fast axis)	8.55	0.03	1.52	0.05
P. cf. secundum 238m (fast axis)	8.58	0.02	1.48	0.04
P. cf. secundum 238m (fast axis)	8.57	0.01	1.46	0.05
P. cf. secundum 238m (fast axis)	8.55	0.02	1.43	0.04
P. cf. secundum 238m (fast axis)	8.60	0.03	1.40	0.05
P. cf. secundum 238m (fast axis)	8.63	0.02	1.44	0.05
P. cf. secundum 238m (fast axis)	8.58	0.03	1.45	0.02
P. cf. secundum 238m (fast axis)	8.46	0.03	1.53	0.03
P. cf. secundum 238m (slow axis)	8.40	0.05	1.66	0.12
P. cf. secundum 238m (slow axis)	8.60	0.02	1.38	0.03
P. cf. secundum 238m (slow axis)	8.59	0.05	1.41	0.05
P. cf. secundum 238m (slow axis)	8.56	0.02	1.49	0.06
P. cf. secundum 238m (slow axis)	8.51	0.07	1.50	0.02
P. cf. secundum 238m (slow axis)	8.55	0.02	1.51	0.04
P. cf. secundum 238m (slow axis)	8.45	0.04	1.51	0.04
P. cf. secundum 238m (slow axis)	8.48	0.02	1.52	0.06
P. cf. secundum 238m (slow axis)	8.45	0.05	1.46	0.02
P. cf. secundum 238m (slow axis)	8.50	0.02	1.50	0.03
P. cf. secundum 238m (slow axis)	8.58	0.04	1.52	0.03
P. cf. secundum 238m (slow axis)	8.57	0.03	1.49	0.03
P. cf. secundum 238m (slow axis)	8.60	0.01	1.51	0.03
P. cf. secundum 238m (slow axis)	8.44	0.05	1.51	0.03
P. cf. secundum 238m (slow axis)	8.55	0.03	1.50	0.03
P. cf. secundum 238m (slow axis)	8.51	0.03	1.45	0.05
P. cf. secundum 238m (slow axis)	8.54	0.04	1.48	0.04
P. cf. secundum 238m (slow axis)	8.58	0.02	1.35	0.02
P. cf. secundum 238m (slow axis)	8.58	0.01	1.36	0.03
P. cf. secundum 238m (slow axis)	8.71	0.05	1.30	0.04
P. cf. secundum 238m (slow axis)	8.66	0.03	1.38	0.02
P. cf. secundum 238m (slow axis)	8.72	0.03	1.27	0.04
P. cf. secundum 238m (slow axis)	8.81	0.02	1.42	0.05
P. cf. secundum 238m (slow axis)	8.99	0.04	1.33	0.05
P. cf. secundum 238m (slow axis)	8.99	0.03	1.37	0.03
P. cf. secundum 238m (slow axis)	9.08	0.10	1.39	0.07

Table A5: Raman shift Mg, FWHM, and residual FWHM data from the depth gradient samples.

Species	Depth	Mean Raman Shift Mg* (cm^{-1})	SD Raman Shift Mg* (cm^{-1})	Mean FWHM (cm^{-1})	SD FWHM (cm^{-1})	Mean Residual FWHM* (cm^{-1})	SD Residual FWHM* (cm^{-1})
P. cf. *secundum*	221	11.44	0.06	10.06	0.03	1.64	0.04
P. cf. *secundum*	238	11.47	0.06	9.97	0.04	1.55	0.04
P. cf. *secundum*	269	10.99	0.05	9.84	0.03	1.57	0.04
P. cf. *secundum*	273	11.14	0.07	9.73	0.03	1.42	0.04
C. tortuosum	280	11.54	0.04	9.82	0.03	1.37	0.04
C. tortuosum	293	11.14	0.11	9.71	0.03	1.39	0.05
H. imp./laau.	395	10.48	0.10	9.43	0.04	1.34	0.06
Acanella spp.	396	10.13	0.06	9.49	0.03	1.52	0.04
H. imp./laau.	399	10.81	0.07	9.42	0.04	1.21	0.04
H. imp./laau.	401	9.86	0.07	9.38	0.02	1.51	0.04
H. imp./laau.	402	10.19	0.07	9.31	0.04	1.32	0.05
Acanella spp.	405	10.26	0.08	9.47	0.04	1.45	0.06
H. imp./laau.	444	9.22	0.24	9.21	0.04	1.57	0.07
H. imp./laau.	445	9.97	0.10	9.38	0.05	1.47	0.06
H. imp./laau.	446	9.89	0.06	9.32	0.03	1.44	0.04
H. imp./laau.	447	9.90	0.07	9.33	0.04	1.44	0.05
H. imp./laau.	449	9.22	0.09	9.26	0.05	1.62	0.05
H. imp./laau.	449	10.05	0.06	9.31	0.05	1.37	0.04
H. imp./laau.	449	10.16	0.08	9.32	0.03	1.34	0.03
Acanella spp.	451	9.10	0.10	9.33	0.06	1.73	0.08
H. imp./laau.	472	9.42	0.14	9.31	0.04	1.59	0.08
H. imp./laau.	506	9.18	0.12	9.25	0.05	1.62	0.08
H. imp./laau.	544	9.54	0.13	9.2	0.02	1.44	0.05
H. imp./laau.	560	9.22	0.05	9.24	0.04	1.59	0.04
H. imp./laau.	574	9.49	0.08	9.11	0.04	1.37	0.05
H. imp./laau.	582	8.97	0.09	9.13	0.03	1.58	0.04
Acanella spp.	753	9.73	0.14	9.45	0.13	1.62	0.09
Acanella spp.	823	9.47	0.05	9.14	0.03	1.41	0.04

*Note: All Raman-based Mg values (and subsequently, residual FWHM) have been corrected using LA-ICPMS Mg data. *Hemicorallium imperiale/laauense* is abbreviated as *H. imp./laau.*

Table A6: Raman shift Mg, FWHM, and residual FWHM data from the intra-sample Raman measurements.

Specimen	Branch Diameter (mm)	Mean Raman Shift Mg* (cm^{-1})	SD Raman Shift Mg* (cm^{-1})	Mean FWHM (cm^{-1})	SD FWHM (cm^{-1})	Mean Residual FWHM* (cm^{-1})	SD Residual FWHM* (cm^{-1})
H. imp./laau.444m	4.11	9.43	0.07	9.24	0.02	1.52	0.03
H. imp./laau.444m	1.09	9.25	0.26	9.40	0.03	1.75	0.07
H. imp./laau.444m	3.05	9.55	0.03	9.24	0.02	1.48	0.03
H. imp./laau.444m	2.53	9.51	0.02	9.26	0.05	1.51	0.05
H. imp./laau.444m	2.57	9.52	0.07	9.24	0.03	1.49	0.01
H. imp./laau.444m	2.07	9.45	0.04	9.32	0.02	1.59	0.03
H. imp./laau.444m	1.32	9.47	0.06	9.38	0.02	1.64	0.03
H. imp./laau.444m	3.03	9.46	0.04	9.26	0.02	1.53	0.02
H. imp./laau.444m	2.26	9.40	0.03	9.26	0.01	1.55	0.01
H. imp./laau.444m	1.11	9.45	0.03	9.38	0.03	1.66	0.03
H. imp./laau.444m	2.17	9.31	0.03	9.25	0.03	1.57	0.03
H. imp./laau.444m	1.26	9.58	0.01	9.42	0.01	1.65	0.02
H. imp./laau.444m	1.17	9.37	0.03	9.35	0.02	1.65	0.02
H. imp./laau.444m	0.96	9.31	0.04	9.39	0.03	1.71	0.02
H. imp./laau.444m	0.79	9.39	0.04	9.41	0.03	1.71	0.04
H. imp./laau.444m	0.93	9.68	0.04	9.46	0.05	1.65	0.04
H. imp./laau.444m	0.91	9.70	0.04	9.49	0.02	1.67	0.03
H. imp./laau.444m	0.58	10.23	0.07	9.74	0.04	1.74	0.04
H. imp./laau.444m	0.39	10.42	0.07	9.87	0.03	1.80	0.02
H. imp./laau.444m	3.67	9.67	0.05	9.22	0.01	1.41	0.01
H. imp./laau.472m	6.82	9.34	0.02	9.16	0.01	1.48	0.02
H. imp./laau.472m	3.44	9.12	0.03	9.18	0.01	1.58	0.02
H. imp./laau.472m	1.95	9.32	0.06	9.26	0.03	1.58	0.04
H. imp./laau.472m	1.43	9.53	0.02	9.39	0.02	1.64	0.02
H. imp./laau.472m	2.25	9.33	0.02	9.21	0.03	1.53	0.03
H. imp./laau.472m	1.76	9.41	0.02	9.24	0.01	1.53	0.02
H. imp./laau.472m	5.53	9.20	0.01	9.15	0.02	1.51	0.02
H. imp./laau.472m	1.49	9.42	0.03	9.34	0.01	1.62	0.01
H. imp./laau.472m	1.61	9.14	0.05	9.33	0.02	1.71	0.03
H. imp./laau.472m	4.37	9.16	0.04	9.17	0.01	1.55	0.02
H. imp./laau.472m	2.26	9.53	0.04	9.31	0.02	1.56	0.03
H. imp./laau.472m	1.83	9.36	0.01	9.19	0.03	1.50	0.03
H. imp./laau.472m	2.47	9.22	0.04	9.20	0.01	1.55	0.01
H. imp./laau.472m	2.11	9.19	0.03	9.23	0.02	1.60	0.02
H. imp./laau.472m	1.11	9.63	0.03	9.40	0.04	1.61	0.04
H. imp./laau.472m	3.09	9.19	0.03	9.16	0.03	1.53	0.03
H. imp./laau.472m	3.98	9.02	0.07	9.14	0.02	1.57	0.04
H. imp./laau.472m	5.02	9.38	0.05	9.11	0.02	1.41	0.02
H. imp./laau.472m	5.91	9.08	0.02	9.14	0.01	1.55	0.01
H. imp./laau.472m	0.73	9.56	0.02	9.47	0.04	1.70	0.04
P. cf. *secundum* 273m	13.04	11.62	0.05	9.75	0.06	1.28	0.07
P. cf. *secundum* 273m	8.33	11.49	0.08	9.66	0.04	1.23	0.06
P. cf. *secundum* 273m	2.69	11.29	0.10	9.82	0.04	1.46	0.04
P. cf. *secundum* 273m	4.28	11.50	0.06	9.71	0.06	1.28	0.08
P. cf. *secundum* 273m	8.22	11.37	0.05	9.73	0.03	1.34	0.02
P. cf. *secundum* 273m	5.18	11.35	0.05	9.70	0.05	1.32	0.06

P. cf. *secundum* 273m	6.01	11.48	0.07	9.75	0.03	1.32	0.05
P. cf. *secundum* 273m	4.42	11.46	0.05	9.73	0.02	1.31	0.03
P. cf. *secundum* 273m	5.64	11.55	0.04	9.72	0.02	1.27	0.03
P. cf. *secundum* 273m	1.86	11.15	0.10	9.71	0.03	1.39	0.02
P. cf. *secundum* 273m	6.48	11.43	0.06	9.73	0.03	1.32	0.03
P. cf. *secundum* 273m	4.94	11.42	0.04	9.70	0.03	1.29	0.03
P. cf. *secundum* 273m	3.26	11.54	0.04	9.74	0.03	1.29	0.04
P. cf. *secundum* 273m	3.29	11.37	0.04	9.71	0.02	1.32	0.01
P. cf. *secundum* 273m	2.49	11.47	0.06	9.72	0.02	1.30	0.04
P. cf. *secundum* 273m	8.46	11.22	0.04	9.75	0.04	1.41	0.04
P. cf. *secundum* 273m	10.13	11.33	0.04	9.80	0.05	1.43	0.06
P. cf. *secundum* 273m	1.22	11.50	0.06	9.81	0.05	1.38	0.07
P. cf. *secundum* 273m	1.77	11.87	0.08	9.97	0.07	1.42	0.06
P. cf. *secundum* 273m	0.95	11.63	0.04	9.95	0.04	1.48	0.04
C. tortuosum 280m	7.11	11.44	0.04	9.77	0.03	1.35	0.02
C. tortuosum 280m	6.31	11.44	0.05	9.80	0.03	1.39	0.03
C. tortuosum 280m	4.87	11.39	0.11	9.76	0.04	1.36	0.06
C. tortuosum 280m	3.91	11.46	0.06	9.82	0.02	1.39	0.02
C. tortuosum 280m	3.74	11.35	0.06	9.84	0.02	1.46	0.04
C. tortuosum 280m	2.4	11.77	0.11	10.00	0.03	1.48	0.05
C. tortuosum 280m	7.08	11.20	0.06	9.70	0.03	1.37	0.04
C. tortuosum 280m	4.74	11.52	0.02	9.83	0.02	1.39	0.02
C. tortuosum 280m	1.67	11.72	0.12	10.16	0.03	1.66	0.05
C. tortuosum 280m	3.25	11.46	0.07	9.83	0.02	1.41	0.01
C. tortuosum 280m	7.31	11.37	0.09	9.76	0.03	1.36	0.02
C. tortuosum 280m	1.45	11.75	0.13	10.10	0.07	1.59	0.05
C. tortuosum 280m	1.05	11.50	0.08	9.91	0.04	1.47	0.05
C. tortuosum 280m	3.6	11.48	0.13	9.84	0.03	1.41	0.05
C. tortuosum 280m	1.14	11.57	0.09	9.95	0.06	1.49	0.08
C. tortuosum 280m	1.44	11.71	0.22	10.08	0.01	1.58	0.06
C. tortuosum 280m	3.65	11.72	0.03	9.82	0.05	1.32	0.05
C. tortuosum 280m	0.89	11.58	0.15	10.01	0.05	1.55	0.04
C. tortuosum 280m	2.45	11.57	0.06	9.88	0.03	1.42	0.04
C. tortuosum 280m	3.13	11.54	0.04	9.89	0.06	1.44	0.06
Acanella spp. 823m	8.58	9.30	0.06	9.13	0.02	1.46	0.04
Acanella spp. 823m	8.61	9.25	0.07	9.18	0.03	1.53	0.04
Acanella spp. 823m	8.15	9.15	0.04	9.12	0.01	1.50	0.03
Acanella spp. 823m	7.85	9.11	0.07	9.14	0.04	1.54	0.05
Acanella spp. 823m	7.68	9.50	0.06	9.22	0.02	1.47	0.04
Acanella spp. 823m	6.76	9.31	0.06	9.23	0.03	1.55	0.04
Acanella spp. 823m	6.54	9.26	0.04	9.16	0.02	1.50	0.04
Acanella spp. 823m	3.78	9.28	0.08	9.01	0.04	1.34	0.04
Acanella spp. 823m	5.64	9.16	0.05	9.10	0.04	1.48	0.04
Acanella spp. 823m	4.3	9.17	0.06	9.05	0.02	1.43	0.04
Acanella spp. 823m	2.96	9.44	0.05	9.01	0.03	1.29	0.03
Acanella spp. 823m	2.75	9.43	0.06	8.96	0.02	1.24	0.02
Acanella spp. 823m	2.53	9.32	0.09	9.01	0.02	1.33	0.05
Acanella spp. 823m	1.93	9.43	0.06	8.98	0.03	1.26	0.04

Acanella spp. 823m	1.87	9.41	0.04	8.94	0.03	1.23	0.04
Acanella spp. 823m	1.85	9.40	0.04	8.99	0.02	1.28	0.03
Acanella spp. 823m	1.26	9.53	0.04	9.00	0.02	1.25	0.03
Acanella spp. 823m	1.17	9.54	0.06	9.04	0.05	1.28	0.06
Acanella spp. 823m	0.96	9.60	0.07	9.07	0.04	1.29	0.06
Acanella spp. 823m	1.05	9.88	0.09	9.03	0.05	1.15	0.04

Note: *Hemicorallium imperiale/laauense* is abbreviated as *H. imp./laau.*

BIBLIOGRAPHY

Acosta-Maeda, T.E., Scott, E.R.D., Sharma, S.K., and Misra, A.K. (2013) The pressures and temperatures of meteorite impact: Evidence from micro-Raman mapping of mineral phases in the strongly shocked Taiban ordinary chondrite. American Mineralogist, 98, 859-869.

Al-Horani, F.A., Al-Moghrabi, S.M., and de Beer, D. (2003) The mechanism of calcification and its relation to photosynthesis and respiration in the scleractinian coral Galaxea fascicularis. Marine Biology, 142, 419-426.

Andersson, A.J., Mackenzie, F.T., and Bates, N.R. (2008) Life on the margin: implications of ocean acidification on Mg-calcite, high latitude and cold-water marine calcifiers. Marine Ecology Progress Series, 373, 265-273.

Ardila, N.E., Giribet, G., and Sánchez, J.A. (2012) A time-calibrated molecular phylogeny of the precious corals: reconciling discrepancies in the taxonomic classification and insights into their evolutionary history. BMC Evolutionary Biology 12:246.

Bischoff, W.D., Sharma, S.K., and MacKenzie, F.T. (1985) Carbonate ion disorder in synthetic and biogenic magnesian calcites: a Raman spectral study. American Mineralogist, 70, 581-589.

Bostock, H.C., Tracey, D.M., Currie, K.I., Dunbar, G.B., Handler, M.R., Mikaloff Fletcher, S.E., Smith, A.M., and Williams, M.J.M. (2015) The carbonate mineralogy and distribution of habitat forming deep-sea corals in the southwest Pacific region. Deep Sea Research Part I: Oceanographic Research Papers, 100, 88-104.

Calil, P.H.R., Richards, K.J., Jia, Y., and Bidigare, R.R. (2008) Eddy activity in the lee of the Hawaiian Islands. Deep Sea Research Part II: Topical Studies in Oceanography, 55, 1179-1194.

Chaabane, S., López Correa, M., Ziveri, P., Trotter, J., Kallel, N., Douville, E., McCulloch, M., Taviani, M., Linares, C., and Montagna, P. (2019) Elemental systematics of the calcitic skeleton of Corallium rubrum and implications for the Mg/Ca temperature proxy. Chemical Geology, 52, 237-258.

Chave, K.E. (1954) Aspects of biogeochemistry of magnesium 1. Calcareous marine organisms. Journal of Geology, 62, 266–283.

Comeau, S., Cornwall, C.E., DeCarlo, T.M., Krieger, E., and McCulloch, M.T. (2018) Similar controls on calcification under ocean acidification across unrelated coral reef taxa. Global Change Biology, 24, 4857-4868.

Cornwall, C., Comeau, S., DeCarlo, T., Moore, B., D'alexis, Q., and McCulloch, M. (2018) Resistance of corals and coralline algae to ocean acidification: physiological control of calcification under natural pH variability. Proceedings of the Royal Society B: Biological Sciences, 285, 20181168.

Cornwall, C., Comeau, S., DeCarlo, T.M., Larcombe, E., Moore, B., Giltrow, K., Puerzer, F., D'Alexis, Q., and McCulloch, M.T. (2020) A coralline alga gains tolerance to ocean acidification over multiple generations of exposure. Nature Climate Change, 10, 143-146.

DeCarlo, T., D'Olivo, J., Foster, T., Holcomb, M., Becker, T., and McCulloch, M. (2017) Coral calcifying fluid aragonite saturation states derived from Raman spectroscopy. Biogeosciences, 14, 5253-5269.

DeCarlo, T.M., Ren, H., and Farfan, G.A. (2018) The origin and role of organic matrix in coral calcification: Insights from comparing coral skeleton and abiogenic aragonite. Frontiers in Marine Science, 5, 170.

DeCarlo, T.M., Comeau, S., Cornwall, C.E., Gajdzik, L., Guagliardo, P., Sadekov, A., Thillainath E.C., Trotter, J., and McCulloch, M.T. (2019) Investigating marine bio calcification mechanisms in a changing ocean with in vivo and high-resolution ex vivo Raman spectroscopy. Global Change Biology, 25, 1877-1888.

Dickson, A.G. (1990) Thermodynamics of the dissociation of boric acid in synthetic seawater from 273.15 to 318.15 K. Deep Sea Research, 37, 755-766.

Dickson, A.G., and Millero, F.J. (1987) A comparison of the equilibrium constants for the dissociation of carbonic acid in seawater media. Deep Sea Research, 34, 1733-1743.

Dickson, A.G., Sabine, C.L., and Christian, J.R. (2007) Guide to best practices for ocean CO_2 measurements, 191 p. PICES, Sidney.

Dueñas, L.F., Alderslade, P., and Sánchez, J.A. (2014) Molecular systematics of the deep-sea bamboo corals (Octocorallia: Isididae: Keratoisidinae) from New Zealand with descriptions of two new species of Keratoisis. Molecular Phylogenetics and Evolution, 74, 15-28.

Farfan, G.A., Apprill, A., Cohen, A., DeCarlo, T.M., Post, J.E., Waller, R.G., Hansel, C.M. (2021) Crystallographic and chemical signatures in coral skeletal aragonite. Coral Reefs, 41, 19-34.

Farmer, J.R., Hönisch, B., Robinson, L.F., and Hill, T.M. (2015) Effects of seawater-pH and biomineralization on the boron isotopic composition of deep-sea bamboo corals. Geochimica et Cosmochimica Acta, 155, 86-106.

Flöter, S., Fietzke, J., Gutjahr, M., Farmer, J., Hönisch, B., Nehrke, G., and Eisenhauer, A. (2019) The influence of skeletal micro-structures on potential proxy records in a bamboo coral. Geochimica et Cosmochimica Acta, 248, 43-60.

Gagnon, A.C., Adkins, J.F., Fernandez, D.P., and Robinson, L.F. (2007) Sr/Ca and Mg/Ca vital effects correlated with skeletal architecture in a scleractinian deep-sea coral and the role of Rayleigh fractionation. Earth and Planetary Science Letters, 261, 280-295.

Greenwood, J. (2009) Shallow water dissolution of settling calcite at station ALOHA. Limnology and Oceanography, 54, 1420-1424.

Hasegawa, H., Rahman, M.A., Luan, N.T., Maki, T., and Iwasaki, N. (2012). Trace elements in Corallium spp. as indicators for origin and habitat. Journal of Experimental Marine Biology and Ecology, 414, 1–5.

Kaabar, W., Bott, S., and Devonshire, R. (2011) Raman spectroscopic study of mixed carbonate materials. Spectrochimica Acta A, 78, 136-141.

Kontoyannis, C.G., Orkoula, M.G., and Koutsoukos, P.G. (1997) Quantitative analysis of sulfated calcium carbonates using Raman spectroscopy and X-ray Powder Diffraction. Analyst, 122, 33-38.

Krishnamurti, D. (1957) The Raman spectrum of calcite and its interpretation. Proceedings of the Indian Academy of Sciences, A46, 183-202.

LaVigne, M., Hill, T.M., Spero, H.J., and Guilderson, T.P. (2011) Bamboo coral Ba/Ca: calibration of a new deep ocean refractory nutrient proxy. Earth Planetary Science Letters, 312, 506-515.

Lebrato, M., Andersson, A.J., Ries, J.B., Aronson, R.B., Lamare, M.D., Koeve, W., Oschlies, A., Iglesias-Rodriguez, M.D., Thatje, S., Amsler, M., Vos, S.C., Jones, D.O.B., Ruhl, H.A., Gates, A.R., and McClintock, J.B. (2016) Benthic marine calcifiers coexist with $CaCO_3$-undersaturated seawater worldwide. Global Biogeochemical Cycles, 30, 1038-1053.

Lendvay, B., Cartier, L.E., Gysi, M., Meyer, J.B., Krzemnicki, M.S., Kratzer, A., and Morf, N.V. (2020) DNA fingerprinting: an effective tool for taxonomic identification of precious corals in jewelry. Science Reports, 10, 1-12.

Lewis, E., and Wallace, D. (1998) Program developed for CO_2 system calculations: Carbon Dioxide Information Analysis Center, Oak Ridge National Laboratory, ORNL/CDIAC 105.

Long, X., Ma, Y., and Qi, L. (2014) Biogenic and synthetic high magnesium calcite–A review. Journal of Structural Biology, 185, 1-14.

Luan, N.T., Rahman, M.A., Maki, T., Iwasaki, N., and Hasegawa, H. (2013) Growth characteristics and growth rate estimation of Japanese precious corals. Journal of Experimental Marine Biology and Ecology, 441, 117-125.

Mackenzie, F.T., Bischoff, W.D., Bishop, F.C., Loijens, M., Schoonmaker, J., and Wollast, R. (1983) Magnesian calcites: low temperature occurrence, solubility and solid-solution behavior. In R.J. Reeder, Ed., Carbonates: Mineralogy and Chemistry, 11, p. 97-143. Reviews in Mineralogy, Mineralogical Society of America, Washington, DC.

Mass, T., Drake, J.L., Haramaty, L., Kim, J.D., Zelzion, E., Bhattacharya, D., and Falkowski, P.G. (2013) Cloning and characterization of four novel coral acid-rich proteins that precipitate carbonates in vitro. Current Biology, 23, 1126-1131.

Mavromatis, V., Gautier, Q., Bosc, O., and Schott, J. (2013) Kinetics of Mg partition and Mg stable isotope fractionation during its incorporation in calcite. Geochimica et Cosmochimica Acta, 114, 188-203.

McCulloch, M., Falter, J., Trotter, J., and Montagna, P. (2012) Coral resilience to ocean acidification and global warming through pH up-regulation. Nature Climate Change, 2, 623-627.

McDougall, T.J., and Barker, P.M. (2011) Getting started with TEOS-10 and the Gibbs Seawater (GSW) Oceanographic Toolbox, 28pp., SCOr/IAPSO WG127.

Mehrbach, C., Culberson, C.H., Hawley, J.E., and Pytkowicx, R.M. (1973) Measurement of the apparent dissociation constants of carbonic acid in seawater at atmospheric pressure. Limnology and Oceanography, 18, 897-907.

Merrifield, M.A., and Holloway, P.E. (2002) Model estimates of M2 internal tide energetics at the Hawaiian Ridge. Journal of Geophysical Research, 107, 3179.

Morse, J.W., Andersson, A.J., and Mackenzie, F.T. (2006) Initial responses of carbonate-rich shelf sediments to rising atmospheric pCO_2 and “ocean acidification:” role of high Mg calcites. Geochimica et Cosmochimica Acta, 70, 5814–5830.

Morse, J.W., Arvidson, R.S., and Lüttge, A. (2007) Calcium carbonate formation and dissolution. Chemical Reviews, 107, 342-381.

Mucci, A. (1987) Influence of temperature on the composition of magnesian calcite overgrowths precipitated from seawater. Geochimica et Cosmochimica Acta, 51, 1977-1984.

Murakami-Sugihara, N., Shirai, K., Hori, M., Amano, Y., Fukuda, H., Obata, H., Tanaka, K., Mizukawa, K., Sano, Y., Takada, H., and Ogawa, H. (2019) Mussel shell geochemical analyses reflect coastal environmental changes following the 2011 Tohoku tsunami. ACS Earth and Space Chemistry, 3, 1346-1352.

Perrin, J., Vielzeuf, D., Ricolleau, A., Dallaporta, H., Valton, S., and Floquet, N. (2015) Block by-block and layer-by-layer growth modes in coral skeletons. American Mineralogist, 100, 681-695.

Perrin, J., Vielzeuf, D., Laporte, D., Ricolleau, A., Rossman, G.R., and Floquet, N. (2016) Raman characterization of synthetic magnesian calcites. American Mineralogist, 101, 2525-2538.

R Core Team (2021) R: A language and environment for statistical computing. Vienna, Austria: R Foundation for Statistical Computing.

Riebesell, U., Fabry, V.J., Hansson, L., and Gattuso, J.P. (2010). Guide to best practices for ocean acidification research and data reporting, 260 p., Publications Office of the European Union, Luxembourg.

Robinson, L.F., Adkins, J.F., Frank, N., Gagnon, A.C., Prouty, N.G., Roark, E.B., and van de Flierdt, T. (2014) The geochemistry of deep-sea coral skeletons: a review of vital effects and applications for paleoceanography. Deep Sea Research Part II: Topical Studies in Oceanography, 99, 184-198.

Sherwood, O.A., Heikoop, J.M., Sinclair, D.J., Scott, D.B., Risk, M.J., Shearer, C., and Azetsu Scott, K. (2005) Skeletal Mg/Ca in Primnoa resedaeformis: relationship to temperature. In A. Freiwald and J.M. Roberts, Eds., Cold-water Corals and Ecosystems, p. 1061-1079, Springer-Verlag, Berlin.

Shibano, Y., Takahata, K., Kawano, J., Watanabe, T., Enomoto, D., Kagi, H., Kamiya, N., and Yamamoto, J. (2017) Raman spectroscopic determination of Sr/Ca ratios of calcite samples. Journal of Raman Spectroscopy, 48, 1755-1761.

Sinclair, D.J., Williams, B., Allard, G., Ghaleb, B., Fallon, S., Ross, S.W., and Risk, M. (2011) Reproducibility of trace element profiles in a specimen of the deep-water bamboo coral Keratoisis sp. Geochimica et Cosmochimica Acta, 75, 5101-5121.

Tambutté, S., Holcomb, M., Ferrier-Pagés, C., Reynaud, S., Tambutté, E., Zoccola, D., and Allemand, D. (2011) Coral biomineralization: from gene to the environment. Journal of Experimental Marine Biology and Ecology, 408, 58-78.

Thresher, R., Rintoul, S.R., Koslow, J.A., Weidman, C., Adkins, J., and Proctor, C. (2004) Oceanic evidence of climate change in southern Australia over the last three centuries. Geophysical Research Letters, 31, L07212.

Thresher, R.E., MacRae, C.M., Wilson, N.C., and Gurney, R. (2007) Environmental effects on the skeletal composition of deep-water gorgonians (Keratoisis spp.; Isididae). Bulletin of Marine Science, 81, 409-422.

Thresher, R.E., Wilson, N.C., MacRae, C.M., and Neil, H. (2010) Temperature effects on the calcite skeletal composition of deep-water gorgonians (Isididae). Geochimica et Cosmochimica Acta, 74, 4655-4670.

Thresher, R.E., Tilbrook, B., Fallon, S., Wilson, N.C., and Adkins, J. (2011) Effects of chronic low carbonate saturation levels on the distribution, growth and skeletal chemistry of deep-sea corals and other seamount megabenthos. Marine Ecology Progress Series, 442, 87-99.

Thresher, R.E., Fallon, S.J., and Townsend, A.T. (2016) A "core-top" screen for trace element proxies of environmental conditions and growth rates in the calcite skeletons of bamboo corals (Isididae). Geochimica et Cosmochimica Acta, 193, 75-99.

Uppström, L.R. (1974) The boron/chlorinity ratio of deep-sea water from the Pacific Ocean. Deep Sea Research and Oceanographic Abstracts, 21, 161-162.

Urmos, J., Sharma, S.K., and Mackenzie, F.T. (1991) Characterization of some biogenic carbonates with Raman spectroscopy. American Mineralogist, 76, 641-646.

Vielzeuf, D., Garrabou, J., Baronnet, A., Grauby, O., and Marschal, C. (2008) Nano to macroscale biomineral architecture of red coral (Corallium rubrum). American Mineralogist, 93, 1799-1815.

Vielzeuf, D., Garrabou, J., Gagnon, A., Ricolleau, A., Adkins, J., Günther, D., Hametner, K., Devidal, J-L., Reusser, E., and Perrin, J. (2013) Distribution of sulphur and magnesium in the red coral. Chemical Geology, 355, 13-27.

Vielzeuf, D., Gagnon, A.C., Ricolleau, A., Devidal, J-L., Balme-Heuze, C., Yahiaoui, N., Fonquernie, C., Perrin, J., Garrabou, J., and Montel, J-M. (2018) Growth kinetics and distribution of trace elements in precious corals. Frontiers in Earth Science, 6, 167.

Watson, E.B. (2004) A conceptual model for near-surface kinetic controls on the trace-element and stable isotope composition of abiogenic calcite crystals. Geochimica et Cosmochimica Acta, 68, 1473-1488.

Weinbauer, M., Brandstätter, F., and Velimirov, B. (2000) On the potential use of magnesium and strontium concentrations as ecological indicators in the calcite skeleton of the red coral (Corallium rubrum). Marine Biology, 137, 801-809.

White, W. (1974) The carbonate minerals. In E.V.C. Farmer, Ed., The Infrared Spectra of Minerals, Mineralogical Society Monograph, 4, p. 87-110, Mineralogical Society, London.

Yoshimura, T., Tanimizu, M., Inoue, M., Suzuki, A., Iwasaki, N., and Kawahata, H. (2011) Mg isotope fractionation in biogenic carbonates of deep-sea coral, benthic foraminifera, and hermatypic coral. Analytical and Bioanalytical Chemistry, 401, 2755-2769.